Stopping of heavy ions in plasmas at strong coupling

Günter Zwicknagel[a,*], Christian Toepffer[b], Paul-Gerhard Reinhard[b]

[a] *Laboratoire de Physique des Gaz et des Plasmas, Bâtiment 212, Université Paris XI, F-91405 Orsay, France*
[b] *Institut für Theoretische Physik, Universität Erlangen, D-91058 Erlangen, Germany*

Contents

Abstract

Standard approaches to the energy loss of ions in plasmas like the dielectric linear response or the binary collision model are strictly valid only in the regimes where the plasma is close to ideal and the coupling between projectile-ion and the plasma target is sufficiently weak. In this review we explore the stopping power in regimes where these conditions are

---

* Corresponding author. Present address: Institut für Theoretische Physik, Universität Erlangen, D-91058 Erlangen, Germany. E-mail: zwicknagel@theorie2.physik.uni-erlangen.de.

STOPPING OF HEAVY IONS IN PLASMAS AT STRONG COUPLING

Günter ZWICKNAGEL[a]**, Christian TOEPFFER**[b]**, Paul-Gerhard REINHARD**[b]

[a] *Laboratoire de Physique des Gaz et des Plasmas, Bâtiment 212, Université Paris XI, F-91405 Orsay, France*
[b] *Institut für Theoretische Physik, Universität Erlangen, D-91058 Erlangen, Germany*

not met. Actually relevant fields of application are heavy ion driven inertial fusion and the cooling of beams of charged particles by electrons. The conventional linear mean-field treatments are extended by many-body methods and particle simulations to account for strong correlations between the particles and for nonlinear coupling. We report the following important results in connection with the stopping at strong coupling: The energy loss of an ion scales with its charge approximately like $Z^{1.5}$, the effective screening length depends on Z and is larger than the Debye length. Slow highly charged ions are surrounded by a cloud of electrons trapped by many body collisions. Quantum effects like the wave nature of the electrons and Pauli-blocking reduce the stopping power by mollifying the effective interactions. © 1999 Elsevier Science B.V. All rights reserved.

1. Introduction

The energy loss of fast, heavy particles passing through matter was first considered by Bohr [21] who treated the target electrons as classical particles. As the transfer of energy to the free electrons of the plasma target does not occur in quantized steps the classical approach is valid as long as the plasma is not degenerate. The quantized energy transfer to bound electrons, first considered by Bethe [19] and Bloch [20] leads to a reduction of the stopping power. Also the effective charge state of the ion is higher in a plasma as compared to a cold gas. The energy loss in a plasma is thus much larger than in a cold gas [127]. These theoretical predictions have been confirmed by recent experiments [33,34,42,43,59,94,95,163].

There are two standard approaches to the energy loss of ions in an electron plasma. On one hand one considers the stopping due to the polarization cloud which the moving ion creates in its wake. This is essentially a continuum treatment which ceases to be valid on scales comparable to the inter-particle distance. Alternatively one considers the energy transfer in successive binary collisions between the projectile and the electrons. Here it is essential to include the shielding of the Coulomb potential by the polarization of the plasma on long ranges. Thus both approaches are complementary to each other: The continuum treatment for the polarization requires a cutoff at small distances because the plasma consists of discrete particles and the model involving collisions between particles has an upper cutoff due to shielding. In fact both theories yield nearly identical results for the stopping power as long as the conditions remain standard in the sense that the target plasma is ideal, i.e. hard collisions between the electrons are rare, and that the coupling between the ion and the target is linear.

It is the purpose of this report to investigate the energy loss of ions in a plasma beyond these standard conditions, i.e. for strong ion–electron coupling and/or non-ideal targets. Such studies are of considerable actual interest in at least two areas of application:

1. In heavy ion inertial fusion (HIF) one plans to compress a $d - t$ pellet until ignition. The compression is either driven directly by ions or indirectly by X-rays produced through the stopping of ions in a converter. In either case, targets with densities 10^{21}–10^{24} cm^{-3} are heated through the energy loss of the ions. The resulting target plasmas eventually reach temperatures of 100 eV, but are nonideal in the initial stages of the heating process. The current status of HIF has been reported in Ref. [143].
2. In most experiments with charged particle beams it is desired that the particles are concentrated in a small fraction of the single-particle (μ)-phase space. One method to reduce the phase space volume of an ion beam is electron cooling as proposed by Budker [28]. The ion beam is mixed with a co-moving electron beam which has a very small longitudinal momentum spread corresponding to a temperature of a few K due to its acceleration from the source. In the rest frame of the beams the cooling process may then be envisaged as a stopping of ions in an electron plasma. Although the density is low, $n = 10^7$–10^8 cm^{-3}, the electrons are strongly correlated because of the low longitudinal temperature. Moreover the ions in the beam are often highly charged, for example U^{92+} in experiments planned to investigate transitions from ordinary hadronic matter to a quark-gluon plasma with the help of the Large Hadron Collider (LHC) at CERN. In such situations the coupling between the ions and the cooler electrons becomes highly nonlinear. Reviews on electron cooling have been given in Refs. [166,142] and

the proceedings [144,145] present the current status of the physics of cold and highly correlated beams.

The report is organized as follows: In Section 2.1 we present the hamiltonian for the ion–target system. The stopping power dE/ds is defined in Section 2.2. There follows in Section 2.3 an identification of various regimes for the ion–plasma system. While the target parameters density n and temperature T define the ideality ξ and the degeneracy Θ, the projectile properties charge Z and velocity v determine the strength of the ion–target coupling. In Section 3.1 we discuss methods appropriate for linear coupling with ideal and nonideal targets. In order of increasing perturbation caused by the ion there follows a regime in which the electrons are subjected to weak coupling except for a very small fraction of space where the coupling to the ion is strong. We have coined the name semilinear coupling for this regime which is discussed in Section 3.2. Finally, we present in Section 3.3 methods for the truly nonlinear coupling regime where analytical treatments are no longer possible. Again one follows the lines of either improving the continuum treatment by accounting for higher correlations in the response of the target to the ion or to account for such correlations when calculating effective cross sections for particle collisions in the medium. This involves unavoidably increasing numerical expense. One may then find it advantageous to use numerical methods like molecular dynamics (MD) computer simulations. In Section 3.4 we give a summary of possible approaches to the energy loss in plasmas according to the different regimes of application. In Section 4.1 we present some salient features of stopping in classical plasmas, mainly for purposes of later comparison. Actual results for the nonlinear stopping obtained by classical simulations are presented and compared with other treatments and experiments in Section 4.2.

Nonlinear screening and the trapping of electrons by slowly moving highly charged ions is discussed in Section 4.3. Quantum effects, both the wave nature of the electrons as well as Pauli-blocking within the target tend to mollify the effective interaction between charged particle and thus reduce the stopping power. This is investigated in Section 5.1 with the help of effective potentials and confirmed by semiclassical wave packet molecular dynamics (WPMD) computer simulations in Section 5.2. As the WPMD gives some account for quantum correlations it is compared in Section 5.3 with another approach to strong quantum correlations starting from the hypernetted chain (HNC) method with effective interactions. Our results are summed up in Section 6. Finally there are appendices dealing with more technical matters like various simulation techniques, as molecular dynamics (MD) which accounts for particle collisions vs. the particle-in-cell (PIC) method which is a mean field approach. We further provide lists of definitions of important quantities and a list of symbols.

2. The projectile–target system

2.1. General considerations and definitions

For a complete theoretical description of the energy loss of charged particles passing through matter one is confronted with a large spectrum of physical processes. First challenges arise from describing the target, which, depending on density and temperature, may be a solid, fluid, gas or

plasma. Therefore one has to know the degree of ionization, the degeneracy of the electrons and the various types of ions in the target and the related bound states. This involves already a rather complete solution of many-body and atomic physics. In particular the composition of dense plasmas and their properties as conductivity or opacity are topics of actual theoretical and experimental investigations. Once the target is specified one is left with the additional aspects of the projectile–target interaction. Here the two main topics are:

1. The energy loss of the projectile in elastic collisions with free target electrons and target ions and in inelastic collisions due to ionization of target ions and excitation of bound electrons.
2. The changes in the electronic configuration of the projectile ion by various processes as radiative, dielectronic and three- or many-body recombination of free electrons, collisional ionization and excitation by target ions and electrons as well as charge transfer by bound–bound transitions between target ions and projectile. Most of these processes give also small contributions to the energy loss.

Because the time scales are usually quite different, the stopping itself can be separated from the dynamics of the projectile ionization. This results in a much more simplified description of stopping compared to a full scheme where all processes mentioned are considered simultaneously. While the stopping power is now determined for a given electronic configuration of the projectile, the changes of the configuration during the entire process of slowing down are calculated from rate equations which account for all the various atomic processes as discussed e.g. in Refs. [34,116,117,136]. The stopping power for fixed projectile ionization together with the evolution of the charge state finally yields the energy loss over the time or path of interest. If necessary the corresponding amount of energy loss related to the processes which change the electronic configuration of the projectile must be added.

There remains the task to calculate the stopping power for a given charge state. This still includes stopping contributions by free electrons, by target nuclei and ionization or excitation of target ions. Nuclear stopping yields relevant contributions only for very small projectile velocities of the order of the thermal velocity of the nuclei in the target. Thus one can neglect if for the largest part of the slowing down process. Then one concentrates on the energy loss to free and bound electrons. The calculation of stopping by bound electrons, see e.g. Refs. [24,26,36,58,79,117,179], requires in general an accurate knowledge of energy levels and related transition probabilities (oscillator strengths) in the target ions. At least a mean ionization potential of the target has to be provided for determining the stopping power at high velocities using the Bethe stopping formula [19]. The existence of bound electrons in the target strongly affects the charge state of the projectile, mainly by the very efficient bound–bound charge transfer. The stopping power, however, is usually dominated by the free electron contribution, provided that the degree of ionization of the target is high enough to supply some amount of free electrons. Stopping by free electrons is very efficient because any amount of energy can be transferred in contrast to the quantized energy transfer for the excitation of bound states. Hence the stopping power in a plasma is higher than in a cold gas. Because decreasing numbers of bound electrons are accompanied by less charge transfer to the target, the charge states of the projectile are usually higher in plasmas compared to a gas. Together with the more efficient free electron stopping this results in an enhanced stopping in plasmas as theoretically predicted [127] and experimentally observed [33,34,42,43,59,94,95,163].

Here we intend to concentrate on the many-body aspects involved in the stopping at strong coupling rather than the atomic physics of the target ions. Hence we focus only on the free electron contribution to stopping. For discussing the energy loss at strong coupling we thus consider mainly a point-like projectile of given charge in a free electron target plasma. This restriction to free electrons becomes of course more and more realistic for increasing degrees of ionization, that is at high temperatures. Also in dense plasmas bound states disappear through a lowering of the continuum edge. For investigations concerning electron cooling even the real target is a free electron target.

Within this simplified model the hamiltonian of the free electron (charge e, mass m) target can be written as

$$\hat{H}_0 = \sum_i \frac{\hat{p}_i^2}{2m} + \sum_i \sum_{j \neq i} \frac{e^2}{4\pi\varepsilon_0 |\hat{r}_i - \hat{r}_j|} + U_0 \, , \tag{1}$$

where U_0 is a constant representing the potential energy related to the interaction of the electrons with a static homogeneous charge neutralizing background as well as to the background–background interaction. Here we restrict ourselves to non-relativistic situations concerning the target conditions – as already assumed in Eq. (1) – as well as the projectile velocities. A review of the stopping of relativistic projectiles can be found in [2]. For treating the energy loss of the charged projectile we assume that the projectile–target interaction is switched on instantaneously at a certain time. This leads to the Hamilton operator for the projectile–target system:

$$\hat{H}(t) = \hat{H}_0 + \frac{\hat{P}^2}{2M} - \theta(t - t_0)\sum_i e\phi_{\mathrm{p}}(\hat{r}_i - \hat{R}) \, , \tag{2}$$

with the position R, momentum P, mass M and potential $\phi_{\mathrm{p}}(r) = Ze/4\pi\varepsilon_0|r|$ of the projectile and the step function $\theta(t)$. On this level of description of the projectile–target system, bound states of the projectile are still included as well as all changes of its electronic configuration as far as free electrons are involved, e.g. in the case of ionization by electron–projectile collisions and recombinations due to three- or many-body interactions.

2.2. Definitions of the stopping power

The key observable in experiments exploring the interaction of charged particles with matter is usually the energy loss ΔE of the projectile ion. It is obtained by comparing the kinetic energy of the ion before and after passing through the target. The more detailed quantity is the stopping power which is defined as the energy change per unit path-length dE/ds and which corresponds to the actual decelerating force on the ion. The knowledge of the stopping power as function of energy allows then to determine the time evolution of ions in matter and further quantities, as e.g. the range of the projectile. The stopping power can directly be derived from the energy loss per path length as $dE/ds(v) = \Delta E/\Delta s$ provided ΔE and Δs remain sufficiently small, as it is often the case for experiments with heavy projectiles and thin targets as well as for simulation studies.

For most theoretical approaches the stopping power is more conveniently defined either by the change of its kinetic energy

$$dE/ds = \frac{1}{v}\frac{d}{dt}\langle P^2/2M \rangle \, , \tag{3}$$

or by the decelerating force as the change in the momentum of the projectile projected on the direction of motion

$$\mathrm{d}E/\mathrm{d}s = \frac{\boldsymbol{v}}{v} \cdot \boldsymbol{F} = \frac{\boldsymbol{v}}{v} \cdot \frac{\mathrm{d}}{\mathrm{d}t} \langle \boldsymbol{P} \rangle \ . \tag{4}$$

Both definitions are equivalent if the projectile travels along a straight line as it will be the case for sufficiently high projectile energies and/or large masses. Problems show up at very low projectile energy of the order of the mean kinetic energy of the target particles where the motion of the projectile represents a thermalization in the target and takes the character of Brownian motion with stochastically changing momenta. We concentrate now on the proper deceleration processes where the ion travels along a straight or smoothly varying path. This allows for a clearcut definition of a stopping power.

In the following we will work out a microscopic expression for the stopping power for the ion–target system Eq. (2). We will do that first for a fully quantum mechanical treatment where the state of the system is described by the density operator $\hat{\rho}(t)$ and reduce it later to classical models. For $t < t_0$ the ion is still absent and the target as defined by $\hat{H}_0$, Eq. (1), is assumed in a stationary state $\hat{\rho}_0 = \hat{\rho}(t < 0)$ with $[\hat{H}_0, \hat{\rho}_0] = 0$, i.e. typically in an equilibrium state like, e.g., $\hat{\rho}_0 = \exp(-\beta\hat{H}_0)/\mathrm{Tr}\exp(-\beta\hat{H}_0)$. For times $t > t_0$ the ion is present and the system evolves according to $i\hbar\partial\hat{\rho}(t)/\partial t = [\hat{H}, \hat{\rho}(t)]$ where $\hat{H}$ now denotes the full projectile–target Hamilton operator Eq. (2). With definition (4) the stopping power for $t > t_0$ reads

$$\frac{\mathrm{d}E}{\mathrm{d}s} = \frac{\boldsymbol{v}}{v} \cdot \frac{\mathrm{d}}{\mathrm{d}t} \mathrm{Tr}\hat{\rho}(t)\hat{\boldsymbol{P}} = \frac{\boldsymbol{v}}{v} \cdot \frac{1}{i\hbar} \mathrm{Tr}[\hat{H}, \hat{\rho}(t)]\hat{\boldsymbol{P}} = \frac{\boldsymbol{v}}{v} \cdot \frac{1}{i\hbar} \mathrm{Tr}\hat{\rho}(t)[\hat{\boldsymbol{P}}, \hat{H}]$$

$$= -\frac{\boldsymbol{v}}{v} \cdot \frac{1}{i\hbar} \mathrm{Tr}\hat{\rho}(t)[\hat{\boldsymbol{P}}, \sum_i e\phi_\mathrm{p}(\hat{\boldsymbol{r}}_i - \hat{\boldsymbol{R}})] = \frac{\boldsymbol{v}}{v} \cdot \mathrm{Tr}\hat{\rho}(t)\sum_i e\nabla_R\phi_\mathrm{p}(\hat{\boldsymbol{r}}_i - \hat{\boldsymbol{R}}) \ .$$

The expectation value recurs only to the ion and one electron coordinate. It is thus useful to introduce the reduced density

$$\rho_2(\boldsymbol{r}, \boldsymbol{R}, t) = \sum_i \int \mathrm{d}^3 r_i \, \delta^3(\boldsymbol{r} - \boldsymbol{r}_i) \prod_{j \neq i} \int \mathrm{d}^3 r_j \langle \boldsymbol{r}_1, \ldots, \boldsymbol{r}_N, \boldsymbol{R} | \hat{\rho}(t) | \boldsymbol{r}_1, \ldots, \boldsymbol{r}_N, \boldsymbol{R} \rangle \ .$$

This allows to express the stopping power finally as

$$\frac{\mathrm{d}E}{\mathrm{d}s} = -\int \mathrm{d}^3 r \int \mathrm{d}^3 R \, \rho_2(\boldsymbol{r}, \boldsymbol{R}, t) \frac{\boldsymbol{v}}{v} \cdot e\nabla_r\phi_\mathrm{p}(\boldsymbol{r} - \boldsymbol{R}) \ . \tag{5}$$

This very general expression allows to determine the stopping power from any kind of theoretical treatment which provides the probability to find at time t an electron at location $\boldsymbol{r}$ and the projectile at $\boldsymbol{R}$. The expression can be simplified for high projectile mass and energy where we can assume a classical behavior of the projectile with simultaneously known position and velocity. The projectile trajectory is given by the density $\delta^3(\boldsymbol{R} - \boldsymbol{v}t)$ where $\boldsymbol{v} = \boldsymbol{v}(t)$ varies only slowly on the time scale of the target–projectile and intra-target interactions. This allows for the approximation $\rho_2(\boldsymbol{r}, \boldsymbol{R}, t) \approx \rho_1(\boldsymbol{r}, t)\delta^3(\boldsymbol{R} - \boldsymbol{v}t)$ where $\rho_1(\boldsymbol{r}, t)$ is the electronic density at location $\boldsymbol{r}$. Now the stopping

power can be expressed in terms of the electric field $\mathscr{E}$ at the projectile location $\boldsymbol{R} = \boldsymbol{v}t$ created by the electronic charge density $\varrho(\boldsymbol{r}, t) = -e\rho_1(\boldsymbol{r}, t)$

$$\frac{\mathrm{d}E}{\mathrm{d}s} = \int \mathrm{d}^3 r\, \varrho(\boldsymbol{r}, t)\frac{\boldsymbol{v}}{v}\cdot \nabla_r \phi_{\mathrm{p}}(\boldsymbol{r} - \boldsymbol{v}t) = Ze\frac{\boldsymbol{v}}{v}\cdot \mathscr{E}(\boldsymbol{v}t, t) , \tag{6}$$

when employing $\phi_{\mathrm{p}}(\boldsymbol{r}) = Ze/4\pi\varepsilon_0|\boldsymbol{r}|$.

Expression (6) corresponds to the straightforward definition of the stopping power in a simple classical picture for the ion where the force on the ion is directly related to the electric field. Here it was derived from a fully quantal approach together with the additional assumptions of high projectile mass. The expression (6) becomes a rigorous result in the limit of infinite projectile mass ($M \to \infty$). For the derivation see Appendix B.1. The ion moves then with constant velocity and acts just as an external moving potential $\phi_{\mathrm{p}}(\hat{\boldsymbol{r}} - \boldsymbol{v}t)$. There is a stationary solution with constant flow for this type of potential. Thus the stopping power is expected to become time independent after a transient period due to switching on the interaction at t_0. Hence

$$\frac{\mathrm{d}E}{\mathrm{d}s} \overset{t \to \infty}{\to} Ze\frac{\boldsymbol{v}}{v}\cdot \mathscr{E}(\boldsymbol{v}t) , \tag{7}$$

in contrast to definitions (5) and (6), where the stopping power can depend on time due to the feedback of the stopping on the projectile velocity $\boldsymbol{v}(t)$.

Several theoretical methods describe the state of a system in terms of a phase space distribution function $f_N(\boldsymbol{p}_1, \ldots, \boldsymbol{p}_N, \boldsymbol{P}, \boldsymbol{r}_1, \ldots, \boldsymbol{r}_N, \boldsymbol{R}, t)$, e.g. for classical ensembles [108]. The stopping power is then obtained from a phase space integral which reduces to an integral over the one-particle distribution for the projectile $f(\boldsymbol{P}, \boldsymbol{R}, t)$. Starting from definition (4) we obtain

$$\frac{\mathrm{d}E}{\mathrm{d}s} = \frac{\boldsymbol{v}}{v}\cdot \int \mathrm{d}^3 p_1 \cdots \mathrm{d}^3 p_N\, \mathrm{d}^3 P \int \mathrm{d}^3 r_1 \cdots \mathrm{d}^3 r_N\, \mathrm{d}^3 R\, \boldsymbol{P}\frac{\partial f_N}{\partial t}$$

$$= \frac{\boldsymbol{v}}{v}\cdot \int \mathrm{d}^3 P\, \boldsymbol{P} \int \mathrm{d}^3 R\, \frac{\partial f(\boldsymbol{P}, \boldsymbol{R}, t)}{\partial t} . \tag{8}$$

Here the time evolution of $f(\boldsymbol{P}, \boldsymbol{R}, t)$ is to be determined from the corresponding kinetic equations.

The definitions of the stopping introduced above are of course not restricted to the case of an electron target plasma. They apply as well for more complex target systems as gases, solids, fluids and two- or multi-component plasmas. To extend the previous considerations to any kind of target consisting of electrons ($q_i = -e$, $m_i = m$) and one or more species of nuclei ($q_i = Z_i e$, m_i), one has just to replace the target hamiltonian $\hat{H}_0$ (1) by the more general

$$\hat{H}_0^\star = \sum_i \frac{\hat{\boldsymbol{p}}_i^2}{2m_i} + \sum_i \sum_{j \neq i} \frac{q_i q_j}{4\pi\varepsilon_0|\hat{\boldsymbol{r}}_i - \hat{\boldsymbol{r}}_j|} , \tag{9}$$

with $\sum_i q_i = 0$ for neutral systems. The extended projectile–target system is then described by

$$\hat{H}^\star(t) = \hat{H}_0^\star + \frac{\hat{\boldsymbol{P}}^2}{2M} + \theta(t - t_0)\sum_i q_i \phi_{\mathrm{p}}(\hat{\boldsymbol{r}}_i - \hat{\boldsymbol{R}}) . \tag{10}$$

2.3. Parameters characterizing the projectile–target system

The energy loss of an ion impinging on an electron target plasma is determined by the direct interaction of the ion with the target electrons and by the interparticle correlations within the target. Hence, it is necessary to characterize the ion–target system in two respects: first, concerning the strength of the ion–target coupling, and second, concerning the electron–electron correlations in the plasma target. This will be done in the following two subsections. Since we have the impression, that the ion–target coupling is not always paid sufficient attention in the literature, we will address this point in particular. Thus we have a double sorting of strengths distinguishing ideal and nonideal target conditions as well as linear, semilinear, and nonlinear ion–target coupling. Each one of the resulting regimes requires its own theoretical approaches to the stopping power. These will be reviewed subsequently in Section 3.

2.3.1. The electron target

The parameter of ideality ξ for an electron plasma is defined as the ratio of the mean potential energy E_{pot} of the electron interaction to the mean kinetic energy E_{kin} of the electrons. The first one can be estimated by the potential energy for two electrons separated by the distance $a = (4\pi n/3)^{-1/3}$, the Wigner–Seitz radius for an electron density n. For the mean kinetic energy, we take a simple interpolation $E_{\mathrm{kin}} = E_{\mathrm{F}} + k_{\mathrm{B}}T$ between the Fermi-energy E_{F} for a fully degenerate plasma with temperature $T = 0$ and the thermal energy $k_{\mathrm{B}}T$ for a hot, nondegenerate plasma. The parameter measuring the ideality becomes thus

$$\xi = \frac{E_{\mathrm{pot}}}{E_{\mathrm{kin}}} = \frac{e^2}{4\pi\varepsilon_0 a(E_{\mathrm{F}} + k_{\mathrm{B}}T)} = \frac{2\alpha^2 r_{\mathrm{s}}}{1 + \Theta} \,, \tag{11}$$

where $r_{\mathrm{s}} = a/a_0$, a_0 is the Bohr radius and $\alpha = (4/9\pi)^{1/3} = 0.521\ldots$. For small $\xi \ll 1$ the behavior of the electron plasma is dominated by the kinetic energy of the electrons and we are in an ideal, collisionless regime where collective plasma phenomena prevail. Increasing $\xi \geq 1$ corresponds to a strongly coupled, nonideal electron plasma with increasing importance of interparticle correlations.

The definition of ξ in Eq. (11) implied already a further definition characterizing target conditions. There we introduced the degree of degeneracy

$$\Theta = \frac{k_{\mathrm{B}}T}{E_{\mathrm{F}}} = 2\frac{v_{\mathrm{th}}^2}{v_{\mathrm{F}}^2} = 2\alpha^2 \left(\frac{a}{\Lambda}\right)^2 = \frac{k_{\mathrm{B}}T}{13.6\,\mathrm{eV}}(\alpha r_{\mathrm{s}})^2 \,, \tag{12}$$

as the ratio of the thermal energy $k_{\mathrm{B}}T = mv_{\mathrm{th}}^2$ to the Fermi energy $E_{\mathrm{F}} = mv_{\mathrm{F}}^2/2$. Alternatively, one can view it as the ratio of the interparticle distance a to the thermal wavelength $\Lambda = \hbar/mv_{\mathrm{th}}$ where m is the electron mass, $v_{\mathrm{th}} = (k_{\mathrm{B}}T/m)^{1/2}$ the thermal velocity and v_{F} the Fermi velocity. This parameter Θ represents a measure for the importance of the Pauli exclusion principle. The electrons have to obey Fermi–Dirac statistics for $\Theta \ll 1$ and can be treated classically within Boltzmann statistics for $\Theta \gg 1$. For nondegenerate plasmas, $\Theta \gg 1$, the parameter of ideality ξ becomes identical to the classical plasma parameter Γ, defined as

$$\Gamma = \frac{e^2}{4\pi\varepsilon_0 a k_{\mathrm{B}}T} = \frac{2\alpha^2 r_{\mathrm{s}}}{\Theta} \overset{1 \ll \Theta}{\longleftarrow} \xi \,. \tag{13}$$

There is one more criterion to be checked. It is the Coulomb parameter

$$\eta_e = \frac{e^2}{4\pi\varepsilon_0 \hbar v_r}$$

which is concerned with the quantum mechanical wave nature of the interacting electrons. Taking for the relative velocity v_r the averaged relative velocity $\langle v_{ee} \rangle$ between two electrons within the target we arrive at the averaged Coulomb parameter

$$\langle \eta_e \rangle = \frac{e^2}{4\pi\varepsilon_0 \hbar \langle v_{ee} \rangle} = \frac{\alpha r_s}{\langle v_{ee} \rangle' \sqrt{1 + (\Theta/2)}} \overset{\Theta \gg 1}{\to} \sqrt{\frac{13.6\,\text{eV}}{k_B T}} \,, \tag{14}$$

where we further introduced the dimensionless relative velocity $\langle v_{ee} \rangle' = \langle v_{ee} \rangle / \langle v_e \rangle$ scaled in units of the averaged (single) electron velocity $\langle v_e \rangle$. The more specific $\langle v_{ee} \rangle = 2^{1/2} \langle v_e \rangle$ can be derived in the limit of a nondegenerate plasma ($\Theta > 1$) with a Maxwell velocity distribution. Classical motion is a good approximation if $\eta_e, \langle \eta_e \rangle \gg 1$ and a quantum mechanical treatment is necessary for $\eta_e, \langle \eta_e \rangle < 1$.

The various regimes of target conditions are visualized in the left part of Fig. 1. The different regimes of target conditions are displayed in the n–T plane of the electron plasma. The dash-dotted
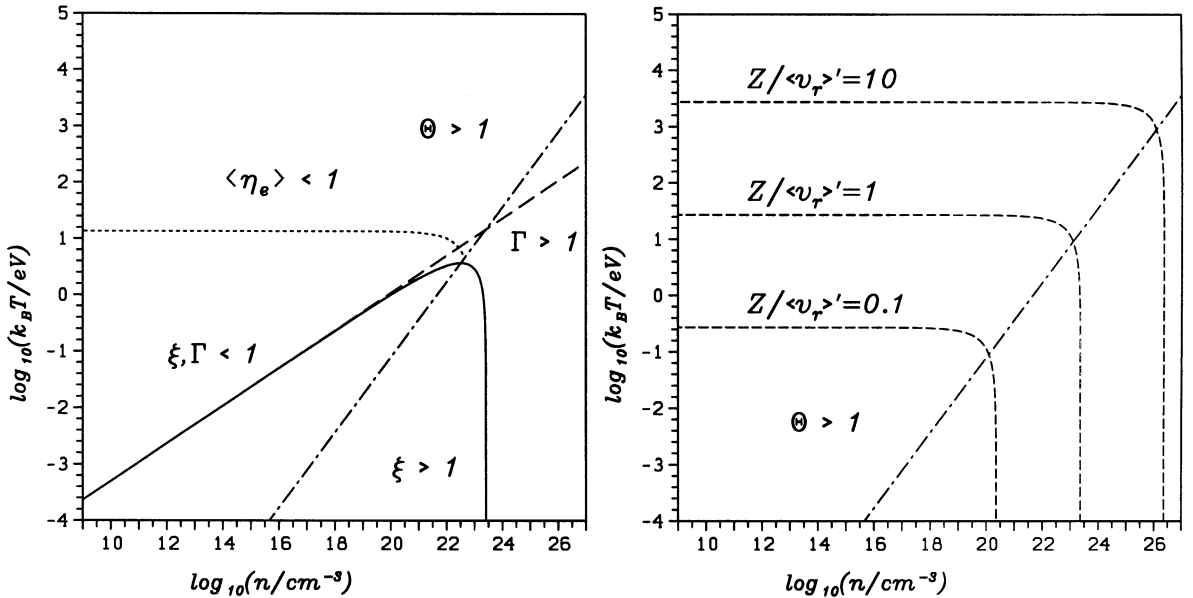

Fig. 1. The n–T regions of different conditions for an electron plasma. *Left plot*: The nonideal plasmas $\xi > 1$ are located below the solid curve $\xi = 1$. The long-dashed line represents $\Gamma = 1$. The dash-dotted line $\Theta = 1$ separates the classical plasmas $\Theta > 1$ (above) from the quantum plasmas $\Theta < 1$. Below the dotted curve ($\langle \eta_e \rangle = 1$) and above the dash-dotted one ($\Theta = 1$) the electron–electron collisions can be treated classically. *Right plot*: The dashed curves $\langle \eta_p \rangle = 1$, for different ratios $|Z|/\langle v_r \rangle' = 10, 1, 0.1$ of the ion charge to the relative velocity, demarcate the region $\langle \eta_p \rangle > 1$ (to left bottom) where a classical description of ion–electron collisions is appropriate.

curve represents the critical degree of degeneracy $\Theta = 1$. The degenerate regime $\Theta < 1$ where the Pauli principle becomes important extends towards higher densities, i.e. below the dash-dotted division line. The solid curve corresponds to the critical ideality $\xi = 1$. Nonideal plasmas are located in the triangle below the solid curve. The long dashed curve indicates the classical plasma parameter $\Gamma = 1$. It deviates from the line $\xi = 1$ only in the degenerate regime $\Theta < 1$. The electronic Coulomb parameter $\langle \eta_e \rangle = 1$ is drawn as dotted line in the nondegenerate region. A classical treatment of the electrons is possible in the region below that line, and, of course, above the dash-dotted degeneracy line $\Theta = 1$.

2.3.2. The ion–electron coupling

For the interaction of an electron and an ion with charge Z, the ratio of the classical collision diameter $b_0 = |Z|e^2/4\pi\varepsilon_0\mu v_r^2$ and the wavelength $\lambdabar_r = \hbar/\mu v_r$ related to the relative motion with reduced mass μ and velocity v_r defines the Coulomb- or Bloch-parameter

$$\eta_p = \frac{b_0}{\lambdabar_r} = \frac{|Z|e^2}{4\pi\varepsilon_0\hbar v_r} \ . \tag{15}$$

This parameter is the analogue to η_e as defined previously. It determines the transition point from a quantum-mechanical to a classical description of the Coulomb interaction of the particles. While a fast interaction with a large kinetic energy $\eta_p \ll 1$ can be described by a plane wave in first order Born approximation, low energetic collisions $\eta_p \gg 1$ allow for a treatment based on classical trajectories, particularly for high ion charges Z. The line $\eta_p = 1$ is the division line between quantal and classical Coulomb collisions. More precisely, the η_p should be defined in terms of an averaged velocity $\langle v_r \rangle$ of the relative motion as in the case of $\langle \eta_e \rangle$, Eq. (14). This yields

$$\langle \eta_p \rangle = \frac{|Z|e^2}{4\pi\varepsilon_0\hbar\langle v_r \rangle} = \frac{|Z|\alpha r_s}{\langle v_r \rangle'\sqrt{1 + (\Theta/2)}} \ . \tag{16}$$

Here the relative velocity $\langle v_r \rangle := \langle |\boldsymbol{v}_e - \boldsymbol{v}| \rangle$, its dimensionless form $\langle v_r \rangle'$ and the averaged electron velocity $\langle v_e \rangle$ are approximated and interpolated as

$$\langle v_r \rangle = (\langle v_e \rangle^2 + v^2)^{1/2} \ ,$$

$$\langle v_r \rangle' = \frac{\langle v_r \rangle}{\langle v_e \rangle} = \left(1 + \frac{v^2}{\langle v_e \rangle^2}\right)^{1/2} \ , \tag{17}$$

$$\langle v_e \rangle = (v_F^2 + v_{th}^2)^{1/2} = v_F\left(1 + \frac{\Theta}{2}\right)^{1/2} \ ,$$

in terms of the Fermi velocity v_F, the thermal velocity v_{th} and the ion velocity v.

The quantum or classical regimes for the ion–electron interaction are indicated in the right part of Fig. 1. The dashed curves $\langle \eta_p \rangle = 1$ are division lines between the classical regime $\langle \eta_p \rangle > 1$ extending towards lower temperatures and the quantal regime $\langle \eta_p \rangle < 1$ at higher T. Three different dashed curves are shown belonging to different ratios $Z/\langle v_r \rangle'$ as indicated. The scaled relative velocity is given by $\langle v_r \rangle' = \langle v_r \rangle/\langle v_e \rangle$. It is to be remarked, however, that the Coulomb parameters η_e and η_p decide only on the validity of a classical treatment for an isolated two-particle

scattering event. One has to be aware of the fact that there may appear other quantum interference effects in a many-body system.

The most important quantity to classify the ion–target coupling is the measure of the strength of the perturbation on the target caused by the ion. The strength parameter should decide whether one can treat the system in perturbation theory or not. To derive such a measure, we compare the potential energy of an electron in the field of the projectile ion with the electron energy in the absence of the ion but at the corresponding relative velocity. To that end, we need some preconceived knowledge of the potential field around the ion. It turns out that the potential energy can be approximated for the purpose of demarcation between regimes by

$$V_{ep}(r) = \frac{-Ze^2}{4\pi\varepsilon_0 r}\left[1 - \exp\left(-\frac{r}{\lambdabar_r}\right)\right]\exp\left(-\frac{r}{\lambda}\right). \tag{18}$$

The factor $\propto (1 - \exp(-r/\lambdabar_r))/r$ stands for the modification of the ionic Coulomb potential when explored by an electronic wavepacket centered at distance r and of width $\lambdabar_r = \hbar/mv_r$ (the reduced mass is replaced by the electron mass m for heavy projectiles). It parametrizes the quantum diffraction effects at short distances $\sim \lambdabar_r$. The other exponential factor $\exp(-r/\lambda)$ parametrizes the long-range screening. Here we ignore all details of dynamical polarization and assume an exponential behavior for the effective screening with a velocity dependent screening length λ. The well-known behavior for ideal plasmas and weak perturbations is $\lambda = \langle v_r \rangle/\omega_p$ where $\omega_p = (e^2 n/m\varepsilon_0)^{1/2}$ is the plasma frequency. More complicated, but still local forms for the screening may be needed in other regimes. Here, the local potential energy (18) serves to derive a definition of the various ion–target coupling regimes. Its explicit form is of minor importance provided that one properly incorporates both important physical phenomena, the wave nature of the electrons and the collective screening effects, and chooses the related parameters $\lambdabar_r$ and λ appropriately. While screening results in a decay faster than $1/r$ on large distances of the order of $r \sim \lambda$, the wave nature of the electrons modifies the Coulomb potential for $r \lesssim \lambdabar_r$ and results for decreasing r in a transition from the $1/r$ behavior to $V_{ep}(r \to 0) \propto 1/\lambdabar_r$, when the wavepacket is centered on the ion. This behavior is approximated by the simple exponential form $V_{ep}(r) \propto (1 - \exp(-r/\lambdabar_r))/r$ (18).

The relevant strength φ of the ion–electron coupling is now given by the ratio of the ion–electron potential to the average electron energy E_e in the target. We need yet to estimate this electron energy E_e. One important ingredient is, of course, the kinetic energy $E_{kin} = m\langle v_r \rangle^2/2$. The potential energy of the electron in its interaction with the other electrons (and the background) can be expressed in terms of the ideality ξ as $E_{pot} = m\langle v_e \rangle^2 \xi/2$. Thus we obtain for the average electron energy $E_e = m\langle v_r \rangle^2/2 + m\langle v_e \rangle^2 \xi/2$ and finally the local strength as

$$\varphi(r) = \frac{2|\langle V_{ep}(r)\rangle|}{m\langle v_r \rangle^2 + m\langle v_e \rangle^2 \xi} = \frac{2\langle b_0 \rangle}{r}\frac{\langle v_r \rangle'^2}{\langle v_r \rangle'^2 + \xi}\left[1 - \exp\left(-\frac{r}{\langle \lambdabar_r \rangle}\right)\right]\exp\left(-\frac{r}{\lambda}\right), \tag{19}$$

where $\langle b_0 \rangle = |Z|e^2/4\pi\varepsilon_0 m\langle v_r \rangle^2$, $\langle \lambdabar_r \rangle = \hbar/m\langle v_r \rangle$ and the scaled relative velocity $\langle v_r \rangle' = (1 + v^2/\langle v_e \rangle^2)^{1/2} \geq 1$ as introduced in Eq. (17). In an analogue manner, the electron–electron interaction can be quantified by a local strength $\varphi_{ee}(r) = 2|\langle V_{ee}(r)\rangle|/m\langle v_{ee} \rangle^2$. Here, the electron–electron potential energy $V_{ee}(r)$ emerges from the potential energy (18) by replacing the ion charge Ze with the electron charge $-e$ and taking the averages $\langle \cdots \rangle$ over the relative

motion of the electrons only, that is, using $\langle v_{\mathrm{ee}} \rangle$ instead of the relative ion–electron velocity $\langle v_{\mathrm{r}} \rangle$. The local quantity $\varphi_{\mathrm{ee}}(r)$ is relevant for electron–electron collisions while an average over the distances r will characterize the global regimes of the electron–electron coupling in the target. Approximating such an average by evaluating φ_{ee} at the typical inter electron distance a yields

$$\varphi_{\mathrm{ee}}(r = a) = \frac{2|\langle V_{\mathrm{ee}}(a) \rangle|}{m \langle v_{\mathrm{ee}} \rangle^2} = \frac{e^2}{4\pi\varepsilon_0 a} \frac{2}{m \langle v_{\mathrm{ee}} \rangle^2} \left[1 - \exp\left(-\frac{a}{\langle \lambdabar_{\mathrm{ee}} \rangle} \right) \right] \exp\left(-\frac{a}{\lambda} \right)$$

$$\approx \frac{e^2}{4\pi\varepsilon_0 a (E_{\mathrm{F}} + k_{\mathrm{B}} T)} = \xi \; ,$$

noting that $a/\lambda < 1$ and $a/\langle \lambdabar_{\mathrm{ee}} \rangle = am \langle v_{\mathrm{ee}} \rangle / \hbar > am v_{\mathrm{F}} / \hbar = 1/\alpha \approx 2$ (see Eq. (12)) for all densities and temperatures. Thus, the local electron–electron interaction strength φ_{ee} leads directly back to the parameter of ideality (11) as a measure of the coupling within the target. The dimensionless local strength $\varphi(r)$ of the ion–electron interaction, Eq. (19), on the other hand, allows to distinguish the various regimes of ion–electron coupling.

The most simple regime is the case of a weak perturbation where lowest order perturbation theory is applicable. This can be handled with linear response techniques and therefore it is called the regime of *linear ion–electron coupling*. It requires a weak potential energy at all distances, that is, $\varphi(r) \ll 1$ for all r. Since $\varphi(0) \geq \varphi(r)$, the corresponding parameter of linearity is

$$\varphi(0) = \frac{2\langle b_0 \rangle}{\langle \lambdabar_{\mathrm{r}} \rangle} \frac{\langle v_{\mathrm{r}} \rangle'^2}{\langle v_{\mathrm{r}} \rangle'^2 + \xi} = 2\langle \eta_{\mathrm{p}} \rangle \frac{\langle v_{\mathrm{r}} \rangle'^2}{\langle v_{\mathrm{r}} \rangle'^2 + \xi} = |Z| \xi \frac{1 + \Theta}{\alpha \sqrt{1 + (\Theta/2)}} \frac{\langle v_{\mathrm{r}} \rangle'}{\langle v_{\mathrm{r}} \rangle'^2 + \xi} \; , \tag{20}$$

where linear ion–target coupling is granted for $\varphi(0) \ll 1$. Here we employed for the last step expression (16) for $\langle \eta_{\mathrm{p}} \rangle$ and the definition (11) of the parameter of ideality ξ to rewrite $\varphi(0)$ (20) in terms of Z, ξ and Θ. Inspecting now the condition for linear coupling $\varphi(0) \ll 1$ and keeping in mind that $\langle v_{\mathrm{r}} \rangle' \geq 1$, we conclude that $\varphi(0) \ll 1$ can be achieved only for $\xi \ll 1$ or large velocities $\langle v_{\mathrm{r}} \rangle' \gg \xi$ resulting in $\langle v_{\mathrm{r}} \rangle'^2 / (\langle v_{\mathrm{r}} \rangle'^2 + \xi) \approx 1$. Thus small $\varphi(0)$ and small $\langle \eta_{\mathrm{p}} \rangle$ are equivalent:

$$\varphi(0) \ll 1 \; \leftrightarrow \; 2\langle \eta_{\mathrm{p}} \rangle \ll 1 \; . \tag{21}$$

In summary, the Coulomb-parameter $\langle \eta_{\mathrm{p}} \rangle = 1$ separates the regimes of weak and strong perturbation, that is of linear and nonlinear ion target coupling in coincidence with the regimes of quantum-mechanical and classical ion–electron scattering. To illustrate this additional significance of $\langle \eta_{\mathrm{p}} \rangle$ as a measure of linearity, we reconsider the three dashed curves in the right part of Fig. 1 representing the division lines $\langle \eta_{\mathrm{p}} \rangle = 1$. They mark the boundary of the linear regime $\langle \eta_{\mathrm{p}} \rangle < 1$ located at higher temperatures and densities for an ion with $Z = 10$ and three different velocities, low $v \ll \langle v_{\mathrm{e}} \rangle$, high $v \approx 10 \langle v_{\mathrm{e}} \rangle$ and very high $v = 100 \langle v_{\mathrm{e}} \rangle$ as indicated. For comparison, for an ion with $Z = 1$ the last two curves would correspond to $v \ll \langle v_{\mathrm{e}} \rangle$ and $v \approx 10 \langle v_{\mathrm{e}} \rangle$. The ion–target coupling is linear in most of the ideal plasma regime ($\xi < 1$) if Z is sufficiently low or the velocities are sufficiently high. For high charges and/or low velocities the linear regime is reached only for extreme temperatures and densities. As mentioned, the value $\langle \eta_{\mathrm{p}} \rangle = 1$ is also the division line between classical and quantal electron–ion scattering and it is interesting to note that truly linear coupling will occur only in quantal regime. That is understandable from the effective local potential energy (18). The quantum smoothing expressed in the factor $[1 - \exp(-r/\lambdabar_{\mathrm{r}})]$ is required to suppress the $1/r$ singularity of the naked Coulomb potential. Alternative checks for the significance

of η_p, $\langle \eta_p \rangle$ as a measure of the ion–electron coupling strength and for the consistency of the linear coupling Eqs. (18)–(21) are given in Appendix B.2. There fully quantum mechanical approaches are considered which confirm the definitions obtained above which are essentially based on the semiclassical expression for the potential energy (18).

The transition to a nonlinear regime with increasing $\langle \eta_p \rangle \geq 1$ proceeds gradually and there comes first an intermediate regime where the coupling (19) remains weak almost everywhere except for a small volume next to the origin. Simple approaches can still work very well in this transitional regime and it is thus useful to single it out by its own name. We call it the regime of *semilinear ion–target coupling*. We reconsider the local condition for a weak perturbation $\varphi(r) \leq 1$ and introduce a critical distance $r_c > 0$. The ion remains locally a weak perturbation for $r > r_c$ where $\varphi(r) < \varphi(r_c)$, and represents a strong perturbation only for $r < r_c$ (and, of course, no perturbation at all for $r > \lambda$). The region of a strong perturbation at small r requires special attention in a theoretical description of stopping. But simple solutions are still feasible if the volume of strong perturbation, $\propto r_c^3$, remains small. The definition of the semilinear regime is thus

$$\frac{r_c}{\lambda} \ll 1, \qquad \varphi(r_c) = 1, \qquad \langle \eta_p \rangle > 1 \ . \tag{22}$$

The definition of r_c, i.e. $\varphi(r_c) = 1$ can be resolved approximately using Eq. (19) for $\langle \eta_p \rangle > 1$ (i.e. $r_c > \langle \lambdabar_r \rangle$) and assuming $r_c \ll \lambda$. This yields $r_c \gtrsim \langle b_0 \rangle$ and we can use $r_c \approx \langle b_0 \rangle$ for further estimates. The regime of the semilinear ion–target coupling is then demarcated by

$$\frac{\langle b_0 \rangle}{\lambda} < 1, \qquad \langle \eta_p \rangle > 1 \tag{23}$$

and larger values of this ratio $\langle b_0 \rangle / \lambda$ hint at an essentially nonlinear coupling. For ideal electron targets $\xi \ll 1$ the effective screening length is $\lambda = \langle v_r \rangle / \omega_p$. For nonideal targets the static screening will change, but the dynamical screening for high velocities $v \approx \langle v_r \rangle \gg \langle v_e \rangle$ still has the form $\lambda = \langle v_r \rangle / \omega_p = v/\omega_p$ because the time for plasma response remains ω_p^{-1} as in an ideal plasma. Hence, for ideal targets or high velocities the parameter $\langle b_0 \rangle / \lambda$ can be expressed as

$$\frac{\langle b_0 \rangle}{\lambda} = \frac{|Z|e^2\omega_p}{4\pi\varepsilon_0 m \langle v_r \rangle^3} = \frac{2|Z|}{\sqrt{3\pi}\langle v_r \rangle'^3}\left(\frac{\alpha r_s}{1+(\Theta/2)}\right)^{3/2} . \tag{24}$$

Here the semilinear regime ($\langle b_0 \rangle / \lambda < 1$, $\langle \eta_p \rangle > 1$) is located in the n–T plane between the two boundaries $\langle \eta_p \rangle = 1$ and $\langle b_0 \rangle / \lambda = 1$ to the linear regime and the (essentially) nonlinear one, respectively. This is shown in Fig. 2 for an ion with $Z = 10$, where the dashed curves indicate $\langle \eta_p \rangle = 1$ and the dotted curves $\langle b_0 \rangle / \lambda = 1$ for a relative velocity $\langle v_r \rangle' = 1$ (left plot) and 10 (right). There is a large region of densities and temperatures where the ion–target coupling for highly charged ions is semilinear, in particular for non-degenerate plasmas $\Theta \gg 1$. In the latter case we have $\langle v_e \rangle = v_{th}$ and for $\xi < 1$ or $v \gg v_{th}$ the screening length $\lambda = \langle v_r \rangle / \omega_p = v_{th}(1+(v/v_{th})^2)^{1/2}/\omega_p = \lambda_D(1+(v/v_{th})^2)^{1/2}$ where λ_D is the Debye length. Here the critical ratio reads

$$\frac{\langle b_0 \rangle}{\lambda} = \frac{\sqrt{3}|Z|\Gamma^{3/2}}{(1+(v^2/v_{th}^2))^{3/2}} = \frac{|Z|}{4\pi n\lambda_D^3(1+(v^2/v_{th}^2))^{3/2}} = \frac{|Z|}{N_D}\frac{1}{3(1+(v^2/v_{th}^2))^{3/2}} , \tag{25}$$
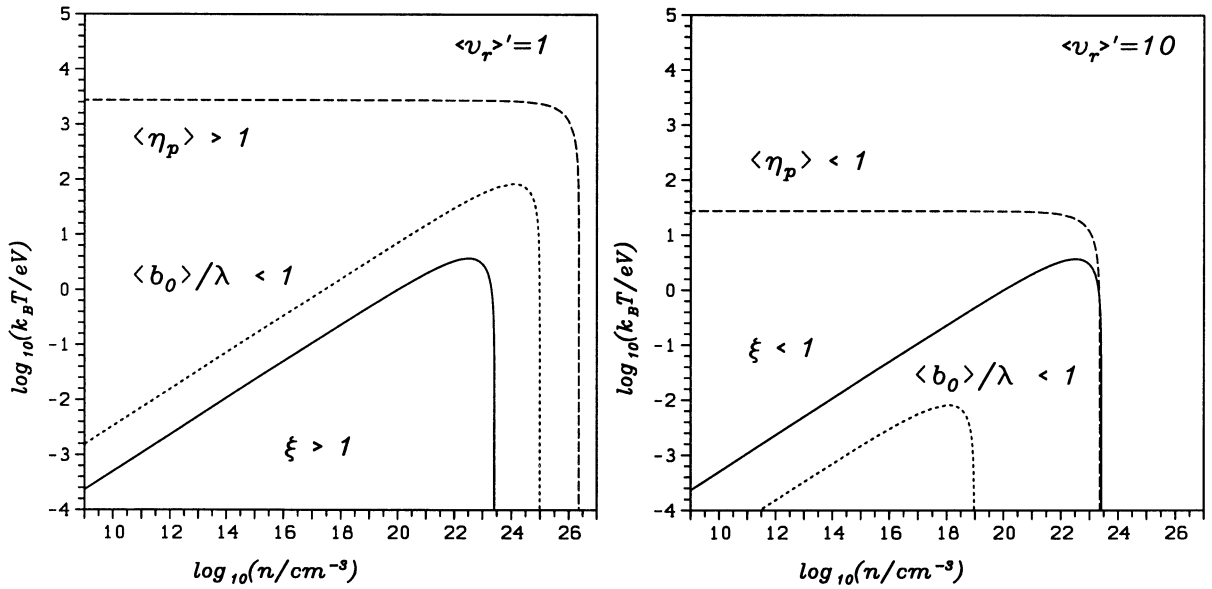
Fig. 2. The regions of ion–target coupling for an ion of charge $Z = 10$ in an electron plasma. The dashed curves represent $\langle \eta_p \rangle = 1$ and separate the linear regime ($\langle \eta_p \rangle < 1$) from the semilinear regime ($\langle \eta_p \rangle > 1, \langle b_0 \rangle / \lambda < 1$) located between the linear regime and the boundary ($\langle b_0 \rangle / \lambda = 1$, dotted curves) to the proper nonlinear one. The corresponding relative velocities are $\langle v_r \rangle' = 1$ (left plot) and 10 (right plot) in units of $\langle v_e \rangle = (v_F^2 + v_{th}^2)^{1/2}$. The solid curve is again the boundary $\xi = 1$ between ideal and nonideal electron targets.

where Γ is the classical plasma parameter (13) and $N_D = 4\pi n \lambda_D^3 / 3$ is the number of electrons in a Debye sphere. In condition (23) together with expression (25) we recover the well-known condition to describe the stopping in classical plasmas by the dielectric formalism. There the ion charge state has to be small compared to the number of electrons N_D in a Debye sphere or, more precisely, to the number $N_D(1 + (v/v_{th})^2)^{3/2}$ in the dynamical screening sphere [135], in order to ensure that each electron contributes only slightly to the screening or, more generally, to the target response.

In summary, there exist for given target conditions and ion charge two critical velocities, v_1 from Eq. (24) and $v_2 > v_1$ from Eqs. (16) and (21): the ion–target coupling is linear for ion velocities $v \geq v_2$, semilinear for $v_1 \leq v < v_2$ and nonlinear for $v < v_1$. Of course, v_1 or both velocities v_1 and v_2 may be zero in certain cases and only semilinear and linear or only linear coupling occurs, respectively. In fact, reality is a bit more involved because the effective ion charge depends on the projectile velocity and hence v_1 and v_2 should also vary with velocity. Nevertheless, the critical velocities serve as a useful sorting criterion delivering this sequence of the three different coupling regimes.

The criteria outlined above have been concerned exclusively with the electronic component of the target plasma. The ionic component of the target has been assumed tacitly as a homogeneous static charge neutralizing background. However, the discussed regimes and the corresponding definitions can be applied as well to the target ions by mainly replacing the electron mass and

charge by the mass and charge of the target ions. Furthermore, the outlined classification of the target coupling regimes in terms of the ratio $\varphi(r)$ (cf. Eq. (19)) of a potential energy $V_{ep}(r)$ to the mean energy of an electron can be used for a much larger spectrum of ion–target systems. For instance, the potential energy for electrons in the field of an extended charge distribution related to the bound states of not completely stripped projectile ions can be introduced if the extension of the ion ($\gtrsim \langle \lambda_r \rangle$) does not allow to use the bare Coulomb potential of a pointlike effective charge as employed throughout the previous discussion. When in addition stopping by bound target electrons is considered, the criterion for ion–target coupling strength should be altered by taking into account the binding energy of the electrons bound to the target ions/atoms. There, the coupling strength at low projectile velocities is measured with reference to the binding/ionization energy of the bound electrons which replaces now the kinetic energy of the free electrons in the expression for the mean electron energy.

3. Stopping of heavy ions by free electrons in the various regimes

As outlined above, we distinguish the regimes of an ion–plasma system in two respects: ideality and linearity. The target parameters density n and temperature T define the degree of ideality while the projectile properties charge Z and velocity v have a strong impact on the degree of linearity. Hence stopping at strong coupling can take place in three different scenarios: linear stopping in nonideal plasmas, nonlinear stopping in ideal plasmas, or nonlinear stopping in nonideal plasmas. The description of the energy loss in these different cases deals mainly with the question of how rigorously one has to treat the electron–electron interaction in the presence of the ion. In this section we review the existing methods and recent proposals for the description of the (electronic) stopping in the various regimes. The sections are sorted with respect to the degree of ion–target coupling.

3.1. Linear ion–target coupling

It is the main feature of the linear ion–target coupling regime that it is possible to separate the correlations within the target from those between the ion and the target. The projectile can be considered as a weak perturbation such that its effect on the target can be treated within linear response. There the dynamic response for a momentum transfer $\hbar k$ and an energy transfer $\hbar \omega$ is given in terms of the dielectric function $\varepsilon(k, \omega)$ which contains all necessary information about the internal structure of the target. We will discuss in this subsection the approaches which are based on the dielectric formulation. This is done in the following steps: In Section 3.1.1 we define and discuss the key quantities of linear response and their interrelations. The linear response formulation of the stopping power is then introduced in Section 3.1.2. The RPA formulation for the dielectric function is presented in Section 3.1.3. It is appropriate for ideal targets. Nonideal targets require higher correlations as outlined in Section 3.1.4. These are usually treated by density functional theories which aim to incorporate all higher correlations into an effective interaction while maintaining the simple structure of linear response. There are two mainstreams in these approaches, the Kohn–Sham equations with energy-density functionals derived in local density approximation (LDA) and the technique of the local field corrections (LFC). The Kohn–Sham

approach is also applicable in the regime of nonlinear coupling and mainly employed there. We thus postpone its description to Section 3.3.5. Here we restrict the discussions to the LFC and spend two subsections to outline two important and widely used classes of approaches to the LFC: the STLS approximations in Section 3.1.5 and the HNC scheme in Section 3.1.6. There exists a somewhat different class of approaches where nonideality effects are described in Markovian approximation through electron–electron collisions, most often further simplified through a relax-ation-time approximation to the collision integral. This is discussed in Section 3.1.7. Finally, we comment briefly on perturbative expansions for higher order corrections in Section 3.1.8.

A very different approach to the energy loss of an ion rests on a purely kinetic description for the electrons. This is conceivable for an ideal target with sufficiently weak interaction between the electrons. The stopping can then be deduced as result of independent successive binary ion–electron collisions. Collective phenomena as screening and plasmon excitations are included by using an appropriate effective ion–electron interaction which, however, needs to be determined carefully. Since such an approach is a priori not restricted to linear ion–target coupling and turns out to become important mostly in the semilinear regime we postpone the discussion of the binary collision model for stopping to Section 3.2.1.

3.1.1. Different formulations of linear response

As basis for all further considerations we recall quickly the main aspects and quantities of linear response theory. Most directly related to the concept of linear response is the *density–density response function* χ which is defined from the relation between an external perturbing potential U_{ext} and the resulting density response δn as

$$\delta n(\boldsymbol{r}, t) = \int \mathrm{d}^3 r' \, \mathrm{d}t' \, \chi(\boldsymbol{r}, t; \boldsymbol{r}', t') U_{\text{ext}}(\boldsymbol{r}', t') \tag{26}$$

and which is to be computed from first order time dependent perturbation theory (see e.g. [54], Section 13). This involved operator definition becomes a simple algebraic equation for systems with a spatially homogeneous ground state. Then the response function χ depends only on the differences $\boldsymbol{r} - \boldsymbol{r}', t - t'$, and Fourier transformation in space and time (see Section B.3) yields

$$\delta n(\boldsymbol{k}, \omega) = \chi(\boldsymbol{k}, \omega) U_{\text{ext}}(\boldsymbol{k}, \omega) \,, \tag{27}$$

which we will consider as the defining relation for the response χ. Note that we are using the same symbols for the space–time dependent quantities as well as for the corresponding momentum–frequency dependent ones. This should not cause confusion as the distinction is usually clear from the context.

An alternative formulation of linear response uses the concept of the *dielectric function* ε which is defined from the relation between the external perturbation U_{ext} and the resulting total potential U_{tot} as

$$U_{\text{tot}}(\boldsymbol{k}, \omega) = \frac{1}{\varepsilon(\boldsymbol{k}, \omega)} U_{\text{ext}}(\boldsymbol{k}, \omega) \,, \tag{28}$$

which is here already written in its simpler form in Fourier space. This equation is the analogue of Eq. (27) defining the response function χ. Both quantities are, in fact, fully equivalent and represent

merely a different emphasis in their definition. The response density δn of Eq. (27) yields the induced potential

$$U_{\text{ind}}(\boldsymbol{k}, \omega) = V(\boldsymbol{k})\delta n(\boldsymbol{k}, \omega) \,, \tag{29}$$

where $V(\boldsymbol{k})$ is the Fourier transformed two-body interaction potential, in case of electron systems the repulsive Coulomb potential $V(\boldsymbol{k}) = e^2/\varepsilon_0 k^2$. The induced potential adds up together with the external potential to the total potential, i.e. $U_{\text{tot}} = U_{\text{ext}} + U_{\text{ind}}$. Combining all this information establishes the expected one-to-one relation

$$\chi(\boldsymbol{k}, \omega) = \frac{1}{V(\boldsymbol{k})}\left(\frac{1}{\varepsilon(\boldsymbol{k}, \omega)} - 1\right) \tag{30}$$

or its reverse

$$\varepsilon(\boldsymbol{k}, \omega) = \frac{1}{1 + V(\boldsymbol{k})\chi(\boldsymbol{k}, \omega)} \,. \tag{31}$$

The response functions χ, ε carry similar physical information as the *dynamical structure factor*

$$S(\boldsymbol{k}, \omega) = \int \mathrm{d}^3 r \int_{-\infty}^{\infty} \mathrm{d}t \, \langle \delta n(\boldsymbol{r}' + \boldsymbol{r}, t' + t)\delta n(\boldsymbol{r}', t')\rangle \exp(-\mathrm{i}(\boldsymbol{k}\cdot\boldsymbol{r} - \omega t)) \,, \tag{32}$$

representing the Fourier transformation of the density–density correlation function $\langle \delta n(\boldsymbol{r}' + \boldsymbol{r}, t' + t)\delta n(\boldsymbol{r}', t')\rangle$, where $\langle \dots \rangle$ denotes the expectation value in the ground state. In homogeneous systems where the response is independent of the initial location $\boldsymbol{r}'$ and time t', the momentum dependence characterizes the spatial transport and the frequency dependence gives access to resonances, relaxation times and other spectral features.

The fluctuation–dissipation theorem establishes a direct relation between the dynamical structure factor $S(\boldsymbol{k}, \omega)$ and the response function χ which reads [105,139,140]

$$S(\boldsymbol{k}, \omega) = -\frac{2\hbar}{1 - \exp(-\hbar\omega/k_{\text{B}}T)} \,\text{Im}\,[\chi(\boldsymbol{k}, \omega)] = 2\hbar f_{\text{B}}(-\hbar\omega)\,\text{Im}\,[\chi(\boldsymbol{k}, \omega)]$$

$$\overset{\hbar \to 0}{=} -\frac{2k_{\text{B}}T}{\omega}\,\text{Im}[\chi(\boldsymbol{k}, \omega)] \,, \tag{33}$$

where the two first expressions apply for a fully quantum mechanical treatment and the last one for the classical limit. The factor $f_{\text{B}}(x) = [\exp(x/k_{\text{B}}T) - 1]^{-1}$ is the Bose function. Equivalently, the dynamical structure factor is related to the dielectric function ε through

$$S(\boldsymbol{k}, \omega) = \frac{2\hbar}{V(\boldsymbol{k})} f_{\text{B}}(-\hbar\omega)\,\text{Im}\left[\frac{1}{\varepsilon(\boldsymbol{k}, \omega)}\right] \overset{\hbar \to 0}{=} -\frac{2k_{\text{B}}T}{\omega V(\boldsymbol{k})}\,\text{Im}\left[\frac{1}{\varepsilon(\boldsymbol{k}, \omega)}\right] \,. \tag{34}$$

Note that both relations (33) and (34) are not directly reversible as the relation between χ and ε was. The structure function provides only the imaginary part of χ or $1/\varepsilon$. The full information is nonetheless contained also in the dynamical structure factor $S(\boldsymbol{k}, \omega)$ and may be regained by Kramers–Kronig relations.

Finally, there is one more quantity used to express response properties of a system, the *static structure factor* $S(\boldsymbol{k})$ which represents the instantaneous density–density correlation $\langle \delta n(\boldsymbol{r} + \boldsymbol{r}')\delta n(\boldsymbol{r}')\rangle$. It is thus connected to the spatial correlations between particles as contained in the pair distribution function $g(\boldsymbol{r})$ by Fourier transformation (see e.g. [77])

$$S(\boldsymbol{k}) = 1 + n\int \mathrm{d}^3 r\,(g(\boldsymbol{r}) - 1)\exp(-\mathrm{i}\boldsymbol{k}\cdot\boldsymbol{r}) \;. \tag{35}$$

The same symbol S is used for both, the static and the dynamic, structure factor. The actual meaning becomes apparent from the independent variables. This usage suggests a close correspondence and, in fact, the static structure factor is obtained from the time-dependent (dynamic) density–density correlation as the limit of instantaneous response $t \to 0$. This results in the relation

$$S(\boldsymbol{k}) = \frac{1}{n}\int_{-\infty}^{\infty}\frac{\mathrm{d}\omega}{2\pi}S(\boldsymbol{k},\omega) \;. \tag{36}$$

The unweighted integration over all frequencies is the obvious result from the "instantaneous" limit towards the static structure. It means physically that all dynamical responses are virtually present in the observed static correlations. There is, of course, also a simple relation between the static structure factor and the density–density response function χ or the dielectric function ε which can be easily established by combining Eq. (36) with the relations (33) or (34).

Each one of these four response functions discussed above has a natural relation to a particular observable of the system. The structure factors S have been developed in connection with scattering experiments on homogeneous systems. For example, the dynamical structure function is typically related to the neutron scattering analysis of atomic vibration spectra in solids [8] and applies for any scattering analysis with good energy resolution. It serves as a direct measure for the double differential cross section $\mathrm{d}^2\sigma/(\mathrm{d}\Omega\,\mathrm{d}E) \propto S(\boldsymbol{k},\omega)$ where the prefactor depends on the kinematics of the projectile and the scattering angle Ω is related to the transferred momentum $\hbar\boldsymbol{k}$ in the standard fashion. The response function χ or the dielectric function ε are naturally related to experiments with the optical (or electro-magnetic) response of a system. For example, the cross section for photo-absorption is $\sigma_{\mathrm{abs}} \propto \omega\,\mathrm{Im}\{\chi(k = \omega/c,\omega)\}$. The dielectric function is, by definition, a measure for the electro-magnetic properties of a material. Resonances show up as poles in χ or zeroes in ε. The broadening of resonances hints at the various damping mechanisms, as e.g. Landau damping or electron–electron scattering. Other transport properties as the electrical resistivity or thermal conductivity can also be related to these basic response functions [89]. A most important observable which is usually looked at before any more detailed analysis is the (Coulomb) interaction-energy E_{pot} which can be related to the static structure factor $S(\boldsymbol{k})$ through the exact relation $E_{\mathrm{pot}}/N = (1/16\pi^3)\int\mathrm{d}^3 k\,(e^2/\varepsilon_0 k^2)(S(k) - 1)$. The static structure function $\mathrm{d}\sigma/\mathrm{d}\Omega \propto S(\boldsymbol{k})$ is, furthermore, related to scattering without energy resolution, which amounts to integrating over all energies (= frequencies). Such a situation is typically met in X-ray scattering analysis of solids, or often deliberately arranged for correlation analysis of liquids by neutron scattering experiments [77].

The most important observable for our purposes is the stopping power $\mathrm{d}E/\mathrm{d}s$. The next subsection is devoted to establish and to discuss the relations between the stopping power and the

response functions in a regime where linear response applies, i.e. for cases of linear ion–target coupling where the ion exerts only a small perturbation on the electron system.

3.1.2. Stopping power by linear response

According to its definition (6) or (B.1), the stopping power is determined by the electric field $\mathscr{E}$ at the ion position which is caused by the charge density ϱ of the target. For an initially homogeneous system with $\varrho_0 = \varrho(t < t_0) = -en$ and $\mathscr{E}_0 = 0$ the relevant electric field is created by the charge density $\varrho_{ind}(\boldsymbol{r}, t) = \varrho(\boldsymbol{r}, t) - \varrho_0$ induced by the perturbing ion potential $\phi_p(\boldsymbol{r}, t) = \theta(t - t_0)Ze/4\pi\varepsilon_0|\boldsymbol{r} - \boldsymbol{v}t|$. Rewriting definition (6) in terms of the Fourier transformed ϱ_{ind} and ϕ_p, the stopping power on an ion with charge Ze and velocity $\boldsymbol{v}$ is

$$\frac{dE}{ds} = Ze\hat{\boldsymbol{v}} \cdot \mathscr{E}(\boldsymbol{r} = \boldsymbol{v}t)$$

$$= -\frac{i}{(2\pi)^4}\int d^3k \int d\omega\, \boldsymbol{k} \cdot \hat{\boldsymbol{v}} \varrho_{ind}(\boldsymbol{k}, \omega)\phi_p(-\boldsymbol{k})\exp(i(\boldsymbol{k} \cdot \boldsymbol{v} - \omega)t) . \tag{37}$$

This is still a general result for an initially homogeneous system. Assuming a linear ion–target coupling with sufficiently weak perturbation, we now employ the linear response relations (27) and (30). Identifying $\varrho_{ind} = -e\delta n$, $U_{ext} = -e\phi_p$ and $V(k) = e^2/\varepsilon_0 k^2$ we obtain the induced charge density as

$$\varrho_{ind}(\boldsymbol{k}, \omega) = \varepsilon_0 k^2 \phi_p(\boldsymbol{k}, \omega)\left[\frac{1}{\varepsilon(\boldsymbol{k}, \omega)} - 1\right] . \tag{38}$$

Inserting this relation together with the Fourier transformed $\phi_p = 2\pi Ze\delta(\omega - \boldsymbol{k} \cdot \boldsymbol{v})/\varepsilon_0 k^2$ into Eq. (37) and taking advantage of the symmetry $\varepsilon^*(\boldsymbol{k}, \omega) = \varepsilon(-\boldsymbol{k}, -\omega)$ finally yields

$$\frac{dE}{ds} = \frac{Z^2 e^2}{\varepsilon_0(2\pi)^3}\int d^3k\, \frac{\boldsymbol{k} \cdot \hat{\boldsymbol{v}}}{k^2}\, \text{Im}\left[\frac{1}{\varepsilon(\boldsymbol{k}, \boldsymbol{k} \cdot \boldsymbol{v})}\right] . \tag{39}$$

This is the basic expression for the stopping power in the regime of linear ion–target coupling $\langle\eta_p\rangle \ll 1$, applicable at any target conditions, i.e. any ξ, Θ, so far the corresponding dielectric function ε is available. Note that transient effects caused by switching on the ion–target interaction have been disregarded in deriving relation (39) by considering the limit $t_0 \to -\infty$. This limit is practically reached after a transient period of the order of the response time of the electron target ω_p^{-1} [160,161,199]. The induced electric field in the frame co-moving with the ion takes then a stationary value provided that the ion velocity ($\dot{v} \propto dE/ds$) varies slowly on the time scale for transient effects. This is usually ensured for a high projectile mass $M/m \gg 1$.

There is an alternative derivation of the stopping power (39) which is based on the concept of a scattering rate R. It illustrates a different aspect of linear response and provides an additional interpretation of stopping [3,6]. The scattering rate $R(\boldsymbol{k}, \omega(\boldsymbol{k}))$ depends on the change in momentum $\hbar\boldsymbol{k} = \boldsymbol{p}' - \boldsymbol{p}$ and energy $\hbar\omega(\boldsymbol{k}) = p'^2/2M - p^2/2M = ((\boldsymbol{p} + \hbar\boldsymbol{k})^2 - p^2)/2M = \hbar\boldsymbol{k} \cdot \boldsymbol{v} + \hbar^2 k^2/2M$ for an ion with charge Ze, mass M and velocity $\boldsymbol{v}$. It can be computed with Fermi's 'Golden Rule' and the

dynamical structure factor $S(\boldsymbol{k}, \omega)$ as the density of the elementary excitations of the target. This yields the scattering rate R (per time and k-space volume)

$$R(\boldsymbol{k}, \omega(\boldsymbol{k})) = \frac{1}{\hbar^2}|e\phi_p(\boldsymbol{k})|^2 S(\boldsymbol{k}, \omega(\boldsymbol{k})) = \frac{1}{\hbar^2}\left(\frac{Ze^2}{\varepsilon_0 k^2}\right)^2 \frac{2\hbar\varepsilon_0 k^2}{e^2} f_B(-\hbar\omega(\boldsymbol{k})) \operatorname{Im}\left[\frac{1}{\varepsilon(\boldsymbol{k}, \omega(\boldsymbol{k}))}\right], \tag{40}$$

where Eq. (34) was used to relate the dynamical structure factor to the dielectric function. The energy loss per time dE/dt is deduced from the scattering rate R as the average over all losses and gains of energy quanta $\hbar\omega$ where $\omega > 0$ represents a gain for the target and a loss for the projectile. The stopping power $dE/ds = 1/v\, dE/dt$ becomes then

$$\frac{dE}{ds} = -\frac{1}{v}\int\frac{d^3 k}{(2\pi)^3}\hbar\omega(\boldsymbol{k})R(\boldsymbol{k}, \omega(\boldsymbol{k})) = -\frac{Z^2 e^2}{\varepsilon_0 4\pi^3}\int d^3 k \frac{\omega(\boldsymbol{k})f_B(-\hbar\omega(\boldsymbol{k}))}{vk^2}\operatorname{Im}\left[\frac{1}{\varepsilon(\boldsymbol{k}, \omega(\boldsymbol{k}))}\right]. \tag{41}$$

Again we consider here the limit of heavy projectiles $(M \gg m)$ which allows to neglect the recoil effects, taking $\omega(\boldsymbol{k}) = \boldsymbol{k} \cdot \boldsymbol{v}$. Using the symmetries of $\varepsilon(\boldsymbol{k}, \omega)$ as well as the relation $f_B(x) + f_B(-x) = -1$ for the Bose function yields finally the stopping power in the form (39). The present procedure views the energy loss as an average over absorption and emission of energies $\hbar\omega$ by the projectile. This aspect provides also a simple way to describe the straggling, i.e. the deviation of the energy loss per path-length from its mean value. The relative straggling (as compared with dE/ds) is given by the second ω-moment of the scattering rate R [6].

The general dependencies on the basic projectile parameters, charge Z and velocity v, are the most important features. One sees immediately from Eq. (39) that the stopping power grows quadratically with Z, which is a trivial consequence from the linear response which depends linearly on the perturbation Z. The dependence on the velocity is more involved. We have to distinguish two regimes. For ion velocities v low compared to the mean electron velocity $\langle v_e \rangle$ the stopping power is linear in v

$$\frac{dE}{ds} = -\frac{Z^2 e^2 n}{\varepsilon_0(2\pi)^3 \omega_p} v \left[C(\xi, \Theta) + O(v^2)\right], \quad v \ll \langle v_e \rangle, \tag{42}$$

where the dimensionless friction coefficient $C(\xi, \Theta)$ depends on the target conditions and hence on the interparticle correlations. It can be obtained immediately from Eq. (39) as

$$C(\xi, \Theta) = \frac{4\pi\omega_p}{3n}\int_0^\infty dk\, k^2\left(\frac{\partial}{\partial\omega}\operatorname{Im}\left[\frac{1}{\varepsilon(k, \omega)}\right]\right)_{\omega=0}, \tag{43}$$

assuming $\varepsilon(\boldsymbol{k}, \omega) = \varepsilon(k, \omega)$ for an isotropic target. In the limit of large velocities, on the other hand, the stopping power goes like

$$\frac{dE}{ds} = -\frac{Z^2 e^4 n}{4\pi\varepsilon_0^2 m}\frac{1}{v^2}\left[\ln\left(\frac{2mv^2}{\hbar\omega_p}\right) + O(1/v^2)\right], \quad v \gg \langle v_e \rangle, \tag{44}$$

and depends on the target conditions only through the electron density n. The approach to the limit (44) for sufficiently high v follows directly from the f-sum-rule for the dynamical structure factor which is related to particle number conservation ([140], Section 2.2). Thus, only the energy loss at low velocities provides information about the correlations within the target.

We want to point out once again that the general relation (39) between stopping power and dielectric response applies to any kind of target, ideal and nonideal electron plasmas as well as targets beyond the present considerations like two component plasmas of different degrees of ionization and degeneracy or solids and atomic or molecular gases. In these cases also inelastic contributions from ionization and excitation of bound states are included in the linear response stopping power. It is only required that the ion target coupling is linear or, with some restrictions to be discussed below, semilinear. The crucial task is thus to derive the dielectric function for a given system, including properly all necessary correlations.

3.1.3. The RPA dielectric function for ideal targets

For ideal electron targets $\xi \ll 1$, the response functions $\chi(\mathbf{k}, \omega)$ and $\varepsilon(\mathbf{k}, \omega)$ are derived within the weak coupling limit of interparticle correlations, well-known as the random phase approximation (RPA). Starting point to derive the RPA density–density response function χ_R, denoted by the subscript R, is the *free* density–density response function χ_0. It is easy to evaluate for homogeneous systems and yields

$$\chi_0(\mathbf{k}, \omega) = -2 \int \frac{d^3 p}{(2\pi\hbar)^3} \frac{f_0(\mathbf{p} + \hbar\mathbf{k}) - f_0(\mathbf{p})}{\hbar\omega - \zeta(\mathbf{p} + \hbar\mathbf{k}) + \zeta(\mathbf{p}) + i0} , \tag{45}$$

where $f_0(\mathbf{p}) = 1/(\exp((\zeta(\mathbf{p}) - \mu)/k_B T) - 1)$ is the Fermi–Dirac distribution with chemical potential μ and the free electron dispersion $\zeta(\mathbf{p}) = \mathbf{p}^2/2m$. The free density–density response function χ_0 (45) is often called the Lindhard function [109]. The RPA density–density response function χ_R is computed from this free response and the two-body Coulomb interaction $V(\mathbf{k}) = e^2/\varepsilon_0 k^2$ by the RPA equation

$$\chi_R(\mathbf{k}, \omega) = \frac{\chi_0(\mathbf{k}, \omega)}{1 - V(\mathbf{k})\chi_0(\mathbf{k}, \omega)} . \tag{46}$$

The RPA dielectric function ε_R then follows from $\chi_R(\mathbf{k}, \omega)$ using relation (30) as

$$\varepsilon_R(\mathbf{k}, \omega) = 1 - V(\mathbf{k})\chi_0(\mathbf{k}, \omega) = 1 - \frac{e^2}{\varepsilon_0 k^2} \chi_0(\mathbf{k}, \omega) . \tag{47}$$

The RPA response functions χ_R (46) and ε_R (47) provide the dynamical response of an ideal electron target for any degree of degeneracy, for a cold electron gas in solids (using the jellium approximation) as well as for dilute, hot classical plasmas [7,64]. For the homogeneous and isotropic electron targets which we consider here the response functions χ_0 (45), χ_R (46) and ε_R (47) depend only on the absolute value of $\mathbf{k}$.

3.1.4. Dielectric functions for nonideal targets, LFC and LDA

The RPA equation (46) incorporates already the most important long range correlations from the Coulomb interactions. In particular, it gives a pertinent description of the response of the collective plasmon mode. There remain, however, several deficiencies from neglecting higher correlations, as, e.g., exchange in the quantum regime, or short range correlations accounting for close two-electron collisions. Density functional methods aim to cure these deficiencies by developing an effective interaction which incorporates correlations beyond mean field while maintaining

the simple structure of the mean field equations, here the RPA equations (46). Quite general theorems guarantee the existence of such effective interactions [84,102,151], but actually applicable functionals require a few more approximations. Subsequently, there emerges a variety of formulations towards the desired goal of an optimal compromise between theoretical soundness and practicability. There is a widespread literature on this topic and we cannot dwell in all the details of the various approaches. We aim here merely at a short overview of two widely used schemes, the technique of the local field corrections (LFC) and the Kohn–Sham equations with energy-density functionals derived in local density approximation (LDA). We are going to discuss here the LFC while a discussion of the LDA will be presented in connection with applications to the nonlinear coupling regime in Section 3.3.5.

The local field correction (LFC) is defined as a correction to an underlying RPA description. Starting point is the RPA equation (46) for the RPA response function χ_R. The exact response function χ will differ and contain, of course, more information about higher correlations. But the RPA response has anticipated already a great deal of the most crucial long range correlations. It is thus useful to define the extra correlations with reference to RPA. This is done by

$$\chi(\boldsymbol{k}, \omega) = \frac{\chi_0(\boldsymbol{k}, \omega)}{1 - V(\boldsymbol{k})(1 - G(\boldsymbol{k}, \omega))\chi_0(\boldsymbol{k}, \omega)} , \tag{48}$$

which defines the correlations in terms of a modified residual interaction, $V \rightarrow V(1 - G)$, to be used in the RPA equations. This modification is summarized in the function $G(\boldsymbol{k}, \omega)$ which is called the *local field correction*. By relation (30) the modified dielectric function takes the form

$$\varepsilon(\boldsymbol{k}, \omega) = 1 - \frac{V(\boldsymbol{k})\chi_0(\boldsymbol{k}, \omega)}{1 + V(\boldsymbol{k})G(\boldsymbol{k}, \omega)\chi_0(\boldsymbol{k}, \omega)} . \tag{49}$$

The RPA expressions (47) and (46) are recovered for vanishing LFC $G(\boldsymbol{k}, \omega) \rightarrow 0$.

The form of definition (48) suggests that deeper correlation effects can be treated in terms of an effective interaction for RPA calculations and it hints the direction for the systematic construction of approximations. The two most widely used of the various possibilities will be discussed in the following two subsections. Note that the LFC depends generally on momentum and frequency. This means that the so defined effective interaction $V(\boldsymbol{k})(1 - G(\boldsymbol{k}, \omega))$ embodies retardation. The spectral structure of $G(\boldsymbol{k}, \omega)$ reflects the dynamics of the higher many-body correlations from which one can hope that these are faster than the dominant modes described in RPA (usually the plasmon mode). This suggests already a first step of approximation, the static LFC $G(\boldsymbol{k})$ where the ω dependence is neglected. Rephrasing the relation (48) in terms of the structure functions suggests that a static LFC $G(\boldsymbol{k})$ should be one-to-one related to the static structure function $S(\boldsymbol{k})$ and thus to the pair distribution function $g(\boldsymbol{r})$. The both approximation schemes discussed below try to establish such a relation from different starting points.

3.1.5. The STLS approach to LFC

One line of development has been initiated by Singwi–Tosi–Land–Sjölander in [165] (STLS approach). It starts from incorporating the two-particle density in the derivation of the response functions χ_0 and χ which are based solely on the one-particle density in the usual RPA approach.

This establishes a relation between the (static) pair distribution function $g(r)$ and the static LFC $G(k)$ given by

$$G(k) = -\frac{1}{n} \int \frac{d^3q}{(2\pi)^3} \frac{q \cdot k}{q^2} [S(k-q) - 1] , \qquad (50)$$

where the static structure factor $S(k)$ is uniquely related to $g(r)$ by Eq. (35). The STLS approach was first derived in a classical environment. It has been generalized to quantum systems in [158,159].

To give an idea how relation (50) is derived, we sketch here quickly the simpler case of a purely classical system. Starting point is the parametrization of the two-particle phase-space density $f^{(2)}$ in terms of the equilibrium correlation function $g(r)$ as

$$f^{(2)}(r_1, p_1; r_2, p_2; t) = f(r_1, p_1; t) f(r_2, p_2; t) g(r_1 - r_2) . \qquad (51)$$

Upon integration over the momenta p_1, p_2 this is an exact relation for the time-independent case. It is an approximation for a truly dynamical situation based on the assumption that the static correlations are dominated by spatial correlations and that they are not so much affected by the oscillations of the mean field. The further steps are straightforward and tedious: The ansatz (51) is inserted into the lowest of the BBGKY equations determining $\partial_t f(r_1, p_1; t)$, see e.g. [14]. The one-particle phase space distributions $f(r, p; t)$ in that equation thus emerging are expanded into a stationary part plus a small dynamical perturbation as $f = f_0 + \delta f$, and linearized in terms of the δf. Rephrasing that equation in terms of the response functions χ_0 and χ yields a generalized RPA equation of the type (48) from which one can read off the LFC by comparison resulting in relation (50) after expressing the pair distribution function g by its equivalent static structure function S.

Eq. (50) deduces a static LFC from given static structure function. The LFC, on the other hand, determines a structure function from the generalized response equation (48). This closes the circle and suggests a selfconsistent scheme as follows:

(1) Start from a given static structure function $S(k)$ and use Eq. (50) to compute the corresponding LFC $G(k)$.

(2) The now given $G(k)$ allows to compute the response function $\chi(k, \omega)$ using Eq. (48).

(3) The response function defines the dynamic structure function $S(k, \omega)$ according to Eq. (33).

(4) Frequency integration in relation (36) delivers a new static structure function $S(k)$ from which one continues from step 1 until sufficient convergence is achieved.

This STLS scheme is conceptually obvious and technically still fairly simple. Thus it has been widely used in several applications where a correlated electron plasma plays a role. And it has been developed further to finite temperatures, to a fully quantum mechanical treatment, and to a truly dynamical local field correction [158,159]. There arise, however, the typical problems when constructing approaches to correlations: the emerging response and correlation functions violate basic consistency conditions. The worst problem in the STLS approaches is probably that the spatial correlation function $g(r)$ ceases to be positive semi-definite. i.e. one finds occasionally $g < 0$ at small distances. This does not seem to cause problems for global observables where the STLS approach has much success. But it is a hindrance for studying more detailed observables.

The STLS scheme can be simplified by a sum rule approach. The dielectric response is dominated by the free particle response, on one hand, and by the plasmon response, on the other. A simple and reliable approximation can be obtained by constructing the static structure

function from the free particle structure function and the contribution of the plasmon pole. Such an approach reduces the selfconsistent STLS problem to purely static coupled equations, thus avoiding the cumbersome frequency structure in the full STLS. The model and some applications to the two- and three-dimensional electron gas have been discussed in [63] and references cited therein. It has been applied to compute the stopping power for a two-dimensional electron gas in [181]. It is found that the LFC enhance the stopping power for small ion velocities $v < v_F$ where v_F is the Fermi velocity of the electrons. For larger velocities, the stopping power converges rapidly towards the result from the simple dielectric theory, that is, the high velocity result (44).

3.1.6. LFCs by using information from HNC calculations

The STLS approach as reviewed in the previous Section 3.1.5 constitutes a simple and selfconsistent scheme to compute correlations effects which often provides pertinent results. Its correlation function, however, violates basic consistency conditions, e.g. the positivity of $g(r)$. Other approaches spend more effort to achieve compatibility with these conditions. A most widely used scheme amongst these is the hypernetted-chain (HNC) approximation. It has also been much applied to problems in plasma physics, for a review in the context with plasma applications up to computing the stopping power see [90]. The HNC scheme allows to compute the static pair correlation function $g(r)$ for a plasma and subsequently the internal energy or further thermodynamic properties. It is desirable to incorporate this detailed and reliable information into the computation of the dielectric response and its related observables. The connection is established by choosing a *static* LFC $G(k)$ such that the LFC corrected RPA equation (48) together with the relations (33) and (36) yields the static structure function $S(k)$ as it is prescribed from HNC, i.e.

$$S^{HNC}(\mathbf{k}) \overset{!}{=} S(\mathbf{k}) = \frac{2\hbar}{n} \int d\omega f_B(-\hbar\omega) \mathrm{Im}\left[\frac{\chi_0(\mathbf{k}, \omega)}{1 - V(\mathbf{k})(1 - G(\mathbf{k}))\chi_0(\mathbf{k}, \omega)}\right].$$

This relation simplifies dramatically in the classical limit $\hbar \to 0$ and reduces to [88,90]

$$G(\mathbf{k}) = 1 - k^2 \lambda_D^2 \left(\frac{1}{S^{HNC}(\mathbf{k})} - 1\right), \tag{52}$$

where λ_D is the Debye length. The choice (52) then guarantees the recovery of the static properties of the HNC approach through the LFC corrected dielectric formulation, summarized in Eq. (49). But now the dielectric formulation can be applied for truly dynamical processes as well. This way one has achieved a dynamical extrapolation of the static HNC correlations. In practical implementations, it is advantageous to employ a properly parametrized form for the static structure function $S(\mathbf{k})$ or the related static LFC $G(\mathbf{k})$ as obtained from HNC, for an example see Section 3.2.1 of [90] and work cited therein. A careful shaping of the ansatz allows to meet most of the important consistency condition for the pair distribution function, i.e. the compressibility sum rule, the positivity condition $g > 0$, and the short wavelength limit $\lim_{\mathbf{k} \to \infty} G(\mathbf{k}) = 1 - g(0)$. Spin degrees-of-freedom are also incorporated and the corresponding spin-susceptibility sum rule is met by construction.

There exist also extensive HNC calculations for two-component plasmas consisting of ions and electrons. The inherent instabilities occurring through the attractive ion–electron interaction [112]

can be circumvented by disentangling the HNC scheme into subsequent steps, solving HNC first for the electrons, then for ions using the electron-screened potential, and then adding carefully the effect of the ion–electron interaction [88,90]. This delivers at the end a 2×2 matrix for the static structure function, and subsequently for the static LFC by a relation similar to Eq. (52). Several further observables can be deduced in the standard fashion using the LFC corrected dielectric theory, see e.g. Section 3.1.1 of [90], once the LFC are given. In particular, one can compute the stopping power using the relation (39).

The LFC as defined in Eq. (48) are in general dynamical quantities depending also on the frequency ω. The approximation by static LFC discussed above works very well for many purposes. But there are also drawbacks, e.g. in the description of the detailed line broadening of the plasmon peak. A dynamical LFC is thus desirable. Such an extended approach may still be deduced from static HNC calculations by considering limiting cases and interpolation. Guided by dynamical studies of [175], Ichimaru et al. propose an interpolation as [88,90]

$$G(\boldsymbol{k}, \omega) = \frac{G(\boldsymbol{k}) - \mathrm{i}\omega\tau(\boldsymbol{k})I(\boldsymbol{k})}{1 - \mathrm{i}\omega\tau(\boldsymbol{k})} \ , \tag{53}$$

where $\tau(\boldsymbol{k})$ is the typical relaxation in mode $\boldsymbol{k}$ and the structure component $I(\boldsymbol{k}) = \lim_{\omega \to \infty} G(\boldsymbol{k}, \omega)$. It can be obtained from static HNC calculations as a higher weighted average over the static structure function

$$I(\boldsymbol{k}) = \frac{1}{n} \int \frac{\mathrm{d}^3 q}{(2\pi)^3} \left[\frac{\boldsymbol{k} \cdot \boldsymbol{q}}{q^2} + \frac{\boldsymbol{k} \cdot (\boldsymbol{q} - \boldsymbol{k})}{|\boldsymbol{k} - \boldsymbol{q}|^2} \right] \frac{\boldsymbol{k} \cdot \boldsymbol{q}}{q^2} [1 - S(\boldsymbol{k} - \boldsymbol{q})] \ .$$

and it is related to the viscosity [175]. This dynamical LFC approach has been extensively studied by Ichimaru and collaborators with respect to all sorts of observables. A detailed discussion of results using these static and dynamical LFC with HNC input is found in [89–90,123,173,189].

Existing treatments based on HNC and quantum HNC [93], on the STLS (Section 3.1.5) approach and extended STLS schemes [158,159], on informations from Greens-function-Monte–Carlo methods [176] or on diffusion Monte–Carlo results [125,162] are able to provide LFCs at any target conditions Θ, ξ. Hence using LFCs to obtain the modified dielectric function (49) and subsequently the stopping power by Eq. (39) allows to study ion stopping in all kind of nonideal, strongly correlated targets, provided, of course, that the ion–target coupling is linear or at least semilinear. Its domain of application is thus the parameter space with $\xi \gtrsim 1$ and $\langle \eta_{\mathrm{p}} \rangle \lesssim 1$, i.e. the regime of low projectile charge states Z or high velocities as can be seen immediately by inspecting definitions (20) and (21). The LFCs generally increase the stopping and they are particularly important at low ion velocity [153,182] while for high ion velocities the simple RPA dielectric description, see e.g. [115], becomes sufficient again. The static LFC includes already most of the corrections and the dynamical LFC adds a bit on top.

3.1.7. Dielectric function in relaxation-time approximation

Another possibility is to include correlations in terms of instantaneous (quasi)particle collisions. A particular simple scheme for that is provided by the relaxation-time approximation as suggested by Mermin [121]. The resulting dielectric function for a given electron–electron collision frequency

v takes the form

$$\varepsilon(\boldsymbol{k}, \omega) = 1 + \frac{(\omega + i\nu)(\varepsilon_R(\boldsymbol{k}, \omega + i\nu) - 1)}{\omega + i\nu(\varepsilon_R(\boldsymbol{k}, \omega + i\nu) - 1)/(\varepsilon_R(\boldsymbol{k}, 0) - 1)}, \tag{54}$$

expressed in terms of the RPA dielectric function ε_R (47). The collision frequency ν is used as a model parameter. In some investigations on stopping of ions in carbon and silicon the collision frequency ν was determined by fitting $-\operatorname{Im}[1/\varepsilon(\boldsymbol{k} = 0, \omega)]$ to experimental optical energy loss functions [1,10,12,133,134]. Treating the collision frequency as a free parameter, the modified dielectric function (54) allows useful qualitative estimates of the influence of electron–electron collisions on the stopping power. The predicted effect is a shorter life time and smaller mean free path of the plasmons resulting in considerable modifications of the wake field behind the passing ion [11]. This is of particular importance for vicinity effects on the energy loss of multi-ion arrangements [12,195,198]. For the stopping of a single ion, the broadening of the plasmon peak with increasing ν shifts the threshold for the energy loss by plasmon excitation towards lower projectile velocities. It is now possible that ions with low velocities can also excite plasmons which increases the stopping power at low ν compared to the RPA result [10]. The stopping remains almost unchanged for high velocities which are above the threshold for plasmon excitations (at $\nu = 0$). This is in agreement with the common high velocity limit (44). Recently, relaxation rates ν have been deduced from MD-simulations for classical targets [168]. These confirm the kinetic behavior $\nu \propto \omega_p \Gamma^{3/2}$ (rate of Coulomb scattering events with scattering angles $> 90°$) in the weak coupling regime, but show an anti-kinetic behavior $\nu \propto \omega_p \Gamma^{-1.5}$ for nonideal systems with $\Gamma > 1$.

3.1.8. Perturbative corrections to the linear response

The stopping power (39) as obtained from the linear response formalism represents the first order in a perturbation expansion with respect to the external perturbation ϕ_p. This suggests that improvements in the description of stopping can be achieved by taking into account higher orders in the perturbation series. The second order terms are called the Barkas correction [17]. They are quadratic in ϕ_p and hence their contribution to stopping is $\propto Z^3$. More precisely, the Barkas correction gives a contribution of the order $Z/(\langle v_r \rangle')^3$ relative to the leading Z^2 term of the linear response theory. Thus it is a small correction in the linear, and to some extent in the semilinear, regime. But the perturbation series diverges as soon as one reaches the nonlinear regime. The approach shares the general features of a perturbation series: it is designed to enhance the accuracy of the description within a regime inside the convergence radius of the expansion, i.e. the regime of weak coupling. A general discussion of this line of development is found in [9,51,141]. Investigations on the Barkas contribution in a classical electron target ($\hbar \to 0$) and for semilinear ion–target coupling are presented in [37,135,154].

3.2. Semilinear ion–target coupling

In the semilinear coupling regime, the perturbation caused by the ion is just beyond weak. But there arises a spatial distinction such that the perturbation remains truly weak in the largest part of the ion–target interaction region – as ensured by definition (22). Only electrons in a very small volume ($\propto r_c^3 \ll \lambda^3$) near the ion explore a strong perturbation. This suggests an approach which

relies on linear response and adds corrections from the small region of nonlinear effects. Such a procedure will be much less expensive than a fully nonlinear description of stopping, and it applies to a rather large area of projectile and target parameters covered by the semilinear regime, see Fig. 2. This justifies our notion of a semilinear regime and a particular treatment of stopping in this regime. These approaches are based essentially on the complementarity of dielectric linear response and binary electron–ion collision. The linear response accounts correctly for all the dynamical polarization effects in the target as long as the coupling is linear, i.e. in the dominant fraction of the interaction zone. Binary collisions in the inner interaction region are governed by the ion–electron interaction at arbitrary strengths η_p while being insensitive to the dynamical effects. Some approximation schemes to combine both aspects are presented in the next subsections. First, however, we will discuss the treatment of binary collisions in general.

3.2.1. Stopping by binary collisions

For negligible interaction between the electrons in an ideal plasma ($\xi \ll 1$), the stopping can be described entirely by independent binary ion–electron collisions. This holds for arbitrary strengths of the ion–electron interaction. This completely kinetic approach starts by describing the system through the momentum distribution $\tilde{f}(\boldsymbol{P})$ of the ion and the distribution $f(\boldsymbol{p})$ of the electrons. The time evolution of the ion distribution is determined from scattering events $(\boldsymbol{P},\boldsymbol{p}) \leftrightarrow (\boldsymbol{P}',\boldsymbol{p}')$ of the ion with electrons in terms of a collision integral I_{ie} as $\partial_t \tilde{f}(\boldsymbol{P}) = I_{ie}$. Here, we use the quantum version of a Boltzmann collision integral for ion–electron collisions which includes Pauli blocking factors for the final electron states and allows to treat all degrees of degeneracy of the electron target. The force $\boldsymbol{F}$ on the ion, i.e. the time derivative of its momentum, can be expressed now as the integral (see also the definition (8) of stopping)

$$
\boldsymbol{F} = \frac{\mathrm{d}}{\mathrm{d}t}\langle\boldsymbol{P}\rangle = V \int \frac{\mathrm{d}^3 P}{(2\pi\hbar)^3} \boldsymbol{P} \frac{\partial\tilde{f}(\boldsymbol{P})}{\partial t} = V \int \frac{\mathrm{d}^3 P}{(2\pi\hbar)^3} \boldsymbol{P} I_{ie}
$$

$$
= \frac{2V}{\mu^2} \int \frac{\mathrm{d}^3 P\, \mathrm{d}^3 P'\, \mathrm{d}^3 p\, \mathrm{d}^3 p'}{(2\pi\hbar)^6} \boldsymbol{P}\, w(\boldsymbol{P},\boldsymbol{p};\boldsymbol{P}',\boldsymbol{p}') \left[\tilde{f}(\boldsymbol{P}')f(\boldsymbol{p}')(1-f(\boldsymbol{p})) - \tilde{f}(\boldsymbol{P})f(\boldsymbol{p})(1-f(\boldsymbol{p}')) \right], \tag{55}
$$

where $\mu = mM/(m+M)$ is the reduced mass, V a spatial volume and

$$
w(\boldsymbol{P},\boldsymbol{p};\boldsymbol{P}',\boldsymbol{p}') = \sigma(\boldsymbol{P},\boldsymbol{p};\boldsymbol{P}',\boldsymbol{p}')\delta^3(\boldsymbol{P}+\boldsymbol{p}-\boldsymbol{P}'-\boldsymbol{p}')\delta(\tilde{\zeta}(\boldsymbol{P})+\zeta(\boldsymbol{p})-\tilde{\zeta}(\boldsymbol{P}')-\zeta(\boldsymbol{p}'))
$$

with the energies $\tilde{\zeta}(\boldsymbol{P}) = P^2/2M$ of the ion and $\zeta(\boldsymbol{p}) = p^2/2m$ of the electrons and the cross section σ for the collisions $(\boldsymbol{P},\boldsymbol{p}) \leftrightarrow (\boldsymbol{P}',\boldsymbol{p}')$. For the projectile ion with a given velocity $\boldsymbol{v}$, the corresponding distribution is $\tilde{f}(\boldsymbol{P}) = [(2\pi\hbar)^3/V]\delta^3(\boldsymbol{P}-M\boldsymbol{v})$. This allows to integrate over two momenta. Assuming a cross section with the symmetry $\sigma(\boldsymbol{P},\boldsymbol{p};\boldsymbol{P}',\boldsymbol{p}') = \sigma(\boldsymbol{P}',\boldsymbol{p}';\boldsymbol{P},\boldsymbol{p})$ and substituting $(\boldsymbol{p}'-\boldsymbol{p}) \to \boldsymbol{q}$, the stopping power $\mathrm{d}E/\mathrm{d}s = \hat{\boldsymbol{v}}\cdot\boldsymbol{F}$ becomes

$$
\frac{\mathrm{d}E}{\mathrm{d}s} = \frac{2}{\mu^2} \int \frac{\mathrm{d}^3 p\, \mathrm{d}^3 q}{(2\pi\hbar)^3} \hat{\boldsymbol{v}}\cdot\boldsymbol{q}\ \sigma(M\boldsymbol{v},\boldsymbol{p};M\boldsymbol{v}+\boldsymbol{q},\boldsymbol{p}-\boldsymbol{q})\delta(\tilde{\zeta}(M\boldsymbol{v})+\zeta(\boldsymbol{p})-\tilde{\zeta}(M\boldsymbol{v}+\boldsymbol{q})-\zeta(\boldsymbol{p}-\boldsymbol{q}))
$$

$$
\times f(\boldsymbol{p})(1-f(\boldsymbol{p}-\boldsymbol{q})). \tag{56}
$$

Alternatively to this expression in terms of the transferred momentum q, one can obtain a more common representation by a transformation to center of mass momentum $K = Mv + p = K'$ and relative momenta $p_r = p - (\mu/M)K = (\mu/m)p - \mu v$, and $p'_r = p_r - q$. The cross section σ is usually independent of the center of mass motion, that is, $\sigma = \sigma(p_r; p'_r)$. This yields

$$
\frac{dE}{ds} = \frac{2}{\mu^2}\left(\frac{m}{\mu}\right)^3 \int \frac{d^3p_r\, d^3p'_r}{(2\pi\hbar)^3} \delta\left(\frac{p_r^2}{2\mu} - \frac{p'^2_r}{2\mu}\right) v \cdot [p_r - p'_r]\sigma(p_r; p'_r)\left[f\left(\left(1 + \frac{m}{M}\right)p_r + mv\right)\right.
$$
$$
\left. - f\left(\left(1 + \frac{m}{M}\right)p_r + mv\right)f\left(p'_r + \frac{m}{M}p_r + mv\right)\right] . \tag{57}
$$

The cases of heavy ions and spherical scattering potentials allow further simplifications. For a heavy ion, the reduced mass becomes $\mu \approx m$ or $m/M \to 0$ and the quadratic term $f((1 + (m/M))p_r + mv)f(p'_r + (m/M)p_r + mv)$ connected with Pauli-blocking cancels out for differential cross sections $\sigma(p_r; p'_r)$ which are invariant under an exchange of p_r and p'_r. There remains

$$
\frac{dE}{ds} = 2\int \frac{d^3p_r}{(2\pi\hbar)^3} f(p_r + mv)\frac{p_r^2}{m}\int d\Omega'\, \hat{v} \cdot [\hat{p}_r - \hat{p}'_r]\sigma(p_r; p_r\hat{p}'_r) . \tag{58}
$$

It is worth to remark, that the stopping power (58) obtained under these conditions within the present kinetic-probabilistic description agrees completely with a rigorous, fully quantum mechanical treatment developed in [25,156]. There one starts with the definition of the energy transfer (B.1) and evaluates it in the limit $t \to \infty$ for non-interacting electrons, taking as initial state an ensemble of plane waves for the single electron states with occupation numbers according to the distribution f.

For spherical symmetric scattering potentials, where $\sigma(p_r; p'_r) = \sigma(p_r, \vartheta)$ the stopping power appears finally in the very compact form

$$
\frac{dE}{ds} = 2\int \frac{d^3p_r}{(2\pi\hbar)^3} f(p_r + mv)\frac{p_r}{m} \hat{v} \cdot p_r\, \sigma_{tr}(p_r) . \tag{59}
$$

Here the transport cross section $\sigma_{tr}(p_r) = 2\pi\int_{-1}^{1} d\cos(\vartheta)[1 - \cos(\vartheta)]\sigma(p_r, \vartheta)$ has been introduced after integrating over the scattering angle ϑ, with $\cos(\vartheta) = (p_r \cdot p'_r)/p_r^2$. Usually, one is interested in ion stopping in an electron plasma in thermal equilibrium and the electron distribution f is the Fermi–Dirac distribution f_0 for free electrons. As a remarkable feature, the final results for the stopping power Eqs. (58) and (59) depend linearly on the electron distribution $f = f_0$ for any degree of degeneracy Θ. That is, the influence of the quadratic Pauli-blocking term in Eq. (57), $f_0((1 + (m/M))p_r + mv)f_0(p'_r + (m/M)p_r + mv)$, becomes negligible in the limit of small mass ratios $m/M \to 0$. In the general case of arbitrary m/M this Pauli-blocking term becomes unimportant only in the high temperature limit $\Theta \gg 1$, when f_0 merges into a Maxwell distribution and this quadratic term can be neglected. This case of arbitrary mass ratios and high temperatures $\Theta \gg 1$ is commonly used as starting point for the energy loss in terms of binary collisions [53,164,60,131]. There, one has just to retain the mass factors of Eq. (57) to obtain expressions analogous to Eqs. (58) and (59) with $f(p_r + mv)/m$ replaced by $(m/\mu)^3 f((1 + m/M)p_r + mv)/\mu$.

For spherical potentials simple and compact expressions in terms of the transport cross sections can be easily derived in the low and high projectile velocity range, respectively. At low velocities, an

expansion with respect to v of the shifted electron distribution in the stopping power (59) yields

$$\frac{\mathrm{d}E}{\mathrm{d}s} = v\frac{1}{3\pi^2 m\hbar^3}\int_0^\infty \mathrm{d}p\, p^5 \frac{\partial f_0}{\partial\zeta(p)}(p)\,\sigma_{\mathrm{tr}}(p), \quad v \ll \langle v_e\rangle\ . \tag{60}$$

For high velocities an even simpler expression is obtained by substituting $\mathbf{p}_r \to (\mathbf{p} - m\mathbf{v})$ and approximating $p_r = |\mathbf{p}_r| \approx mv$. This leads to

$$\frac{\mathrm{d}E}{\mathrm{d}s} = -mnv^2\sigma_{\mathrm{tr}}(mv), \quad v \gg \langle v_e\rangle\ , \tag{61}$$

where the density n emerges through $2\int\mathrm{d}^3p f_0(p) = n(2\pi\hbar)^3$.

To express the stopping power in terms of the electron distribution and an effective electron–ion cross section goes in fact beyond a mere binary collision approximation and is employed in various different regimes, see e.g. Section 3.3.6 for applications to the case of nonlinear electron–ion coupling and highly degenerate target systems. The key issue is then to find an appropriate effective ion–electron potential and to compute the related effective cross section. A main ingredient to that are collective effects of the electron cloud like dynamical screening and plasma waves. These effects are, of course, best under control in the linear response regime. We thus regard, as a first exercise and test, the cross section for the case of linear ion–target coupling. The required effective ion–electron potential ϕ_{ei} is then for ideal plasmas ($\xi \ll 1$) simply provided by the linear response of the medium in terms of the RPA dielectric function with $\phi_{\mathrm{ei}}(k,\omega) = \phi_{\mathrm{p}}(k)/\varepsilon_{\mathrm{R}}(k,\omega) = Ze/[\varepsilon_0 k^2\varepsilon_{\mathrm{R}}(k,\omega)]$, see Eq. (28). Because we deal with linear coupling $\langle\eta_{\mathrm{p}}\rangle \ll 1$, the cross section σ can be evaluated in first order Born approximation, yielding

$$\sigma(|\hbar\mathbf{k}|) = \frac{\mu^2}{4\pi^2\hbar^4}|e\phi_{\mathrm{ei}}(k,\omega(\mathbf{k}))|^2 = \frac{\mu^2}{4\pi^2\hbar^4}\frac{Z^2 e^4}{\varepsilon_0^2 k^4|\varepsilon_{\mathrm{R}}(k,\omega(\mathbf{k}))|^2}\ , \tag{62}$$

for a momentum transfer $\hbar\mathbf{k} = \mathbf{q}$ and the related energy transfer $\hbar\omega(\mathbf{k}) = \tilde\zeta(M\mathbf{v}) - \tilde\zeta(M\mathbf{v} + \hbar\mathbf{k}) = \zeta(\mathbf{p} - \hbar\mathbf{k}) - \zeta(\mathbf{p})$. The cross section in first order Born approximation depends only on the transferred momentum $\mathbf{q}$ and it is thus favourable to insert it into Eq. (56). Rewriting the product of Fermi–Dirac distributions as $f_0(\mathbf{p})(1 - f_0(\mathbf{p} - \hbar\mathbf{k})) = -[f_0(\mathbf{p}) - f_0(\mathbf{p} - \hbar\mathbf{k})]f_{\mathrm{B}}(\zeta(\mathbf{p}) - \zeta(\mathbf{p} - \hbar\mathbf{k}))$ by using the Bose distribution $f_{\mathrm{B}}(x) = [\exp(x/k_{\mathrm{B}}T) - 1]^{-1}$ yields

$$\frac{\mathrm{d}E}{\mathrm{d}s} = -\frac{Z^2 e^4}{4\pi^2\varepsilon_0^2}2\int\frac{\mathrm{d}^3p}{(2\pi\hbar)^3}\int\mathrm{d}^3k\,\delta(\hbar\omega(\mathbf{k}) + \zeta(\mathbf{p}) - \zeta(\mathbf{p} - \hbar\mathbf{k}))$$

$$\times f_{\mathrm{B}}(-\hbar\omega(\mathbf{k}))\,\hat{\mathbf{v}}\cdot\mathbf{k}\frac{[f_0(\mathbf{p}) - f_0(\mathbf{p} - \hbar\mathbf{k}]}{k^4|\varepsilon_{\mathrm{R}}(k,\omega(\mathbf{k}))|^2} = -\frac{Z^2 e^2}{4\pi^3\varepsilon_0}\int\mathrm{d}^3k\,\hat{\mathbf{v}}\cdot\mathbf{k}f_{\mathrm{B}}(-\hbar\omega(\mathbf{k}))\frac{\mathrm{Im}[\varepsilon_{\mathrm{R}}(k,\omega(\mathbf{k}))]}{k^2|\varepsilon_{\mathrm{R}}(k,\omega(\mathbf{k}))|^2}\ . \tag{63}$$

In the last step, the imaginary part of the RPA dielectric function (47)

$$\mathrm{Im}[\varepsilon_{\mathrm{R}}(k,\omega)] = 2\pi\frac{e^2}{\varepsilon_0 k^2}\int\frac{\mathrm{d}^3p}{(2\pi\hbar)^3}\delta(\hbar\omega + \zeta(\mathbf{p}) - \zeta(\mathbf{p} - \hbar\mathbf{k}))[f_0(\mathbf{p}) - f_0(\mathbf{p} - \hbar\mathbf{k})] \tag{64}$$

was introduced. It is to be remarked, that for the derivation of the stopping power in the present form of Eq. (63) the assumption of a target in thermal equilibrium with $f(\boldsymbol{p}) = f_0(\boldsymbol{p})$ is essential. The mass ratio between projectile and target particles may, however, be arbitrary. In the limit of heavy projectiles, $m/M \to 0$, projectile recoil can be neglected and yields $\hbar\omega(\boldsymbol{k}) = \tilde{\zeta}(M\boldsymbol{v}) - \tilde{\zeta}(M\boldsymbol{v} + \hbar\boldsymbol{k}) \approx -\hbar\boldsymbol{k}\cdot\boldsymbol{v}$. This allows to exploit the symmetry of the dielectric function $\varepsilon_{\mathrm{R}}(k, \omega) = \varepsilon_{\mathrm{R}}^*(k, -\omega)$ and the relation $f_{\mathrm{B}}(x) + f_{\mathrm{B}}(-x) = -1$, to obtain in this limit the stopping power in the form of Eq. (39) for $\varepsilon = \varepsilon_{\mathrm{R}}$, now called Born-RPA stopping power [115]. Thus the linear response stopping power (39) in an ideal target can alternatively be interpreted as result of binary ion–electron encounters in the linear coupling regime and with the effective interaction $e\phi_{\mathrm{ei}}(k, \omega) = Ze^2/\varepsilon_0 k^2\varepsilon_{\mathrm{R}}(k, \omega)$ containing the electron screening from linear response. This agreement is of course not unexpected as binary collisions and linear response are treated on the same level of approximation, that is in first order of the perturbation.

The binary collision approach Eqs. (55)–(59) applies a priori to any strength of the ion–electron interaction, i.e. for any $\langle\eta_{\mathrm{p}}\rangle$, provided that the full many-body dynamics can be mapped into an effective interaction. This should be feasible at least for situations where the electron–electron coupling is small compared to the ion–electron coupling at small distances as it will be the case for nonlinear coupling, $\langle\eta_{\mathrm{p}}\rangle \gg 1$, in an ideal plasma, $\xi < 1$, with weak electron–electron correlations. However, one has yet to determine this effective interaction which includes the dynamical and nonlinear response of the medium, for instance, by solving the ladder T-matrix equation with a fully dynamically screened interaction. Generally applicable tools for this task are not available at present, and we have to consider approximations. Static effective interactions are sufficient at low ion velocities where the strongest nonlinear effects are expected anyway. The well developed techniques of density functional theory can be employed in that limit, as will be outlined in Section 3.3.5. A widely used, simpler alternative is to parameterize the screened Coulomb potentials in terms of Yukawa functions. This concept allows also to include in a phenomenological way dynamical effects by using velocity dependent screening lengths. Surely, such heuristic treatments can be justified only a posteriori in truly nonlinear and dynamical situations, but they provide a very useful tool to supplement the linear response description by small nonlinear contributions in the more relaxed case of semilinear coupling. The resulting corrected linear response treatments are well suited to get fair approximations of the energy loss at semilinear coupling. This will be discussed further in the next subsections. In any case, of course, all approximations for the semilinear regime and extensions into the nonlinear one which are based on some appropriate assumptions and models for an effective potential need to be checked by fully dynamical many-body treatments as e.g. the simulation techniques presented in Section 3.3.

3.2.2. Corrections of linear response stopping using cutoffs

As shown above, the linear response expression (39) can be viewed as result of the binary collision approach in the weak coupling regime. We have seen, furthermore, that systems in the semilinear coupling regime violate the linear coupling only in a small vicinity of the ion where $r < r_{\mathrm{c}}$. Small distances correspond to high momenta. This suggest to approximate the stopping power by using again the linear response, i.e. Born, result but to cut the k-integration at an upper limit $\approx 1/r_{\mathrm{c}}$ and to add a correction term which accounts for the excluded inner region of nonlinear coupling. This line of development has been introduced by Bloch for ion stopping by bound electrons in a gas target [20]. For the inner strong coupling region, the projectile–electron

interaction is much stronger than the atomic bonding. Thus he regarded the corresponding projectile–electron collisions with small impact parameter as collisions with a free electron and calculated them from a binary collision description using a pure Coulomb potential. The finally resulting well-known Bloch correction has then to be added to the Bethe formula for gas targets or in the case of an electron plasma to its analogue, the linear response stopping power (39). As Bloch assumed a pure Coulomb interaction for $r < r_c$ the strong coupling region and hence in our case r_c/λ must be very small. For a recent, quantitative discussion of the regimes of applicability of the Bloch correction see [120]. Extensions to higher ratios r_c/λ are provided by more elaborated correction terms which are discussed in the next subsection. Here we concentrate on the simpler, widely used approximation scheme of using cutoffs. Guided by the observation that the Bloch correction or similar correction terms reduce the linear response stopping by some amount the k-integration in the stopping power expression (39) is restricted by an upper limit k_m, i.e.

$$\frac{dE}{ds} = \frac{Z^2 e^2}{\varepsilon_0 (2\pi)^3} \int_{k < k_m} d^3k \, \frac{\boldsymbol{k} \cdot \hat{\boldsymbol{v}}}{k^2} \, \text{Im}\left[\frac{1}{\varepsilon_R(\boldsymbol{k}, \boldsymbol{k} \cdot \boldsymbol{v})} \right] , \tag{65}$$

where the cutoff parameter $k_m \gtrsim 1/r_c$ has to be defined suitably in order to exclude the small region $r < r_c$ of strong perturbation *and* to add the remaining effects of the close collisions in the average. This can be achieved by comparison with the binary collision approach using typical screened potentials, as will be discussed now.

The first step for this comparison is to work out a simplified closed expression for the stopping power (65). By interpolation between the known exact results in the limits of high and low velocities [115] one can deduce

$$\frac{dE}{ds} \approx Z^2 h(v) \ln(k_m \lambda) . \tag{66}$$

This approximation is valid for $k_m \lambda \gg 1$ and any Θ, v. The function $h(v)$ is linear in v for $v \ll \langle v_e \rangle$ and goes $\propto v^{-2}$ for $v \gg \langle v_e \rangle$ while λ can be identified as an effective velocity dependent screening length. Note that the validity condition $k_m \lambda \gg 1$ together with the typical value $k_m \sim 1/r_c$ nicely recovers the definition (22) of the semilinear regime. The approximation (66) applies also to the linear regime where k_m can be related to the averaged deBroglie wavelength as $k_m = 2/\langle \lambdabar_r \rangle = 2m\langle v_r \rangle/\hbar$.

The effective screening length $\lambda(v)$ read off from the dielectric approach can now be used to approximate the ion–electron interaction by $\phi_{ei}(r) = \phi_p(r)\exp(r/\lambda) = (Ze/4\pi\varepsilon_0 r)\exp(r/\lambda)$. In the limit of infinite projectile masses the projectile velocity is not a dynamical variable of the system and the velocity dependent potential interferes only as an external potential which can be employed in a binary collision treatment. The transport cross section for this Yukawa-like potential and the related stopping power have been much studied over the last decades, see for example Refs. [86,113,114,70,60,71,53]. It turns out that one can derive an approximation for the binary collision stopping power Eq. (59) which reads

$$\left(\frac{dE}{ds}\right)_{bc} \approx Z^2 \, \tilde{h}(v) \left[\ln\left(\frac{2\lambda}{\langle \lambdabar_r \rangle}\right) - \frac{1}{2}\ln(1 + \gamma^2 \langle \eta_p \rangle^2) \right] , \tag{67}$$

where $\ln \gamma = 0.577 \ldots$ is Euler's constant and $\tilde{h}(v)$ is very close to the $h(v)$ from Eq. (66) having exactly the same behavior for small and large velocities. The approximation (67) is valid for large arguments of the logarithm, i.e. $2\lambda/\langle \tilde{\lambda}_{\mathrm{r}} \rangle (1 + \gamma^2 \langle \eta_{\mathrm{p}} \rangle^2)^{1/2} \gg 1$, and for any coupling strength $\langle \eta_{\mathrm{p}} \rangle$. We now compare the binary collision approach with screened potential (67) with expression (66) obtained by a cutoff dielectric description. Both expressions are indeed very similar and we find the desired cutoff as

$$k_m = \frac{2}{\langle \tilde{\lambda}_{\mathrm{r}} \rangle} \frac{1}{\sqrt{1 + \gamma^2 \langle \eta_{\mathrm{p}} \rangle^2}} . \tag{68}$$

In the quantum mechanical plane wave regime $\langle \eta_{\mathrm{p}} \rangle \ll 1$, k_m becomes identical to the intrinsic cutoff $2/\langle \tilde{\lambda}_{\mathrm{r}} \rangle$, as provided from the behavior of the dielectric function $\varepsilon_{\mathbf{R}}$ (47), and Eqs. (65) and (66) merge into the exact linear response or Born-RPA result. In the classical limit $\langle \eta_{\mathrm{p}} \rangle \gg 1$ of ion–electron collisions with nonlinear coupling in the inner interaction region, the cutoff (68) tends to $k_m = 2/\gamma \langle \tilde{\lambda}_{\mathrm{r}} \rangle \langle \eta_{\mathrm{p}} \rangle \approx 1/\langle b_0 \rangle$, see Eq. (15). From the definition of r_{c} via the potential (19) and for the conditions $\langle b_0 \rangle \gg \langle \tilde{\lambda}_{\mathrm{r}} \rangle$ (i.e. $\langle \eta_{\mathrm{p}} \rangle \gg 1$) and $r_{\mathrm{c}} \ll \lambda$, which define the semilinear regime (see Eq. (22)), we obtain $r_{\mathrm{c}} \gtrsim \langle b_0 \rangle$. This yields finally $k_m \approx 1/b_0 \gtrsim 1/r_{\mathrm{c}}$ in agreement with the initial assumption when introducing the cutoff k_m.

Classical derivations of the stopping power [135] treat the electrons as classical particles and employ accordingly the Fried-Conte *plasma dispersion function* [55] which is the limit $\hbar \to 0$ of the RPA free density–density response (45) and provides the classical dielectric function. The classical dielectric function fails at large k-values and a cutoff is needed to render the k-integration in Eq. (39) finite. We identify $k_m \approx \min(1/\langle b_0 \rangle, 2/\langle \tilde{\lambda}_{\mathrm{r}} \rangle)$ as the commonly used cutoff in these classical dielectric approaches.

It has to be emphasized, however, that the cutoff (68) for the linear response stopping power in Eq. (65) is introduced to account for physical effects and not just as a mathematical tool to avoid divergences. The general linear response (Born-RPA) expression (39) yields a convergent integral by virtue of quantum effects which provide naturally an intrinsic cutoff at $2/\langle \tilde{\lambda}_{\mathrm{r}} \rangle$ at any degeneracy Θ including the case of classical targets $\Theta \gg 1$. The linear response stopping, however, is a valid approximation only for linear coupling $\langle \eta_{\mathrm{p}} \rangle \ll 1$ and becomes invalid in the semilinear and more so in the nonlinear regime. The physical cutoff discussed here intends to correct for a small region of strong perturbation at $r < r_{\mathrm{c}}$ and to extend the validity of the linear response expression into the semilinear regime. We remind that the linear regime never appears in an entirely classical system since $\hbar \to 0$ implies both $\Theta \to \infty$ and $\langle \eta_{\mathrm{p}} \rangle \to \infty$. The need of a cutoff is decided by the question whether we are in the linear or the semilinear regime, that is, by the parameter $\langle \eta_{\mathrm{p}} \rangle$, and independent of the degree of degeneracy Θ.

3.2.3. Corrections of linear response by binary collisions

So far we have seen that the comparison of the linear response description with cutoff k_m and the binary collision treatment with screening length λ provides a simple recipe to extend the linear response formalism into the semilinear regime with a minimum of calculational effort. The whole scheme, however, is based on several approximations as expressions (66) and (67) which are well justified only close to the linear regime. In order to proceed further into the semilinear coupling regime one should prefer more complete approaches to incorporate the binary collision

contributions from the strong coupling region. A first attempt in this direction was the Bloch correction mentioned above. Recently more elaborated schemes have been proposed in [61,132,124]. They are based on an idea of Gould and DeWitt [65] in context of deriving convergent collision integrals as needed for the calculation of transport properties in the framework of kinetic theory. Motivated by the corresponding diagrammatic expansion, see also e.g. [146], the cross section in the collision integral is estimated by composing three terms: The linear response or first order Born approximation (BI) for the dynamically screened Coulomb interaction and the binary collision result for a statically screened interaction are added while the linear response cross section for the statically screened interaction is subtracted to compensate for its appearance in the other terms. More precisely, the last term is the first order Born approximation of the binary collision term as well as the static limit of the dynamically screened linear response contribution. In other words, the composed cross section represents a T-matrix expression with a dynamically screened first order Born approximation but statically screened ladder terms of higher order. Translated to stopping powers we arrive at a combined expression $(dE/ds)_{com}$ consisting of the following three contributions

$$\left(\frac{dE}{ds}\right)_{com} = \left(\frac{dE}{ds}\right)_{BI}^{dyn} + \left(\frac{dE}{ds}\right)_{bc} - \left(\frac{dE}{ds}\right)_{BI}^{sta} .$$

(69)

Here $(dE/ds)_{BI}^{dyn}$ represents the Born-RPA, i.e. Eq. (63) taken in the limit of heavy projectiles $(m/M \to 0, \omega(\boldsymbol{k}) = \boldsymbol{k} \cdot \boldsymbol{v})$, which is equivalent to the linear response stopping power (39) with RPA-dielectric function ε_R. The static limit of this expression is obtained by replacing the dynamically screened interaction used in the cross section (62) and subsequently for deriving the Born-RPA stopping power (63) by the statically screened effective ion–electron interaction

$$V_p(k) = \frac{e\phi_p(k)}{\varepsilon_R(k, \omega = 0)} = \frac{Ze^2}{\varepsilon_0 k^2 \varepsilon_R(k, 0)} ,$$

(70)

which results in the third term

$$\left(\frac{dE}{ds}\right)_{BI}^{sta} = \frac{Z^2 e^2}{\varepsilon_0 (2\pi)^3} \int d^3k \, \hat{\boldsymbol{v}} \cdot \boldsymbol{k} \, \frac{Im[\varepsilon_R(k, \boldsymbol{k} \cdot \boldsymbol{v})]}{k^2 |\varepsilon_R(k, 0)|^2} .$$

(71)

The binary collision contribution $(dE/ds)_{bc}$ is equal to expression (59) where the transport cross section $\sigma_{tr}(p_r)$ has to be determined from the exact differential cross section $\sigma(p_r, \vartheta)$ for the statically screened potential V_p (70) calculated, for instance, from a phase shift analysis. A specification of this scheme to entirely classical systems is discussed in Section 4 together with a comparison to simulation results. More general expressions for arbitrary mass ratios are given in [61,124] where the different contributions are evaluated numerically for some specific target conditions and projectile parameters.

The combined expression (69) has several nice features. First, no external parameter appears in contrast to the cutoff approach. Furthermore, a smooth merging into the correct high velocity limit of linear coupling is guaranteed. For increasingly high velocities, where $\langle \eta_p \rangle \to 0$, the complete binary collision result turns into its first order Born approximation. Thus the last two terms $(dE/ds)_{bc} - (dE/ds)_{BI}^{sta}$ cancel gradually and leave solely the dynamical linear response contribution

$(dE/ds)_{BI}^{dyn}$. At low velocities the dynamically screened potential turns into the statically screened one and both the first order Born approximations $(dE/ds)_{BI}^{dyn}$ and $(dE/ds)_{BI}^{sta}$ become identical. The remaining binary collision term takes into account all the strong coupling effects. The resulting stopping power can thus be expected to be rather close to the exact one provided that linear response accurately reproduces the true statically screened interaction. In general, the whole scheme is essentially based on the assumption that the collective effects, static ones as well as dynamical ones, are well described by linear response. Since the collective phenomena take place on the scale of the actual screening length, i.e. at small momenta k, the strong interaction region must thus be small on this scale and hence restricted to high momenta. This immediately leads back to the definition of the semilinear regime, Eqs. (22) and (23), as the proper domain for such type of approximations. It may be extended to (weakly) nonideal plasmas by replacing the RPA dielectric function by the appropriate one which includes correlations within the target, see Section 3.1.4.

3.2.4. Binary collisions with effective screening lengths

In the previous approaches effective interactions served to provide binary collision contributions for correcting the linear response energy loss. Relying on binary collisions only widely used treatments are based on some parametrized screened Coulomb potentials typically in terms of Yukawa functions or related approximations. There, dynamical effects are frequently included in the average by employing velocity dependent screening length as, for instance, in deriving approximation (67). This should be easily feasible for low ion velocities where adiabaticity is guaranteed as well as for sufficiently high velocities where an effective screening length $\lambda(v)$ can be simply adjusted in the binary collision treatment to meet the exact high velocity result (44). The choice of an appropriate screening length becomes, however, crucial for imitating the dynamical effects at medium velocities and no assurance exists that the real dynamical situation can be treated in a satisfactory manner by a velocity dependent, but still statically screened ion–electron interaction. Here the combined expression (69) can provide a good starting point for constructing an effective screening length. First the statically screened potential is transfered, e.g. into a Yukawa potential by replacing $\varepsilon_R(k,0)$ with $1 + 1/(k\lambda)^2$. Now one can interpret Eq. (69) in a different manner by considering the difference $(dE/ds)_{BI}^{dyn} - (dE/ds)_{BI}^{sta}$ as a correction to the binary collision term $(dE/ds)_{bc}$. Demanding that the stopping power is given entirely by $(dE/ds)_{bc}$ the desired screening length $\lambda(v)$ can be read off from a numerical solution of $(dE/ds)_{BI}^{dyn} = (dE/ds)_{BI}^{sta}$. For this, admittedly quite phenomenological, approach again no external parameter is needed and the same restrictions to the semilinear regime apply as discussed in the previous subsection. It is resumed later on for classical systems and compared with numerical simulations in Section 4. Similar ideas have been proposed and investigated for atomic stopping by bound electrons in [118,119]. As it turns out in these investigations, however, this type of description yields for increasing coupling strength improved approximations compared with the theoretically better founded scheme, Eqs. (69)–(71).

3.2.5. Charge dependence at semilinear coupling

It emerges as a new feature in the semilinear regime that the Z^2-charge dependence of the stopping power is modified for low and medium velocities by correction terms which carry the charge dependence of the binary collision cross section, see e.g. [132]. Considering for instance again a Yukawa like screened Coulomb potential with screening length λ. There the transport cross section can be written as $\sigma_{tr}(p_r) = b_0^2 h(b_0/\lambda, \eta_p = b_0/\langle \dot{\lambda}_r \rangle)$ [120] where b_0 and η_p depend linearly

on Z. For $\eta_p \ll 1$ the function h turns into a function of $\langle \hat{\lambda}_r \rangle / \lambda$ only. This results in the quadratic Z dependence of the cross section in first Born approximation. Increasing η_p, however, is connected with a quite complex behavior of h as function of Z. For values of b_0/λ and η_p as characteristic for the semilinear regime h depends logarithmically on Z. This behavior is then recovered in the stopping approximations for semilinear coupling. It can be immediately read of from expressions (66) and (67) in connection with the definitions of $k_m(Z)$ (68) and $\langle \eta_p \rangle(Z)$ (16). To be more specific, the low velocity limit of the corrected linear response stopping power

$$\frac{\mathrm{d}E}{\mathrm{d}s} = -\frac{Z^2 e^2}{\varepsilon_0 (2\pi)^3 \omega_p} \frac{n}{v} \left[\tilde{C}(\xi, \Theta, |Z|) + \mathrm{O}(v^2) \right], \quad v \ll \langle v_e \rangle , \tag{72}$$

is now described by a dimensionless friction coefficient $\tilde{C}(\xi, \Theta, |Z|)$ with a logarithmic dependence on Z

$$\tilde{C}(\xi, \Theta, |Z|) \propto \ln \left(\frac{8\pi \varepsilon_0 m \langle v_e \rangle^2 \lambda_s(v=0)}{\gamma |Z| e^2} \right) . \tag{73}$$

for the semilinear coupling conditions $\langle b_0 \rangle / \lambda \ll 1$ and $\langle \eta_p \rangle \gg 1$.

For velocities larger than $\langle v_e \rangle$ but still small enough to fulfil $\langle \eta_p \rangle \gg 1$ we get the classical high velocity result of Bohr [21]

$$\frac{\mathrm{d}E}{\mathrm{d}s} \sim -\frac{Z^2 e^4}{4\pi \varepsilon_0^2 m v^2} n \ln \left(\frac{8\pi \varepsilon_0 m v^3}{\gamma |Z| e^2 \omega_p} \right), \quad v \gg \langle v_e \rangle, \langle \eta_p \rangle \gg 1 , \tag{74}$$

whereas still higher velocities lead back to linear coupling and the high velocity limit (44). We want to point out that the conditions for semilinear coupling imply large arguments of the logarithms in the above expressions.

3.3. Nonlinear ion–target coupling

The regimes of linear and semilinear coupling allowed to separate the problems of the ion–target coupling from the interactions within the target. The common concept was the linear response formulation which allows to describe the energy loss for a large variety of target conditions by the same basic relation (39) just adapting the dielectric function to the particular target condition. This changes if we proceed to nonlinear ion–target coupling. Now each parameter regime for projectile and target requires its own methods. In this section, we are going to discuss some of these methods to compute stopping in the nonlinear regime. We start in Section 3.3.1 with the Vlasov–Poisson equation which is designed to study nonlinear coupling effects in classical, ideal targets. The appropriate tool for classical, but nonideal targets is given by molecular dynamics (MD) simulations which are presented in Section 3.3.3. The wave nature of the electrons becomes crucial in two-component plasmas. This can be taken into account in a generalization of MD simulations, the wave-packet molecular dynamics (WPMD) where the pointlike electrons of the classical MD simulations are replaced by Gaussian wave-packets. This will be discussed in Section 3.3.4. The WPMD adds quantum effects of wave nature and allows to treat weakly degenerate targets ($\Theta \lesssim 1$). For fully degenerate targets ($\Theta \ll 1$), density functional methods are a widely used tool in all fields

of electron physics. The basic aspects of density functional approaches, the local density approximation (LDA) and its time dependent extension (TDLDA) are outlined in Section 3.3.5, an application to stopping is reported in Section 3.3.6. There are, furthermore, some promising concepts for future work. An extension of the Vlasov equation to treat ideal and degenerate ($\Theta \leq 1$) electron plasmas is sketched in Section 3.3.2. In Section 3.3.7, we present an expression for the stopping power at low velocities in terms of a force–force correlation function, which offers an access to nonlinear stopping by means of the simpler equilibrium descriptions of the ion–target system.

3.3.1. Vlasov–Poisson for classical ideal targets

We first consider the Vlasov equation in the regime of classical ($\Theta \gg 1$, $\langle \eta_e \rangle > 1$) and ideal ($\Gamma \ll 1$) electron plasmas. Ideal targets allow a mean-field treatment of the electrons because correlation effects are negligible. The electron cloud is described in terms of a phase-space distribution $f(\mathbf{r}, \mathbf{u}, t)$ and it is propagated by the Vlasov equation

$$\frac{\partial f}{\partial t} + \mathbf{u} \cdot \frac{\partial f}{\partial \mathbf{r}} + \frac{e}{m} \frac{\partial \phi}{\partial \mathbf{r}} \cdot \frac{\partial f}{\partial \mathbf{u}} = 0 \tag{75}$$

using the static electric potential ϕ as given by the Poisson equation

$$\Delta \phi(\mathbf{r}, t) = -\frac{\varrho_p}{\varepsilon_0} - \frac{\varrho_{ind}}{\varepsilon_0} = -\frac{Ze}{\varepsilon_0} \delta^3(\mathbf{r} - \mathbf{v}t) + \frac{e}{\varepsilon_0} \left[\int f(\mathbf{r}, \mathbf{u}, t) \, \mathrm{d}^3 u - n \right]. \tag{76}$$

Here n is the number density of the target electrons in absence of the ion. It serves here as a homogeneous neutralizing background. This electrostatic approximation is valid for nonrelativistic ion and electron velocities. The induced electric field $\mathscr{E}_{ind} = -\nabla \phi_{ind}$ at the ion position or alternatively the induced electron density provided by a solution of Eqs. (75) and (76) yields the stopping power by virtue of Eq. (6).

The Vlasov–Poisson equation requires ideal targets but is applicable for any strength of the ion–electron potential. The regime of weak coupling is also accessible and it is interesting to look first at the Vlasov equation in that well understood coupling regime. The relative strength of the ionic perturbation can be estimated as

$$\frac{e}{m} \frac{\partial \phi_p}{\partial \mathbf{r}} \cdot \frac{\partial f}{\partial \mathbf{u}} \bigg/ \left(\mathbf{u} \cdot \frac{\partial f}{\partial \mathbf{r}} \right) \approx \sqrt{3} Z \Gamma^{3/2} \frac{v_{th}^3}{u_s^3} \frac{r_s}{|\mathbf{r} - \mathbf{v}t|}, \tag{77}$$

where we have employed a typical velocity scale u_s, a typical length scale $r_s = u_s t_s = u_s / \omega_p$, and as typical time scale one plasmon cycle $t_s = \omega_p^{-1} = (m\varepsilon_0 / e^2 n)^{1/2}$ together with the relation $\Gamma^{3/2} = \omega_p^3 / 4\pi \sqrt{3} n v_{th}^3$ for the classical plasma parameter (13). The factor $\sqrt{3} |Z| \Gamma^{3/2} v_{th}^3 / u_s^3$ characterizes obviously the strength of the perturbation by the ion. A natural and often used choice for the velocity scale is the thermal velocity, $u_s = v_{th}$. The strength of the perturbation becomes then $\sqrt{3} |Z| \Gamma^{3/2} = |Z| / 3N_D$ where N_D is the number of particles in the Debye sphere, see Eq. (25). Weak perturbations are defined by $|Z| / 3N_D \ll 1$. They allow an expansion in orders of the perturbation Z/N_D. The linear terms of the Vlasov–Poisson equation yield the classical dielectric description ([87], Section 3.4) and its stopping power [135]. The linearized Vlasov–Poisson equation can be

solved formally using Fourier transformation (see Appendix B.3). There results the dielectric function $\varepsilon_{cl}(k, \omega)$ for classical electron plasmas [135,55]

$$\varepsilon_{cl}(k, \omega) = 1 + \frac{e^2 n}{m \varepsilon_0 k^2} \int d^3 u \, \boldsymbol{k} \cdot \frac{\partial f_0(u)}{\partial \boldsymbol{u}} \frac{1}{\omega - \boldsymbol{k} \cdot \boldsymbol{u} + i0} \, , \qquad (78)$$

where $f_0(u) = (m/2\pi k_B T)^{3/2} \exp(-mu^2/2k_B T)$ is a Maxwell distribution. This classical dielectric function ε_{cl} is the limit $\hbar \to 0$ of the RPA dielectric function ε_R (47) and reproduces correctly the long wavelength (small k) behavior of ε_R at $\Theta \gg 1$ where quantum effects can be safely neglected [7]. One thus obtains from the linearized Vlasov–Poisson equations the classical version of all linear response quantities and observables connected with ε_{cl} (see Section 3.1.1) and the linear response stopping power (39). The second order of the expansion in Z/N_D yields the Z^3-Barkas contribution mentioned in Section 3.1.8.

A closer inspection reveals that a more relevant energy scale is associated with the mean relative velocity between ion and electron, $u_s = \langle v_r \rangle = v_{th} \langle v_r \rangle'$. This choice suggests that the essential expansion parameter is $Z/N_D(\langle v_r \rangle')^3$ instead of Z/N_D [51,154]. There is, however, a basic problem with the classical approach to the stopping power. It yields diverging integrals which require the introduction of an upper cutoff k_m in the final quadratures of, e.g., Eq. (39). This feature can be nicely seen from Eq. (77). The Coulomb potential of the ion diverges at $\boldsymbol{r} \to \boldsymbol{v}t$ however small the prefactor may be. This demonstrates that the linearized Vlasov–Poisson equation is only applicable for relative distances $r/\lambda > \sqrt{3}|Z|\Gamma^{3/2}/(\langle v_r \rangle')^3$, where $\lambda = \langle v_r \rangle / \omega_p$ is the dynamical screening length in an ideal plasma. The condition is, of course, only relevant for radii $r < \lambda$ which, in turn, requires $\sqrt{3}|Z|\Gamma^{3/2}/(\langle v_r \rangle')^3 \ll 1$. We thus recover the definition of the semilinear regime (25) where the parameter $\sqrt{3}|Z|\Gamma^{3/2}/(\langle v_r \rangle')^3 = \langle b_0 \rangle / \lambda$ marks the boundary between the semilinear and the nonlinear coupling regime. In summary, the linearization or, more general, the expansion of the Vlasov–Poisson equations is applicable in a parameter region which coincides with the semilinear coupling regime and provides approximations for the stopping power depending on a cutoff as discussed earlier in Section 3.2.2. We see also that the condition for linear coupling is here always violated in a sufficiently small vicinity of the ion.

Numerical solutions of Eqs. (75) and (76) are unavoidable in the regime of nonlinear coupling. The Poisson equation Eq. (76) is usually solved on a spatial grid. There are various methods available for that task. A particularly efficient method employs fast Fourier transformation to obtain the potential ϕ_{ind} for a given charge density ϱ_{ind} [106]. There are two different schemes for the propagation of the Vlasov equation (75), either by finite element techniques on a grid in phase space or by particle-in-cell (PIC) techniques [80]. The direct solution of the Vlasov equation in six-dimensional phase space is extremely demanding concerning memory requirements, still beyond nowadays technical limits. There exist, however, solutions of the Vlasov–Poisson equations for a reduced four dimensional phase space (r, z, v_r, v_z) corresponding to a cylindrical simulation box, achieved with the help of massively parallel supercomputers [23]. The more efficient alternative is the PIC treatment where the phase-space distribution is represented by a swarm of pseudo-particles. These are propagated according to Newton's equations of motion in the potential ϕ. The (moderate) effort to solve the Poisson equation on the spatial, i.e. three-dimensional, grid remains the same. But the propagation of the Vlasov equation is much accelerated because the numerical expense depends only linearly on the number of pseudo-particles. And this number is to

be adapted to the spatial grid (rather than the full phase-space grid) to achieve a sufficiently smooth representation of the electron density on the grid. Typically, a few pseudo-particles per grid cell are necessary. Two basically different scenarios are conceivable. In the one case, one pseudo-particle stands as a "macro particle" for many physical electrons. This is the genuine PIC scheme. In the other case, one physical electron is represented by many pseudo-particles. This is the regime of test-particle simulations, typically applied in dense fermion systems where the Vlasov equation is thought to represent the classical limit of a quantal phase-space distribution [18]. The PIC simulations are usually very efficient and allow to perform the computation on work stations at the expense of some fluctuations, or noise, however in the results. The noise can be suppressed, if necessary, by enhancing the number of pseudo-particles. The PIC technique was applied recently to determine the stopping power in cylindrical 2-D spatial geometry [81,38] and in full 3-D space [196,199,200].

The problem with the Coulomb singularity at small distances is also present in these numerical solutions. One usually smoothes the ionic $1/r$ potential for $r \to 0$, either explicitly [22] or implicitly by the finite resolution of the spatial grid. The PIC simulations of [196,199,200] use the full ionic Coulomb potential by switching to piecewise analytical solutions for the 2-body Coulomb problem of a pseudo-particle close to the ion. This scheme was taken over from the MD simulations for ion stopping which will be discussed in Section 3.3.3 and in Appendix A.2. There is, however, a price to be paid for this achievement: High resolution at small distances limits the size of the simulation box if the number of test particles is kept fixed (which is usually the case due to technical limitations). The box size, in turn, sets an upper limit on the wave length in the description. Thus, a high spatial resolution can run into a conflict with long-range phenomena. The appropriate compromise depends on the actual problem. The stopping power at high velocities requires a reasonable treatment of the dynamical screening at long wavelengths, whereas high resolution of the order of the static screening length is necessary for studies in the low velocity regime. Results are presented and discussed in Section 4.

We mention in passing that it is not guaranteed that a solution for the Vlasov–Poisson equations (75) and (76) exists, because of the singular external potential $\phi_p \propto 1/r$. However, for any smooth potential related to an external charge distribution with a continuous first derivative solutions with a stable time evolution in the neighborhood of stationary solutions have been proven to exist [150].

3.3.2. Fermionic Vlasov equation

The Vlasov equation (75) will fail for dense Fermion systems where the degeneracy is high, i.e. $\Theta \ll 1$. This regime calls, in principle, for fully quantal methods as time-dependent Hartree–Fock or TDLDA (see Section 3.3.5, for an example of an application to dense hydrogen see [85]). The full treatment of all quantum aspects, however, grows quickly very expensive and inhibits all calculations with large samples. But one can take advantage from noting that there are two different quantum effects: wave nature of the particles and Pauli principle. And there are cases where the wave nature of the fermions can still be well approximated by classical propagation but where the phase-space density grows so large that the Pauli principle becomes crucial [148]. For electrons, this is the regime of high degeneracy, $\Theta < 1$, but still large Coulomb parameter $\langle \eta_e \rangle > 1$. The most widely used solution for that problem is to continue to use the Vlasov equation but to start from an initial distribution which respects the Pauli principle, often chosen as the Fermi

distribution instead of the classical Maxwell distribution. This strategy provides reliable results for a certain (small) time interval. And so, the Vlasov equation has been successfully applied for studies of nuclear dynamics in energetic heavy-ion reactions [18]. Nevertheless, the violation of the Pauli principle develops with time and sooner or later the Vlasov results become unreliable. The problem can be traced back to the finite resolution in any numerical treatment which induces artificial dissipation. This dissipation then drives relaxation towards the classical Boltzmann equilibrium distribution which, of course, violates the Pauli principle at low enough temperature [148]. The actual time scale of the relaxation depends on the number of test particles. But it is often interfering with the time scale of the studied processes, see [148] for the case of nuclear dynamics and for the case of electrons in metal clusters [44]. A possible solution of this problem is to complement the Vlasov equation by a dedicated collision term which scans the violations of the Pauli principle, i.e. occurrences of $f > 1$, and collides fermions out of these dangerous areas in phase space. It was shown that such a scheme is manageable and successful, for the case of nuclei in [149] and for electron systems in [45], respectively. The modified Vlasov equation respects the Pauli principle to a good approximation and over arbitrarily long times. This opens the way to test-particle simulations of large systems in degenerate, but otherwise ideal, plasmas.

3.3.3. Molecular dynamics simulations

We now consider entirely classical projectile–target systems which are nondegenerate, $\Theta \gg 1$, have a large Coulomb parameter for the electrons, $\langle \eta_e \rangle > 1$, and nonlinear ion–target coupling corresponding to classical ion–electron collisions, $(\langle \eta_p \rangle > 1)$. We want to have no restriction on the coupling strength within the target, i.e. on the ideality $\xi(\Theta \gg 1) = \Gamma$. Molecular dynamics (MD) simulations provide a suitable tool to study the full many-body dynamics of these systems, see e.g. [4]. They have been successfully applied to various strongly coupled systems during the last decades, in particular, to classical Coulomb systems as the one component plasma (OCP) or (binary) ionic mixtures [73,75]. They are also a powerful tool to compute stopping of a heavy ion in an electron OCP, i.e. to study the ion–electron system as described by the Hamilton operator (2) [191–197,199–201]. The procedure is conceptually very simple: the ion and the electrons just follow the classical equations of motion with mutual Coulomb interactions

$$\frac{d\boldsymbol{r}_i}{dt} = \boldsymbol{u}_i, \qquad \frac{d\boldsymbol{u}_i}{dt} = -\frac{1}{m}\frac{\partial}{\partial \boldsymbol{r}_i}\left[\sum_{j \neq i}\frac{e^2}{4\pi\varepsilon_0|\boldsymbol{r}_i - \boldsymbol{r}_j|} - \frac{Ze^2}{4\pi\varepsilon_0|\boldsymbol{r}_i - \boldsymbol{R}|}\right],$$

$$\frac{d\boldsymbol{R}}{dt} = \boldsymbol{v}, \qquad \frac{d\boldsymbol{v}}{dt} = \frac{1}{M}\frac{\partial}{\partial \boldsymbol{R}}\sum_i \frac{Ze^2}{4\pi\varepsilon_0|\boldsymbol{r}_i - \boldsymbol{R}|}, \tag{79}$$

where $\{\boldsymbol{r}_i, \boldsymbol{u}_i, i = 1, \dots, N\}$ are the electronic and $(\boldsymbol{R}, \boldsymbol{v})$ the ionic coordinates. These equations are solved with standard numerical algorithms. The events where an electron comes close to the ion need to be singled out and propagated separately in order to cope with the Coulomb singularity at $r \to 0$. Observables are measured as time averages over a certain time interval or as ensemble averages over different initial configurations. To compute the stopping power, an equilibrium state of the electron system is produced first by a MD propagation without the ion. Then the ion is

added and its energy loss ΔE as well as travelling distance Δs are determined over a sufficient long time τ. The ratio $\Delta E/\Delta s(\tau)$ is the time averaged stopping power. Heavy ions have negligible change in velocity during the measuring time interval and thus $\Delta E/\Delta s$ represents immediately the stopping power for the given (initial) ion velocity v. Further technical details of the MD-simulations are outlined in Appendix A.1 and the results are discussed in Section 4.

The MD simulations contain without restriction all correlation effects, dynamical screening, close collisions, and even multi-particle correlations. They do not rely on a spatial grid for the Coulomb force and thus there is no restriction in the spatial resolution. On the other hand the expense grows quadratically with the particle number N because the Coulomb force is to be evaluated separately for each pair of particles. The available computing power thus limits the computation to at most a few thousand particles. Typical MD simulations use 500 electrons and can still be performed on small work stations. In order to approximate an infinite plasma by this finite particle number, the electrons are packed into an elementary cubic simulation box and this box is continued periodically in all three spatial directions.

The limited simulation box hence introduces a largest length scale on which collective phenomena can be explored. This limitation is unimportant for strongly coupled targets ($\Gamma > 1$) and low projectile velocities because the screening length is then small compared to the size of the simulation box. It becomes a real problem, however, at high projectile velocities where a spatially extended wake field is induced by the ion. But then one leaves anyway the regime of nonlinear coupling and can continue with the simpler linear response methods. This example shows that MD simulations are particularly suited for the case of strong coupling and become inefficient, if not impossible, just where linear response is valid.

We mention in passing that there are attempts to overcome the quadratic growth of expense in the MD simulations by a mixed strategy. The particles are collected in spatial cells and the Coulomb force from remote cells is computed globally. The necessary book-keeping is managed using tree structures, immediately suited for coding in what one calls "tree codes" [16,152,167,137]. The method succeeds in cutting the quadratic growth of expense. But there comes first an enormous overhead of book keeping which makes these tree codes competitive only for very large ensembles around 8000 particles and larger.

The MD-simulations are based on a pure classical treatment. This implies the restriction to parameters where the ion–target system behaves classically. As a consequence, no ground state of the classical ($\hbar \to 0$) ion–target system exists and the dynamics at long time scales ends up in a Coulomb collapse where some electrons get deeper and deeper bound in the ion potential by transferring energy and momentum in interactions with the surrounding electrons. This problem is not explored in the dynamical non-equilibrium simulations of stopping where only a short time interval after switching on the ion–electron interaction is of interest. The Coulomb collapse, however, inhibits straightforward classical MD simulations to a two component target plasma for which no classical equilibrium state exists. A way out of this dilemma is to introduce effective interactions which account for quantum effects by an appropriate smoothing of the Coulomb potential at short distances [39–41,97,74,76,56]. These effective interactions are deduced from an exact solution of the two-body quantum problem at thermal equilibrium. This restricts the method to situations close to equilibrium. Truly non-equilibrium simulations require still other approaches, as e.g. the wave-packet molecular dynamics which is presented in the next subsection.

3.3.4. Wave-packet molecular dynamics (WPMD) in the quantum, nonlinear, nonideal regime

The classical MD simulations, as outlined in the previous subsection, are conceptually simple and provide nonetheless a fairly complete description including all sorts of correlations. But often enough one cannot completely neglect quantum effects. Dense systems are likely to run into the degenerate regime $\Theta \lesssim 1$. Such a situation can be mastered when using the fermionic Vlasov equation as outlined in Subsection 3.3.2. But one often needs also to take care of the wave nature of the electrons, $\eta_e \lesssim 1$, e.g., to reach a stable equilibrium for two-component plasmas. There are several techniques for a fully quantum mechanical description of coupled electron–ion systems, e.g. the path-integral Monte Carlo method [32,111] or ionic MD on electronic Born–Oppenheimer surfaces [30,85]. These powerful techniques allow detailed calculations with compromises resulting mainly from exchange, e.g. treatment of nodes in the density matrix. But they are extremely expensive and limited to situations close to equilibrium.

In order to deal with quantum systems ($\eta_e \lesssim 1$) which also may be far from equilibrium, one has to use a time-dependent quantum mechanical propagation for the electrons. But this is an extremely demanding task. The aim is an approximate quantum treatment which comes from the classical molecular dynamics side, thus maintaining its simplicity as well as its correlation content, and adds just the most basic quantum features, as e.g. finite extension and uncertainty principle. This is achieved by using localized wave packets with a simple analytical form. Such a wave packet dynamics based on Gaussians has been explored in [78,98,99]. It is called wave-packet molecular dynamics (WPMD). The use of Gaussian wave packets yields simple analytical expressions which allow an efficient coding, and it provides an exact solution in two limiting cases: a free particle and a particle in an harmonic oscillator potential. It is still a very good approximation if the width of the wave packet is smaller than the typical length scale of variation of the potential, i.e., if the potential can be approximated locally by a harmonic oscillator [78].

We discuss here the WPMD for a Coulomb system of ions, treated classically, and electrons. The state at a given time t is thus specified by

$$\{\boldsymbol{R}_I(t), \boldsymbol{P}_I(t), \Psi(\boldsymbol{x}_1, \ldots, \boldsymbol{x}_N; t)\} \,, \tag{80}$$

where $\boldsymbol{R}_I(t)$ and $\boldsymbol{P}_I(t)$ describe the positions and momenta of the ions and $\Psi(\boldsymbol{x}_1, \ldots, \boldsymbol{x}_N; t)$ is the many-particle wave function for the electrons. The dynamics of this sytem is governed by the Hamiltonian

$$\hat{H} = \mathscr{H}^{\text{ion}}(\boldsymbol{R}_I, \boldsymbol{P}_I) + \hat{H}^{\text{el.}}(\hat{\boldsymbol{x}}_i, \hat{\boldsymbol{p}}_i) + \hat{H}^{\text{ion-el.}}(\boldsymbol{R}_I, \hat{\boldsymbol{x}}_i) \,. \tag{81}$$

The Hamilton function

$$\mathscr{H}^{\text{ion}}(\boldsymbol{R}_I, \boldsymbol{P}_I) = \sum_I \frac{P_I^2}{2M} + \frac{1}{4\pi\varepsilon_0} \sum_{IJ} \frac{Z^2 e^2}{|\boldsymbol{R}_I - \boldsymbol{R}_J|} \tag{82}$$

determines the dynamics of the ions with mass M and charge Ze, and the Hamilton operator

$$\hat{H}^{\text{el.}}(\hat{\boldsymbol{x}}_i, \hat{\boldsymbol{p}}_i) = \sum_i \frac{\hat{p}_i^2}{2m} + \frac{1}{4\pi\varepsilon_0} \sum_{ij} \frac{e^2}{|\hat{\boldsymbol{x}}_i - \hat{\boldsymbol{x}}_j|} \tag{83}$$

the dynamics of the electrons with mass m. Finally, the electron–ion interaction is given by

$$\hat{H}^{\text{ion-el.}}(\boldsymbol{R}_I, \hat{\boldsymbol{x}}_i) = -\frac{1}{4\pi\varepsilon_0} \sum_{I_i} \frac{Ze^2}{|\boldsymbol{R}_I - \hat{\boldsymbol{x}}_i|} \ . \tag{84}$$

The equations-of-motion are derived from the principle of stationary action [104] which yields

$$\dot{\boldsymbol{R}}_I = \partial_{P_I} \langle \Psi | \hat{H} | \Psi \rangle, \qquad \dot{\boldsymbol{P}}_I = -\partial_{R_I} \langle \Psi | \hat{H} | \Psi \rangle \ , \tag{85}$$

$$\delta \int_{t_1}^{t_2} dt \left\langle \Psi \left| i\hbar \frac{d}{dt} \right| \Psi \right\rangle = \delta \int_{t_1}^{t_2} dt \langle \Psi | \hat{H} | \Psi \rangle \ . \tag{86}$$

These equations are still equivalent to the time dependent Schrödinger equation if the variational wavefunctions are allowed to exhaust the full Hilbert space. But then the system of equations is not tractable for a true many-body system. A very simple approximation for the electron propagation is needed to allow for long-time studies for large probes.

To this end, the electrons are parametrized as Gaussian wave packets, i.e.

$$\Psi(\boldsymbol{x}_1, \ldots, \boldsymbol{x}_N; t) \approx \mathscr{A} \left\{ \prod_i \varphi_i(\boldsymbol{x}_i; t) \right\} \ , \tag{87}$$

$$\varphi_q(\boldsymbol{x}) = \left(\frac{3}{2\pi\gamma^2} \right)^{3/4} \exp\left[-\left(\frac{3}{4\gamma^2} + \frac{ip_\gamma}{2\hbar\gamma} \right)(\boldsymbol{x} - \boldsymbol{r})^2 - \frac{i\boldsymbol{p}}{\hbar}(\boldsymbol{x} - \boldsymbol{r}) \right] \ , \tag{88}$$

with the variational parameters $\boldsymbol{q} = (p_\gamma, \gamma, \boldsymbol{p}, \boldsymbol{r})$, where $\boldsymbol{p}$ and $\boldsymbol{r}$ are the classically conjugate parameters for the position and p_γ and γ for the width. The antisymmetrization operator is denoted by $\mathscr{A}$. The complete antisymmetrization limits the approach to small systems [52,130]. A manageable compromise is obtained if one expands antisymmetrization in orders of exchanges and keeps only terms up to 2-body exchange [98–100]. Thus WPMD permits at this stage studies in the regime $\Theta \lesssim 1$, but further extensions are necessary for the completely degenerate case.

With the parametrized ansatz (88) the dynamics of the electron wavefunction is reduced to a "classical" dynamics of the parameters $\boldsymbol{q}$. Application of the variational principle (86) to a parametrized wave function yields

$$\sum_\mu N_{\nu\mu} \dot{q}_\mu = \frac{\partial H}{\partial q_\nu} \ . \tag{89}$$

which differs from a straightforward Hamiltonian equation by the occurrence of the norm overlap [147]

$$N_{\nu\mu} = i\hbar \langle \overleftarrow{\partial}_{q_\nu} \overrightarrow{\partial}_{q_\mu} - \overleftarrow{\partial}_{q_\mu} \overrightarrow{\partial}_{q_\nu} \rangle \ . \tag{90}$$

Hamiltonian dynamics is recovered only if the norm overlap takes a symplectic form

$$N_{\nu\mu} = \begin{pmatrix} 0 & \hat{1} \\ -\hat{1} & 0 \end{pmatrix} \ , \tag{91}$$

where $\hat{1}$ is the unit matrix in the $4N \times 4N$ subspace. It is one of the advantages of the particular form (88) for the single electron wavepacket that the norm overlap N_0 without any exchange is

independent of time and always symplectic which makes the equations-of-motion for q particularly simple. Including 2-particle exchanges, one obtains a correction δN to the norm matrix. The correction to the inverse norm matrix is calculated according to

$$N^{-1} \approx N_0^{-1} - N_0^{-1}\delta N N_0^{-1} \, . \tag{92}$$

One thus finds that the expectation value of $\hat{H}$ over the wavepackets

$$\mathcal{H}(\boldsymbol{R}_I, \boldsymbol{P}_I, \boldsymbol{r}_i, \boldsymbol{p}_i, \gamma_i, p_{\gamma_i}) = \langle \hat{H} \rangle \tag{93}$$

acts as a classical Hamilton function. It comes as an additional advantage of the ansatz (88) that this expectation value can be performed analytically for a Coulomb system leading to an expression which contains only elementary functions. This is crucial for a fast propagation algorithm. Taking all pieces together, one can describe the dynamics of the plasma by the generalized classical Hamilton function

$$\mathcal{H} = \mathcal{H}^{\text{el.}}(\boldsymbol{r}_i, \boldsymbol{p}_i, \gamma_i, p_{\gamma_i}) + \mathcal{T}_2^{\text{Pauli}}(\boldsymbol{r}_i, \boldsymbol{p}_i, \gamma_i) \tag{94}$$

$$+ \mathcal{H}^{\text{ion}}(\boldsymbol{R}_I, \boldsymbol{P}_I) + \mathcal{H}^{\text{ion-el.}}(\boldsymbol{R}_I, \boldsymbol{r}_i, \gamma_i) \, , \tag{95}$$

where

$$\mathcal{H}^{\text{el.}}(\boldsymbol{r}_i, \boldsymbol{p}_i, \gamma_i, p_{\gamma_i}) = \sum_i \frac{1}{m}\left(\frac{p_{\gamma_i}^2}{2} + \frac{9\hbar^2}{8\gamma_i^2} + \frac{p_i^2}{2}\right) + \frac{e^2}{4\pi\varepsilon_0}\sum_{ij}\left[\frac{1}{|\boldsymbol{r}_i - \boldsymbol{r}_j|}\text{erf}\left(\frac{|\boldsymbol{r}_i - \boldsymbol{r}_j|\sqrt{3}}{\sqrt{2(\gamma_i^2 + \gamma_j^2)}}\right)\right.$$

$$\left. + \mathcal{V}_{\text{Ewald}}(\boldsymbol{r}_i - \boldsymbol{r}_j)\right], \tag{96}$$

$$\mathcal{T}_2^{\text{Pauli}}(\boldsymbol{r}_i, \boldsymbol{p}_i, \gamma_i) = \sum_{ij}\frac{\hbar^2}{m}\exp(-\Delta_{ij}^2)\frac{3\gamma_i\gamma_j}{(\gamma_i^2 + \gamma_j^2)}\frac{3(\gamma_i^2 - \gamma_j^2)^2 + 4\gamma_i^2\gamma_j^2\Delta_{ij}^2}{(\gamma_i^2 + \gamma_j^2)^3 - 8(\gamma_i\gamma_j)^3\exp(-\Delta_{ij}^2)} \, , \tag{97}$$

$$\mathcal{H}^{\text{ion}}(\boldsymbol{R}_I, \boldsymbol{P}_I) = \sum_I \frac{P_I^2}{2M} + \frac{Z^2 e^2}{4\pi\varepsilon_0}\sum_{IJ}\left[\frac{1}{|\boldsymbol{R}_I - \boldsymbol{R}_J|} + \mathcal{V}_{\text{Ewald}}(\boldsymbol{R}_I - \boldsymbol{R}_J)\right], \tag{98}$$

$$\mathcal{H}^{\text{ion-el.}}(\boldsymbol{R}_I, \boldsymbol{r}_i, \gamma_i) = \frac{Ze^2}{4\pi\varepsilon_0}\sum_{Ii}\left[\frac{1}{|\boldsymbol{R}_I - \boldsymbol{r}_i|}\text{erf}\left(\frac{|\boldsymbol{R}_I - \boldsymbol{r}_i|\sqrt{3}}{\gamma_i\sqrt{2}}\right) + \mathcal{V}_{\text{Ewald}}(\boldsymbol{R}_I - \boldsymbol{r}_i)\right], \tag{99}$$

$$\mathcal{V}_{\text{Ewald}}(\boldsymbol{r}) = \sum_l{}'\left(\frac{1}{|\boldsymbol{r} + l L|} - \frac{1}{|l L|}\right). \tag{100}$$

Evaluating Eq. (86) in terms of two body exchanges in the two body center of mass frame yields the expression (97) where the phase space distance

$$\Delta_{ij}^2 = \frac{2(\gamma_i\gamma_j)^2}{3(\gamma_i^2 + \gamma_j^2)\hbar^2}(\boldsymbol{p}_i - \boldsymbol{p}_j)^2 + \frac{3}{2(\gamma_i^2 + \gamma_j^2)}(\boldsymbol{r}_i - \boldsymbol{r}_j)^2 \tag{101}$$

shows that the expansion parameter for the hierarchy of n-body exchanges is e^{-A^2}. By measuring this parameter, the validity of the approximation is checked during propagation. Technically, the two-body exchange effects are incorporated in Eq. (97) as an additional effective electron–electron potential. Note the occurrence of the Ewald potentials (100) in every Coulomb term. This accounts for the Coulomb interactions with the particles in the periodically continued simulation boxes which are used to simulate infinite systems with a finite sample. Details on the solution of the pseudo-hamiltonian equations (89)–(101) are given in Appendix A.3.

The criterion for the validity of a classical approach is that the thermal wavelength $A = \hbar/\sqrt{mk_\mathrm{B}T}$ should stay safely below the average inter electron distance, i.e. the Wigner–Seitz radius $a = (3n/4\pi)^{-1/3}$. The limit of purely classical dynamics would be recovered if the forces vary sufficiently slowly over the width of the wave packet,

$$\frac{\gamma^3 \,\overline{V_r^3 V}}{\sqrt{[(E - V)\ (\hbar^2/m\gamma^2)]}} \ll 1 \ , \tag{102}$$

where γ is the width of the wavepacket and $\overline{V_r^3 V}$ a typical value for the curvature of the force. Note the order of the derivative. Up to a purely harmonic potential $V \propto r^2$ the WPMD propagation is exact. On the other hand Eq. (102) cannot be fulfilled everywhere for a Coulomb potential.

The WPMD includes at least the same amount of correlations as classical molecular dynamics. This is seen, e.g., by making the width of the wavepacket proportional to the thermal wavelength and keeping it fixed during the simulation. Then, the method yields the same results as traditional molecular dynamics simulations employing effective potentials. The purpose of the WPMD reaches farther out to true non-equilibrium situations. This is achieved by allowing the width of the wave packets its own dynamics which can adjust itself to the temperature and density of the system.

The WPMD contains enormous simplifications in order to allow for the handling of large ensembles. This implies, of course, severe approximations. We have already seen that the expansion of exchange limits the regime of acceptable degeneracy to $\Theta \lesssim 1$, in practice to $\Theta > 1/10$. There is, furthermore, the requirement that the widths have to stay below the size of the simulation box. This is guaranteed for systems which have predominantly localized electrons, as e.g. a dense hydrogen plasma consisting of H_2-molecules, atoms and possibly larger clusters. In other cases an unphysical growth of the delocalization can be prevented by adding to Eq. (96) a suitably tailored potential $\Delta \mathscr{H}^{\mathrm{el.}}(\gamma_i)$ whose parameters are fixed by fitting a known observable of the OCP, e.g. the potential energy, see for example Chapter 3.2 of Ref. [91].

3.3.5. Local energy-density functionals: The Kohn–Sham equations, LDA and TDLDA

As outlined in Section 3.1.4, where we discussed the LFCs, density functional approaches aim to incorporate higher correlations into mean field calculations by virtue of an effective interaction, where quite general theorems guarantee the existence of such effective interactions [84,102,151]. While the LFC deals with homogeneous many-electron systems and inserts nonideality effects in the linear response, inhomogeneous systems, as atoms, molecules, surfaces, or in our particular case the inhomogeneity from the projectile ion U_{ext}, add further complications and different (even simpler) approaches are needed as starting point. A very efficient and widely used scheme are the Kohn–Sham equations with exchange and correlations in Local-Density Approximation (LDA), for extensive reviews see [46,96]. We discuss it here for the fully degenerate case ($\Theta = 0$) which is

the typical regime of applications for the LDA. It is based on a variational formulation starting from an expression for the total energy in the form

$$E_{\text{tot}} = E_{\text{kin}}(\{\varphi_\alpha\}) + E_{\text{Coul}}(n(\boldsymbol{r})) + E_{\text{xc}}(n(\boldsymbol{r})) + \int \text{d}^3 r \, n(\boldsymbol{r}) U_{\text{ext}}(\boldsymbol{r}) \tag{103}$$

and referring to the local electron density

$$n(\boldsymbol{r}) = \sum_\alpha |\varphi_\alpha(\boldsymbol{r})|^2 \ . \tag{104}$$

Note the dependencies: the Coulomb energy depends naturally on the local density, the exchange-correlation energy is *approximated* by a local density form, and the full dependence on the single electron wavefunction φ_α is carried through for the kinetic energy which serves to maintain the quantum shell structure. The Kohn–Sham equations are obtained by variation with respect to the φ_α^* which yields

$$\left(\frac{\hat{p}^2}{2m} + U_{\text{Coul}}(\boldsymbol{r}) + U_{\text{xc}}(\boldsymbol{r}) + U_{\text{ext}}(\boldsymbol{r}) \right) \varphi_\alpha = \varepsilon_\alpha \varphi_\alpha \ , \tag{105}$$

$$U_{\text{xc}}(\boldsymbol{r}) = \frac{\delta E_{\text{xc}}(n(\boldsymbol{r}))}{\delta n(\boldsymbol{r})} \ , \tag{106}$$

where $\delta/\delta n(\boldsymbol{r})$ is the functional derivative. This is a nonlinear equation because the potentials depend themselves on the wavefunctions through the density (104). In that respect, the Kohn–Sham equations are similar to the Hartree–Fock equations, but simpler because only local potentials occur. The existence of a local-density representation is guaranteed by the Hohenberg–Kohn [84] and Kohn–Sham theorem [102]. The actual form of the exchange-correlation functional E_{xc}, however, can only be deduced in an approximate way. Most popular is the LDA whose construction is conceptually very simple and can be summarized as

$$E_{\text{xc}}(n(\boldsymbol{r})) = \int \text{d}^3 r \, n(\boldsymbol{r}) \varepsilon_{\text{xc}}(n(\boldsymbol{r})), \qquad \varepsilon_{\text{xc}}(n) = \frac{E_{\text{xc}}(n)}{N} \ . \tag{107}$$

In practice, one computes the binding energy E_{xc}/N of a homogeneous electron cloud at various fixed densities n, and transfers the result point by point independently to the actual local density $n(\boldsymbol{r})$. Key quantity is thus the exchange-correlation energy $\varepsilon_{\text{xc}}(n)$ to be obtained from a careful calculation of correlated electron matter. Early attempts employed just the RPA correlations [15]. Further electron–electron correlations in a Galitskij approach have been added in the widely used Ref. [69]. The very elaborate Green's function Monte Carlo calculations of [31] have been parametrized in the exchange-correlation functional of [180]. In any case, the Kohn–Sham equations with exchange-correlation functionals in LDA constitute a versatile and robust approach to mean-field calculations of inhomogeneous electron systems for which there exists an enormous body of applications in all fields of electron physics.

The success of this Kohn–Sham scheme in static applications suggests a naive and minimal extension to dynamical situations by using the time-dependent analogue of Eq. (105). This yields

the time-dependent LDA (TDLDA) with the basic equation

$$\left(\frac{\hat{p}^2}{2m} + U_{\text{Coul}}(\boldsymbol{r}, t) + U_{\text{xc}}(\boldsymbol{r}, t) + U_{\text{ext}}(\boldsymbol{r}, t)\right)\varphi_\alpha = i\hbar\partial_t\varphi_\alpha , \qquad (108)$$

where the exchange-correlation potential U_{xc} is again defined as in Eq. (106). TDLDA has been successfully applied, e.g., to compute the plasmon response of metal clusters [27,50] and applications are still showing up, nowadays even in the highly excited regime [29].

The TDLDA, consisting out of the dynamical Kohn–Sham equation (108) together with the instantaneous exchange-correlation potential (106), is not only local in coordinate space but also local in time because the U_{xc} refers to the density $n(\boldsymbol{r}, t)$ at the same instant in time as the wavefunctions φ_α. That may be very well justified for slow processes. But there may arise equally well situations where the time scale of the mean-field motion interferes with times for the correlation processes hidden in U_{xc}. An appropriate definition of U_{xc} should then include retardation effects, i.e. should recur also to the density $n(\boldsymbol{r}', t')$ at past times $t' \leq t$ and possibly other places $\boldsymbol{r}' \neq \boldsymbol{r}$. Such generalized concepts for a dynamical exchange-correlation potential have been much discussed over the past decades. The essence is that one can extend the definition of the exchange-correlation potential to become nonlocal in space and time, i.e.

$$U_{\text{xc}} = U_{\text{xc}}(\{n(\boldsymbol{r}', t'), t' \leq t\}) . \qquad (109)$$

The construction of such generalized effective potentials is very intricate because there are now further, dynamical, boundary conditions to be obeyed. There is, for example, the causality requirement $t' < t$. This inhibits a variational formulation in terms of an energy-density functional E_{xc} and subsequent functional derivatives. Modelling has thus to take place at the level of U_{xc} and a consistent definition of energy or related quantities needs to be constructed separately. Nonetheless, considerable progress has been made, particularly in recent years. For a detailed discussion of this wide and involved topic, we refer the reader to the review articles [66–68]. For our present purposes, it suffices to know that such generalized potentials (109) do exist.

A truly dynamical Kohn–Sham scheme has the same capabilities as the technique of the LFC discussed above. There are, in fact, close relations between the both schemes. These become obvious when linearizing the dynamical Kohn–Sham equations and expressing the results in terms of the response function χ. We skip the lengthy and straightforward derivation and just present the essentials. The density is split in the standard manner as $n(\boldsymbol{r}, t) = n + \delta n(\boldsymbol{r}, t)$ into stationary density and small dynamical perturbation. Variation with respect to δn thus introduces the exchange-correlation part of the residual interaction

$$V_{\text{xc}}(|\boldsymbol{r} - \boldsymbol{r}'|, t - t'; n) = \frac{\delta U_{\text{xc}}(\boldsymbol{r}, t)}{\delta n(\boldsymbol{r}', t')} . \qquad (110)$$

Switching to density-operator representation of the quantum state and subsequent linearization yields the response equations as

$$\chi(\boldsymbol{q}, \omega) = \frac{\chi_0(\boldsymbol{q}, \omega)}{1 - [V(\boldsymbol{q}) + V_{\text{xc}}(\boldsymbol{q}, \omega)]\chi_0(\boldsymbol{q}, \omega)} , \qquad (111)$$

where $V(\boldsymbol{q}) = e^2/\varepsilon_0 \boldsymbol{q}^2$ is the Coulomb potential as usual. The pure RPA consists in letting $V_{\mathrm{xc}} = 0$ in the above expression. The sum $V + V_{\mathrm{xc}}$ is thus the effective interaction for RPA calculations as derived from the dynamical Kohn–Sham scheme. It takes the same place as the $V(1 - G)$ in the definition (48) of the local field correction. We thus can identify

$$V_{\mathrm{xc}}(\boldsymbol{q}, \omega) = -V(\boldsymbol{q})G(\boldsymbol{q}, \omega) \ . \tag{112}$$

This expression shows that there is a simple one-to-one correspondence between the time-dependent Kohn–Sham scheme and the LFC, at least for homogeneous systems. The experience in designing LFC helps in the construction of U_{xc}, and vice versa, the experience with treating inhomogeneous systems can be carried over for extensions of LFC. This is what actually takes place in the present development of density functional theory [138].

The TDLDA is the most simple of these density-functional theories. It is not only local in coordinate space but also local in time because the potentials as defined in Eq. (108) refer to the same instant in time as the wavefunctions φ_α. Relating E_{xc} to its kernel $n\varepsilon_{\mathrm{xc}}(n)$ by Eq. (107) then yields the doubly local residual interaction

$$V_{\mathrm{xc}}^{\mathrm{LDA}}(|\boldsymbol{r} - \boldsymbol{r}'|, t - t') = \frac{\partial^2(n\varepsilon_{\mathrm{xc}}(n))}{\partial n^2}\delta(\boldsymbol{r} - \boldsymbol{r}')\delta(t - t') \tag{113}$$

with a most simple Fourier transform

$$V_{\mathrm{xc}}^{\mathrm{LDA}}(\boldsymbol{q}, \omega) = \frac{\partial^2(n\varepsilon_{\mathrm{xc}}(n))}{\partial n^2} = \mathrm{constant} \ .$$

As mentioned above, this simplistic approach suffices for many purposes, in particular for slow processes and weak spatial dependence, but it often succeeds if these slowness and softness conditions are not visibly met. As an example, remember the success of the static LFC which leads to locality in time, $V_{\mathrm{xc}} \propto \delta(t - t')$. In fact, a nonlocality in coordinate space can still be implemented into an energy-density functional in a fairly simple manner. One merely has to replace the local density dependence by a folded density dependence

$$E_{\mathrm{xc}}(n(\boldsymbol{r})) \ \rightarrow \ E_{\mathrm{xc}}(\tilde{n}(\boldsymbol{r})), \qquad \tilde{n}(\boldsymbol{r}) = \int \mathrm{d}^3 r' \, \mathscr{F}(\boldsymbol{r} - \boldsymbol{r}')n(\boldsymbol{r}') \tag{114}$$

and carry through the variational derivations as usual. The folding function $\mathscr{F}$ is related to the momentum structure of the LFC, or V_{xc}, simply as

$$\mathscr{F}^2(\boldsymbol{q}) \propto V_{\mathrm{xc}}(\boldsymbol{q}) \ .$$

Such an approach has been pursued, e.g. for an electron liquid [92] and in connection with ^{3}He systems where finite range effects are crucial already at a static level [183,184]. A similar folding approach for the time profile of the interaction cannot be so simple because a second functional derivative would deliver a residual interaction which is symmetric in time $t - t'$, in contradiction to the causality requirement $t' \leq t$.

3.3.6. Stopping power using LDA and TDLDA

The most demanding case comes with highly degenerate, $\Theta \ll 1$, and nonideal, $\xi \gtrsim 1$, targets. They require a fully quantal treatment and inclusion of correlations. But a detailed quantum

many-body calculation is even nowadays prohibitively complicated when spatial inhomogeneities are involved. Density functional methods as LDA and TDLDA offer a way out of this dilemma for moderately inhomogeneous systems in the nonlinear coupling regime. They allow to take up a great deal of correlations which have been computed extensively in homogeneous electron systems [32] and to carry them over to the inhomogeneous systems by means of an energy-density functional at the level of the local density approximation (LDA). Particularly simple is the static case with the ionic charge at rest for which successful LDA calculations for the nonlinear screening of a proton were performed [5]. The computation of the stopping power in these schemes employs the general results (59), or (58), respectively, obtained in the binary collision picture and expressed in terms of the transport cross section σ_{tr} and a shifted electron (Fermi) distribution [25,156]. For $\Theta = 0$ and $v \ll v_F$ the friction coefficient has been calculated using Eq. (60) for positively charged ions and antiprotons, see e.g. [49,126], and an application for the stopping power of an antiproton in the low velocity regime $v < v_F$ is found in the recent paper [190]. The transport cross section is evaluated with selfconsistent potential built around the ion due to the screening by the electronic scattering states. The electronic exchange-correlation effects in these selfconsistent calculations are computed in LDA. The calculations used the relation (59) which is restricted to spherical scattering potentials. It works well in the regime $v \lesssim v_F$ where deformations remain small. This encourages future work without restriction to spherical potentials, i.e. using expression (58) for general potentials instead of Eq. (59).

3.3.7. Nonlinear response at low ion velocities

An alternative access to the stopping power in the fully nonlinear regime and at low projectile velocities is provided by relating it to the force–force correlation function [47,48] which, in turn, can be computed by dynamical schemes as TDLDA, Vlasov–Poisson or simulation methods (see Sections 3.3.3 and 3.3.4). Starting point is the definition (B.1) of the stopping power taken in the limit of infinite projectile mass. The projectile then represents an external moving potential at position vt and the Hamilton operator is given by $\hat{H}'(t) = \hat{H}_0 - \theta(t)\sum_i e\phi_p(\hat{r}_i - vt)$. Here $\hat{H}_0$ accounts for the kinetic energy of the electrons and their mutual Coulomb interactions and $\sum_i e\phi_p(\hat{r}_i - vt)$ for their coupling to the external potential. One introduces the operator $\hat{F}$ for the component of the force along the direction of motion $\hat{F}(v,t) = e\sum_i (v/v) \cdot \nabla_{r_i}\phi_p(\hat{r}_i - vt)$ and considers the time average. This yields the stopping power as

$$\frac{dE}{ds}(\tau) = -\frac{1}{\tau}\int_0^\tau dt\, \langle \hat{F}(v,t)\rangle = -\frac{1}{\tau}\int_0^\tau dt\, \text{Tr}\,\hat{\rho}(t)\hat{F}(v,t)\,. \tag{115}$$

This is an exact result for constant ion velocities v, i.e. for $M \to \infty$, where dE/ds reaches a time independent value for times large compared to the initial transient period (typically $\sim \omega_p^{-1}$). In the limits $v \to 0$ and $\tau \to \infty$, the stopping power Eq. (115) can be expressed in terms of a force–force correlation function as [47,48]

$$\frac{dE}{ds}(\tau) \overset{v\to 0}{\propto} \frac{v}{2}\int_{-\infty}^\infty dt\, \langle \hat{F}(0)\hat{F}(t)\rangle = \frac{v}{2}\int_{-\infty}^\infty dt\, \text{Tr}\,\hat{\rho}_{eq}\hat{F}(0)\exp(i\hat{H}t/\hbar)\hat{F}(0)\exp(-i\hat{H}t/\hbar)\,, \tag{116}$$

where the force $\hat{F}(t=0)$ is taken at the origin $r = 0$. The density operator $\hat{\rho}_{eq}$ describes the equilibrium state of the fully correlated projectile–target system with the projectile at rest as defined

by the time independent Hamilton operator $\hat{H} = \hat{H}_0 - \sum_i e\phi_p(\hat{r}_i)$ and e.g. $\hat{\rho}_{eq} = \exp(-\beta\hat{H})/\text{Tr}\exp(-\beta\hat{H})$. Note that the stopping power depends linearly on the velocity v as it should be in the regime of small velocities. The factor next to v is the friction coefficient of the system. The result (116) thus relates the friction coefficient to the force–force correlation function at equilibrium. This allows to recur to any theoretical method which is appropriate to describe the equilibrium properties of the ion–target system without restrictions on the projectile–target coupling, degeneracy, ideality, or other state conditions. This offers an alternative access to the stopping at low velocities where the strongest nonlinearity effects are expected.

The relation (116) holds under very general conditions. Nonetheless, it is interesting to look at the regime of linear response and to see how the known results in that regime are recovered. The connection is established by neglecting the ion–target coupling in the equilibrium dynamics of the target, i.e. $\hat{H} \to \hat{H}_0$ and $\hat{\rho}_{eq} \to \hat{\rho}_0 = \exp(-\beta\hat{H}_0)/\text{Tr}\exp(-\beta\hat{H}_0)$. Now $\text{Tr}\,\hat{\rho}_0\ldots$ only accounts for the unperturbed electron system and with a Fourier representation of $\hat{F}$ the correlation function becomes

$$\int_{-\infty}^{\infty} dt\,\langle\hat{F}(0)\hat{F}(t)\rangle \to \int_{-\infty}^{\infty} dt\,\text{Tr}\,\hat{\rho}_0\hat{F}(0)\hat{F}(t) \propto \int d^3k\,|F(\boldsymbol{k})|^2 \int_{-\infty}^{\infty} dt\,\text{Tr}\,\hat{\rho}_0\hat{n}(\boldsymbol{k},t)\hat{n}(-\boldsymbol{k},0)$$

$$\propto \int d^3k\,|F(\boldsymbol{k})|^2 S(k,\omega=0)\,, \tag{117}$$

using the definition of the dynamical structure factor Eq. (32). Inserting expression (117) into Eq. (116), connecting $S(k,\omega)$ to $\varepsilon(k,\omega)$ via relation (34) and replacing $F(\boldsymbol{k})$ by the derivative of the ion potential $F(\boldsymbol{k}) = i\hat{\boldsymbol{v}}\cdot\boldsymbol{k}e\phi_p(\boldsymbol{k})$ directly leads to the linear response result for low ion velocities Eqs. (42) and (43).

3.4. Overview

Table 1 summarizes the presentation of methods in keywords sorted in tabular form. The presentation is, hopefully, self-explanatory. Nonetheless, a few more remarks are in order. There are basically two opposite approaches to the problem: On the one hand, the continuum approach formulated in terms of the dielectric constant $\varepsilon(k,\omega)$, and on the other hand, the particle aspects pronounced in the binary collision approaches. These both classes provide complementary points of view. The collisional approaches motivate appropriate cutoffs in the dielectric formulation or provide more sophisticated correction terms for the linear response approach whereas the dielectric linear response approach gives the appropriate screening for computing the effective cross sections. The more elaborate the treatment, the more does it contain from both aspects. And the most complete theories, as e.g. MD simulations or WPMD, finally contain each side with equal weight.

Before closing this section, we ought to mention that there exist a few more approaches which we have not reviewed here. For linear coupling and ideal or moderately nonideal plasmas a Fokker–Planck equation can be used as starting point [110]. A more general approach is provided by (quantum) kinetic theory [61,103,172], which allows successive improvement by incorporating various levels of approximations for the used collision integrals. The usually employed Lenard–Balescu or Boltzmann collision integrals are designed to describe stopping at linear and

Table 1
Summary of the methods sorted according to the appropriate regime of application

Ion–target coupling		Target conditions	
		Ideal $\xi \ll 1$	Nonideal $\xi \gtrsim 1$
$\langle \eta_p \rangle \ll 1$	Linear	Linear response description, any Θ, $\langle \eta_e \rangle$ $\varepsilon(k, \omega)$ from RPA	$\varepsilon(k, \omega)$ from RPA & LFC
$\langle \eta_p \rangle \gtrsim 1$	Semilinear $r_c/\lambda \ll 1$	Effective $\frac{d\sigma}{d\Omega}$ with screening from $\varepsilon(k, \omega)$ Binary collisions	With cutoff from binary collisions Combined expression $(dE/ds)_{\text{com}}$
	Nonlinear $r_c/\lambda \gtrsim 1$	Vlasov for $\Theta \gg 1$, $\langle \eta_e \rangle \gg 1$ fermionic Vlasov for any Θ, $\langle \eta_e \rangle \gg 1$	Effective $\frac{d\sigma}{d\Omega}$ from LDA low v, $\Theta = 0$, any $\langle \eta_e \rangle$ MD for $\Theta \gg 1$, $\langle \eta_e \rangle \gg 1$ WPMD for $\Theta \lesssim 1$, any $\langle \eta_e \rangle$ TDLDA for $\Theta \ll 1$, any $\langle \eta_e \rangle$ force–force correlation, low v, any Θ, $\langle \eta_e \rangle$

semilinear coupling in ideal targets. Non-Markovian extensions include higher correlations which provide access to nonideal targets. Finally hydrodynamic descriptions have been used to determine the energy loss [35]. Their validity is a question of time-scales rather then coupling strengths: a hydrodynamic approach is suitable whenever the relaxation times are fast enough such that the ion–target system is in local equilibrium.

Furthermore, our presentation and the classification is biased on one-component plasmas, although more general cases are discussed occasionally. The theories for plasmas with two or more

components are complicated by new conditions and regimes showing up. A thorough discussion of these aspects goes beyond the scope of the present review.

4. Nonlinear stopping in classical plasmas

This section is dedicated to the presentation and discussion of the nonlinear stopping power in classical systems studied by numerical methods as MD-simulations (Section 3.3.3) or by solving the Vlasov–Poisson equations (Section 3.3.1).

4.1. Electronic stopping in classical plasmas

Before presenting and discussing the results, we want to specialize several important relations to the classical case as discussed here. This serves to define key quantities for the subsequent discussions. The basic scenario throughout this section is a completely classical system with classical ion–electron collisions $\langle\eta_p\rangle \gg 1$, see Eq. (16), nondegenerate targets $\Theta \gg 1$, see Eq. (12), and classical electron–electron collisions, $\langle\eta_e\rangle \gg 1$, see Eq. (14). The singularity of the Coulomb potential will not be removed by quantum effects and the projectile represents always a strong perturbation on the electrons for sufficiently small distances. According to the classification scheme for the ion–target coupling, Section 2.3, the regime of linear coupling is essentially related to quantum effects and does not exist for a classical ion–target system. There we can deal only with semilinear and nonlinear coupling. Hence, the weak coupling limit for a classical system is the semilinear regime and any discussion of nonlinear features in ion stopping has to be compared with the behavior of stopping at semilinear coupling as reference point. The decisive parameter to characterize the (non)linearity is thus the demarcation between semilinear and nonlinear coupling in classical targets, as defined in Eq. (25),

$$\frac{\langle b_0\rangle}{\lambda} = \frac{\sqrt{3}|Z|\Gamma^{3/2}}{(1 + (v/v_{\text{th}})^2)^{3/2}} = \frac{|Z|}{3N_{\text{D}}}\frac{1}{(1 + (v/v_{\text{th}})^2)^{3/2}} \ . \tag{118}$$

Classical weak coupling, i.e. the semilinear coupling regime, is given for $\langle b_0\rangle/\lambda \ll 1$, and strong coupling, of course, in the opposite case. No length scale exists for classical Coulomb systems and thus the dynamics of the ion–target system is completely characterized by Γ and Z. This can be seen easily after rescaling the equations of motion, as demonstrated in the Appendices A.1 and A.2.

The stopping power for the classical weak coupling regime has to be deduced from the approximations discussed in context with the semilinear regime like linear response with cutoffs (Section 3.2.2), the combined scheme of Section 3.2.3, or binary collisions with effective screening length (Section 3.2.2). We start with discussing the stopping power in the binary collision picture as outlined in Section 3.2.1. The stopping power for spherical symmetric potentials, Eq. (59), can be rewritten in dimensionless form using for classical systems as natural units for time, velocity, length and energy, the inverse of the plasma frequency, the thermal velocity, the Debye length and the thermal energy, respectively (see Eq. (A.1)). Furthermore, we employ the relations $\Gamma^{-3/2} = 4\pi\sqrt{3}n\lambda_{\text{D}}^3$, $\lambda_{\text{D}}^2 = \varepsilon_0 k_{\text{B}}T/e^2 n$ and $e^2/\varepsilon_0 = 4\pi\sqrt{3}\Gamma^{3/2}k_{\text{B}}T\lambda_{\text{D}}$. After replacing the Fermi distribution $f_0(p)$ by the Maxwell distribution $f_0(v_e) = (m/2\pi k_{\text{B}}T)^{3/2}\exp(-mv_e^2/2k_{\text{B}}T)$ the dimensionless

binary collision stopping power resulting from Eq. (59) reads

$$\frac{dE}{ds}\frac{\lambda_D}{k_B T} = \frac{\sqrt{3}}{\Gamma^{3/2}}\int\frac{d^3 v_r}{(2\pi)^{3/2} v_{th}^3}\exp\left(-\frac{(\boldsymbol{v}_r + \boldsymbol{v})^2}{2 v_{th}^2}\right)\frac{v_r}{v_{th}}\frac{\hat{\boldsymbol{v}}\cdot\boldsymbol{v}_r}{v_{th}}\frac{\sigma_{tr}(v_r)}{12\pi\lambda_D^2}.$$
(119)

It reduces in the limit of high velocities (see Eq. (61)) to the compact expression

$$\frac{dE}{ds}\frac{\lambda_D}{k_B T} = \frac{\sqrt{3}}{\Gamma^{3/2}}\left(\frac{v}{v_{th}}\right)^2\frac{\sigma_{tr}(v)}{12\pi\lambda_D^2}, \quad v \gg v_{th}.$$
(120)

In the limit of low velocities the stopping power becomes $\propto v$ and can thus be parametrized in terms of a dimensionless friction coefficient $R(Z,\Gamma)$ as

$$\frac{dE}{ds}\frac{\lambda_D}{k_B T} = -\frac{\sqrt{3}}{\Gamma^{3/2}}\left(\frac{v}{v_{th}}\right)R(Z,\Gamma), \quad v \ll v_{th}.$$
(121)

In case of the binary collision stopping power (119) this friction coefficient is

$$R(Z,\Gamma) = \frac{4\pi}{3}\int_0^\infty\frac{dv_e v_e^5}{(2\pi)^{3/2} v_{th}^6}\exp\left(-\frac{v_e^2}{2 v_{th}^2}\right)\frac{\sigma_{tr}(v_e)}{12\pi\lambda_D^2},$$
(122)

and represents together with definition (121) the scaled version of the general result (60), now applied to classical systems.

The binary collision description is, of course, incomplete as long as the transport cross section σ_{tr} is not specified. It has to be computed from an effective projectile–electron interaction. A suitable and very common choice is the Yukawa-like shielded Coulomb interaction

$$V_p(r) = -\frac{Ze^2}{4\pi\varepsilon_0 r}\exp\left(-\frac{r}{\lambda}\right) = -k_B T\frac{\sqrt{3}Z\Gamma^{3/2}}{r/\lambda_D}\exp\left(-\frac{r}{\lambda}\right).$$
(123)

Here, the screening length λ enters as an external parameter and may depend on the projectile velocity v which itself is an external parameter and not a dynamical variable of the projectile–target system in the considered limit of infinitely massive projectiles. In the classical description, the related transport cross section

$$\sigma_{tr}(v_r) = 2\pi\int_{-1}^1 d\cos(\vartheta)[1 - \cos(\vartheta)]\frac{d\sigma(v_r,\vartheta)}{d\Omega} = 2\pi\int_0^\infty db\, b[1 - \cos(\vartheta(b))]$$
(124)

is defined in terms of the classical mechanics relation between the center-of-mass scattering angle ϑ and the impact parameter b ([62], chapter 3)

$$\vartheta(b) = \pi - 2b\int_{r_m}^\infty\frac{dr}{r^2}\left[1 - \frac{V_p(r)}{E} - \frac{b^2}{r^2}\right]^{-1/2}, \quad\text{where } 1 - \frac{V_p(r_m)}{E} - \frac{b^2}{r_m^2} = 0$$
(125)

and $E = \mu v_r^2/2 \approx m v_r^2/2$ is the relative kinetic energy. The transport cross section given by the integrals (124) and (125) must in general be found numerically. For $\eta_p \gg 1$ and $\lambdabar_r/\lambda \ll 1$, as granted in the classical limit, the cross section obtained from Eqs. (124) and (125) completely agrees with the

fully quantum mechanical σ_{tr} calculated from a numerical solution of the stationary Schrödinger equation with the scattering potential (123) and a subsequent phase shift analysis [120]. An approximate analytical expression exists for high energies ($E = mv_r^2/2 \gg |Ze^2/4\pi\varepsilon_0\lambda|$ [107]. Furthermore a fit formula is available which is valid up to $|Ze^2/4\pi\varepsilon_0\lambda E| \approx 3$ for negatively charged projectiles $Z < 0$ [131]. An inspection of the expressions (123)–(125) in terms of scaled quantities (A.1) shows that the transport cross section depends on v_r/v_{th}, $Z\Gamma^{3/2}$, and λ/λ_D. In particular, it is function of the sign of the ion charge at variance with the linear response approach which depends on $|Z|$ only. The difference in the binary collision stopping power for different signs of Z is, however, only important for nonlinear coupling $|Z|\Gamma^{3/2} \gtrsim 1$ while it is unimportant in the truly semilinear regime ($|Z|\Gamma^{3/2} \ll 1$) where the binary collision treatment is used to provide corrections to the linear response description as outlined in Sections 3.2.2 – 3.2.4. The first of these approximations, the correction by cutoffs, will be discussed now.

Using the classical scaling parameters (A.1), the linear response stopping result with cutoff, Eq. (65), takes the dimensionless form

$$\frac{dE}{ds}\frac{\lambda_D}{k_B T} = Z^2\sqrt{3}\Gamma^{3/2}g\left(k_m, \frac{v}{v_{th}}\right),$$

$$g\left(k_m, \frac{v}{v_{th}}\right) = \frac{\lambda_D^2}{2\pi^2}\int_{k<k_m} d^3k\, \frac{\boldsymbol{k}\cdot\hat{\boldsymbol{v}}}{k^2}\mathrm{Im}\left[\frac{1}{\varepsilon_{cl}(k, \boldsymbol{k}\cdot\boldsymbol{v})}\right], \tag{126}$$

where the RPA dielectric function ε_R (47) and the cutoff k_m (68) are replaced by their classical limits ε_{cl} (78) and

$$k_m = \frac{2}{\gamma\langle b_0\rangle} = \frac{1}{\lambda_D}\frac{2}{\gamma\sqrt{3}|Z|\Gamma^{3/2}}\left(1 + \frac{v^2}{v_{th}^2}\right), \tag{127}$$

respectively. The dimensionless function $g(k_m, v/v_{th})$ depends only on the quantities $|Z|\Gamma^{3/2}$ and v/v_{th}. It neither depends on Z and Γ separately nor on the sign of the ion charge.

The high velocity limit of the stopping power (126) reads

$$\frac{dE}{ds}\frac{\lambda_D}{k_B T} \sim -Z^2\sqrt{3}\Gamma^{3/2}\left(\frac{v_{th}}{v}\right)^2\ln\left[\frac{2}{\gamma\sqrt{3}|Z|\Gamma^{3/2}}\left(\frac{v}{v_{th}}\right)^3\right], \quad v \gg v_{th}, \tag{128}$$

and represents Eq. (74) rewritten in terms of the dimensionless system parameters Γ, Z, and v/v_{th}. At low velocities, the friction coefficient R (121) deduced from the classical linear response stopping power with cutoff k_m, expression (126) is a function only of the combination $|Z|\Gamma^{3/2}$ and takes the form [3,135,194]

$$R(|Z|\Gamma^{3/2}) = \frac{(Z\Gamma^{3/2})^2}{3\sqrt{2\pi}}\left[\ln(k_m^2\lambda_D^2 + 1) - \frac{k_m^2\lambda_D^2}{k_m^2\lambda_D^2 + 1}\right] \overset{k_m \gg 1}{=} \frac{2(Z\Gamma^{3/2})^2}{3\sqrt{2\pi}}\left\{\ln\left[\frac{2}{\gamma\sqrt{3}|Z|\Gamma^{3/2}}\right] - \frac{1}{2}\right\}. \tag{129}$$

The last step is justified because we have $k_m \gg 1$ in the semilinear coupling regime ($|Z|\Gamma^{3/2} \ll 1$) at low velocities. The classical friction coefficient R (129) replaces the general friction coefficient

$\tilde{C}(\xi, \Theta, |Z|)$ which was defined in Eq. (72) and which carries the full dependencies for arbitrary target conditions.

To establish next the classical limit of the combined expression $(dE/ds)_{com}$, Eq. (69), some additional considerations are necessary. We start with the statically screened interaction written in terms of the classical scaling parameters

$$V_p(k) = -4\pi k_B T \lambda_D \sqrt{Z\Gamma^{3/2}k^2 + 1/\lambda^2} \tag{130}$$

which corresponds for $\lambda = \lambda_D$ to the general expression (70) when replacing the RPA dielectric function $\varepsilon_R(k,0)$ (47) with its classical limit $\varepsilon_{cl}(k,0)$ (78). Simultaneously, $V_p(k)$ (130) represents the Fourier transform of the screened scattering potential (123) for arbitrary λ used in the binary collision stopping power. The binary collision contribution $(dE/ds)_{bc}$ which enters into the combined stopping power (69) is thus directly given by Eq. (119) using V_p Eq. (130) or Eq. (123). However, the two first order Born stopping powers, $(dE/ds)_{BI}^{sta}$ and $(dE/ds)_{BI}^{dyn}$, for the statically screened potential (130) and the dynamically screened counterpart

$$V_p(k) = -4\pi k_B T \lambda_D \frac{\sqrt{3}Z\Gamma^{3/2}}{k^2 \varepsilon_{cl}(k, \omega = \boldsymbol{k}\cdot\boldsymbol{v})},$$

respectively, do not exist in the classical limit as discussed at the end of Section 3.2.2. A way out is given by calculating the difference $(dE/ds)_{BI}^{dyn} - (dE/ds)_{BI}^{sta}$ and not each contribution separately. This cures the problems of the classical description related to its invalid predictions for high transferred momenta k, since the statically and dynamically screened potentials become identical for high k and cancel out. In dimensionless form and using the classical scaling the difference of the linear response contributions which enter $(dE/ds)_{com}$ reads

$$\left\{ \left(\frac{dE}{ds}\right)_{BI}^{dyn} - \left(\frac{dE}{ds}\right)_{BI}^{sta} \right\} \frac{\lambda_D}{k_B T} = -Z^2 \sqrt{3}\Gamma^{3/2} g_{ds}\left(\lambda, \frac{v}{v_{th}}\right),$$

$$g_{ds}\left(\lambda, \frac{v}{v_{th}}\right) = \frac{\lambda_D^2}{2\pi^2} \int d^3k \frac{\boldsymbol{k}\cdot\hat{\boldsymbol{v}}}{k^2} \left\{ \frac{\text{Im}\left[\varepsilon_{cl}(k, \boldsymbol{k}\cdot\boldsymbol{v})\right]}{|\varepsilon_{cl}(k, \boldsymbol{k}\cdot\boldsymbol{v})|^2} - \frac{\text{Im}\left[\varepsilon_{cl}(k, \boldsymbol{k}\cdot\boldsymbol{v})\right]}{|1 + 1/(k\lambda)^2|^2} \right\}. \tag{131}$$

Hence, the sum of the linear response term (131) and the binary collision stopping power (119), when using the statically screened interaction (123), (130) with λ equal the Debye length λ_D, represents the classical version of the combined expression (69) presented in Section 3.2.3.

To finish this discussion of the several approximations for semilinear stopping in the classical case we turn now to the binary collision stopping with velocity dependent screening length as sketched in Section 3.2.4. There, the dynamical polarization effects are taken into account in an approximative manner by parametrizing them in terms of a velocity dependent screening length, that is, calculating the stopping power from expressions (119) and (123) with $\lambda = \lambda(v)$ as function of the projectile velocity v. It remains, however, to find an appropriate function $\lambda(v)$ to complete this phenomenological approach and various choices of $\lambda(v)$ can be considered. Here, we propose to demand equal linear response stopping powers for dynamically screened and effective, velocity

dependent interactions. Then, the screening length $\lambda(v)$ is defined implicitly using this difference, Eq. (131), by

$$g_{ds}\left(\lambda\left(\frac{v}{v_{th}}\right), \frac{v}{v_{th}}\right) = 0 \; , \tag{132}$$

which has to be resolved numerically for $\lambda(v/v_{th})$.

4.2. Nonlinear stopping power of heavy ions

We now discuss the results from a large number of MD and test-particle simulations reported in [191–197,199–202] and compare it with recent experimental [170,185–188] as well as other theoretical results [23,38]. The common important observation is that the stopping power in the regime of nonlinear ion–target coupling depends on the ion charge as Z^x, with $x \sim 1.5$. This is clearly different from the $Z^2 \ln(\text{const.}/|Z|)$-behavior in the semilinear coupling regime, see Eq. (129). This reduced growth with Z in the nonlinear regime is connected with a charge dependence of the screening length.

4.2.1. Velocity dependence

Figs. 3 and 4 show the stopping power dE/ds as function of the ion velocity v. The stopping power dE/ds is normalized by division through Z^2 and scaled in units of $3^{1/2}\Gamma^{3/2}k_B T/\lambda_D$ as suggested by the linear response expressions Eqs. (126)–(129). The ion velocity v is scaled in units of the thermal velocity $v_{th} = (k_B T/m)^{1/2}$. For graphic reasons we split up the forthcoming considerations into two parts. We start with a comparison of the different theoretical expressions for the stopping power in the semilinear regime as described in the previous section. This serves as reference for the following presentation and discussion of the simulation results.

The solid curves in Fig. 3 represent the combined expression $(dE/ds)_{com}$ given by the sum of the linear response term (131) and the binary collision stopping power (119) for a statically screened interaction (123) with $\lambda = \lambda_D$. The dotted curves show the linear response stopping power (126) with cutoff (127) while the dash-dotted curves are the results from the binary collision expression (119) with the velocity dependent screening length $\lambda(v)$ provided from Eq. (132). In all cases a positively charged ion is considered. For the lowest displayed coupling strength $Z\Gamma^{3/2} = 0.11$ where we are within the semilinear regime for all velocities the combined expression and the binary collision stopping power with velocity dependent screening are almost identical except of a small deviation around the maximum of the stopping power. This deviation vanishes quickly for still smaller coupling. The linear response result with cutoff exhibits higher stopping powers at medium velocities, is rather close to the other approaches but a bit lower at low velocities and agrees with them for high velocities. This is simply a consequence of the approximative derivation of the cutoff k_m, see Section 3.2.2, which is best substantiated for large k_m, that is, for high projectile velocities and/or for decreasing coupling parameter. In fact, the difference further diminishes for still smaller $|Z|\Gamma^{3/2}$. For increasing coupling strength, i.e. when proceeding towards and into the nonlinear regime, increasing deviations develop between the three descriptions. At $Z\Gamma^{3/2} = 0.36$ we are at the fringe to the nonlinear regime at low ion velocities, but well within semilinear regime for higher velocities while for the highest shown coupling strength $Z\Gamma^{3/2} = 11.2$ nonlinear coupling is
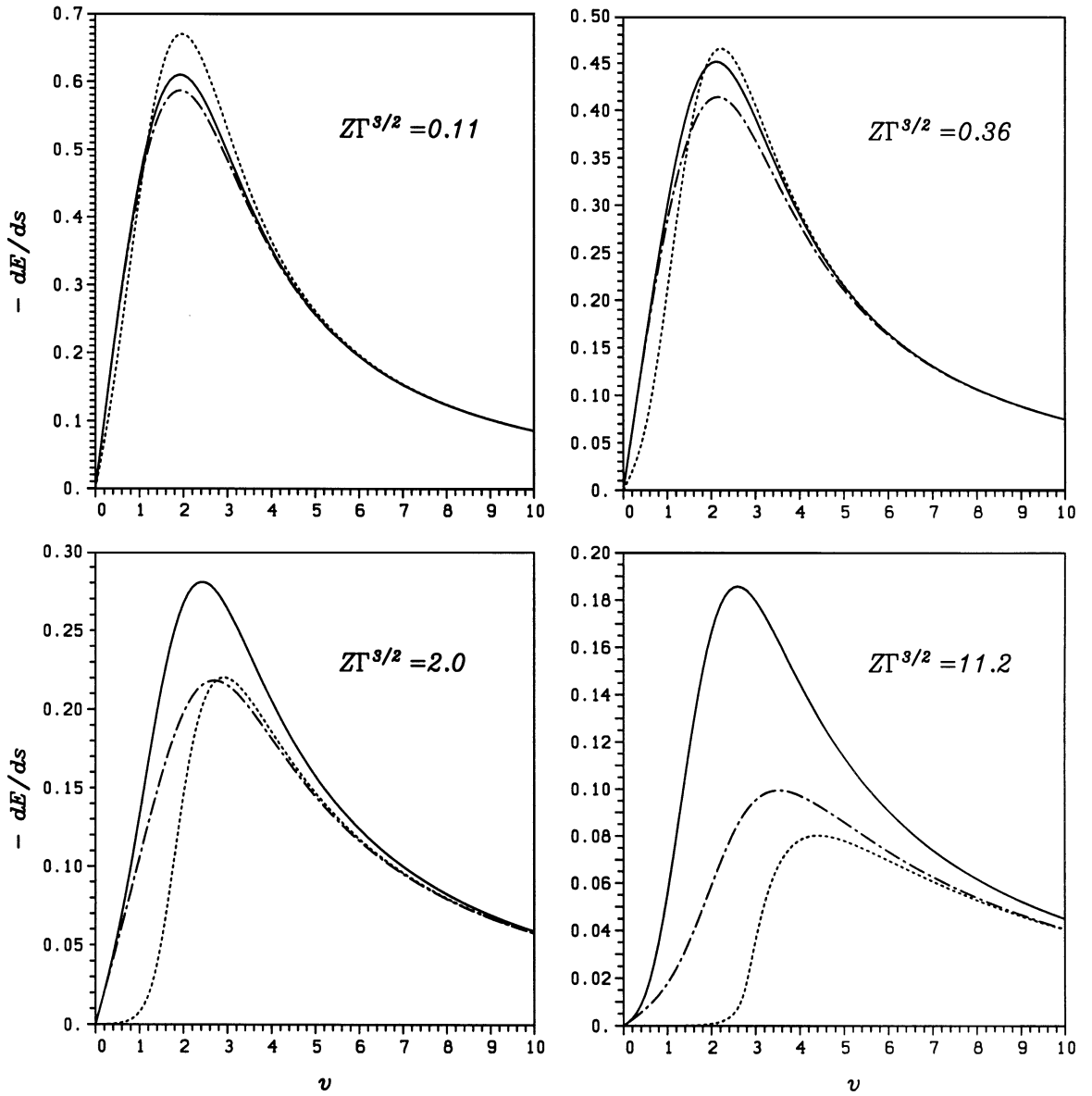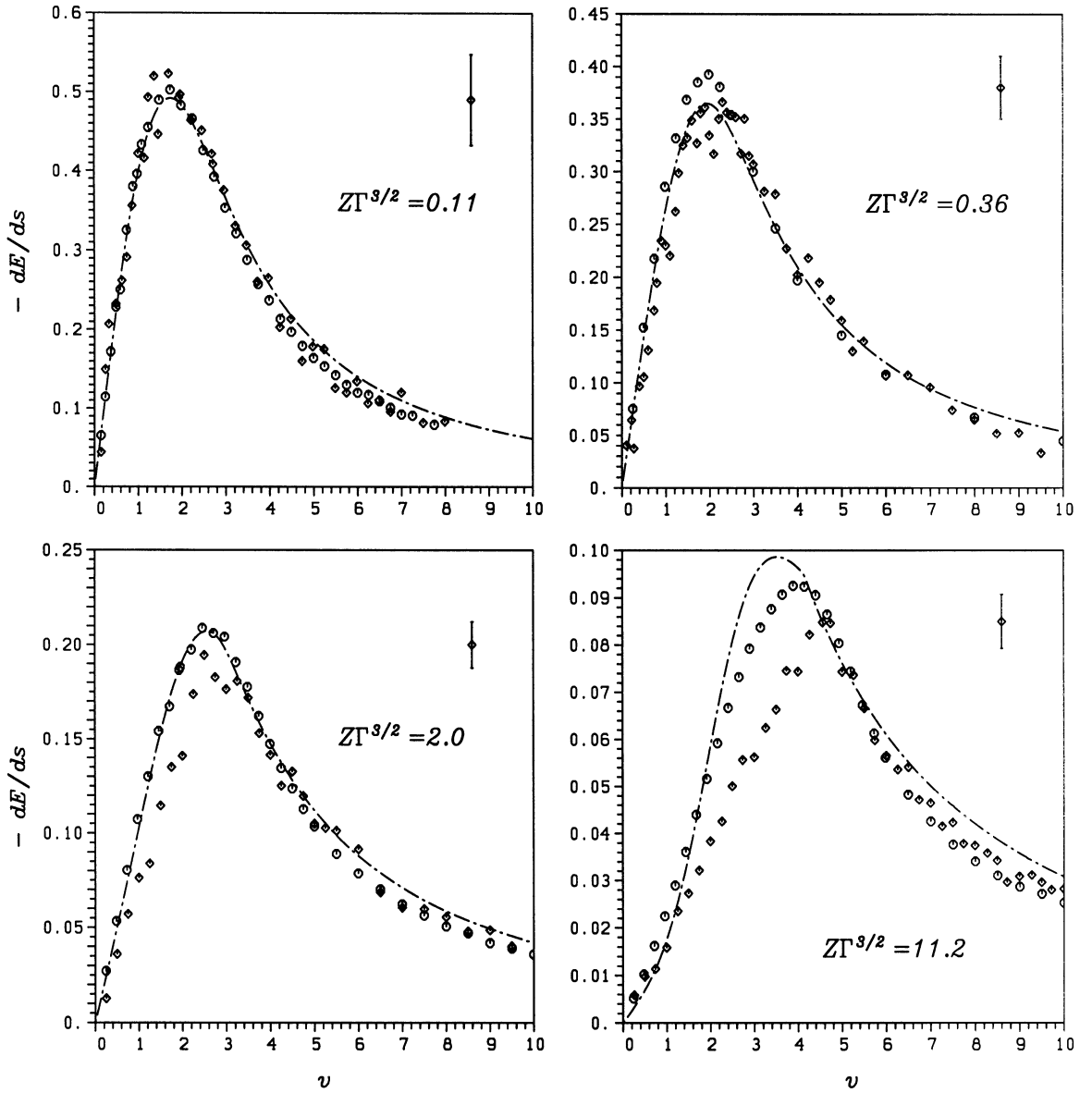
Fig. 3. Normalized stopping power $dE/ds/Z^2$ in units of $3^{1/2}\Gamma^{3/2}k_BT/\lambda_D$ as function of the ion velocity v in units of the thermal velocity $v_{th} = (k_BT/m)^{1/2}$ for a positively charged ion at various $Z\Gamma^{3/2}$. The solid curves represent the combined expression, composed from Eq. (131) and Eq. (119) with interaction (123) and $\lambda = \lambda_D$. The dotted curves are the linear response stopping power (126) with cutoff (127) while the dash-dotted curves exhibit the binary collision result (119) with the velocity dependent screening length $\lambda(v)$ from Eq. (132).

expected for $v < 2.5v_{th}$ if we assume $3^{1/2}|Z|\Gamma^{3/2}/(1 + v^2/v_{th}^2)^{3/2} = 1$ as the division line between semilinear and nonlinear coupling. At medium velocities the binary collision approximation with velocity dependent screening (dash-dotted) stays always below the combined expression (solid)

Fig. 4. Normalized stopping power $dE/ds/Z^2$ in units of $3^{1/2}\Gamma^{3/2}k_B T/\lambda_D$ as function of the ion velocity v in units of the thermal velocity $v_{th} = (k_B T/m)^{1/2}$ for $Z\Gamma^{3/2} = 0.11, 0.36, 2$ and 11.2 corresponding to a fixed ion charge state $Z = 10$ and plasma parameters $\Gamma = 0.05, 0.11, 0.34$ and 1.08, respectively. The diamonds are results of MD-simulations, the circles of Vlasov (PIC/test-particle) simulations. The errorbars for the MD results are suppressed for reasons of clearness, their typical size is indicated right top. For the test-particle simulations the errors are of the same size as the symbols. The dash-dotted curves shows the binary collision result with velocity dependent screening length, see Fig. 3, here corrected for the actual size of the simulation box as explained in the text.

with an increasing deviation for growing $Z\Gamma^{3/2}$, whereas both approaches agree in all cases at low and sufficiently high velocities. At sufficiently high velocities they also meet the linear response description with cutoff (dotted curves), which, however, considerably deviates at low velocities and for increasing coupling where it exhibits a drastically smaller stopping power. Its apparent cubic behavior at low velocities for $Z\Gamma^{3/2} = 2$ and 11.2 is deceiving insofar as there exists a non-vanishing linear term, however very small. This can be easily read of from the friction coefficient Eq. (129), which decreases $R \propto k_m^4$ for small k_m (127). We remind however, that the assumption of large k_m was essential for establishing the correction of the linear response stopping power by cutoffs, see Section 3.2.2. Agreement with the other approaches could be achieved of course by treating k_m in Eq. (126) as a free, velocity dependent fit function.

The results of the stopping power dE/ds as function of the ion velocity v obtained from the simulation studies are shown in Fig. 4 for coupling strengths $Z\Gamma^{3/2} = 0.11$, 0.36, 2 and 11.2 corresponding here to a fixed ion charge state $Z = 10$ and plasma parameters $\Gamma = 0.05$, 0.11, 0.34 and 1.08 of the electron target. The diamonds are results of MD-simulations. The typical size of the errors is indicated by the errorbar right top. These errorbars are related to an ensemble averaging over different microscopic initial configurations. They represent as a conservative estimate the standard deviations and not the (smaller) mean error of the mean, see Appendix A.1. The circles represent the results from test-particle simulations of the Vlasov equation. Here the large number of test particles, which are used to represent a smooth charge density, considerably reduces the fluctuations and the errorbars are of the order of the size of the symbols. As reference for comparison with the theoretical approaches of Fig. 3 we chose the predictions of the binary collision treatment (119) with the velocity dependent screening length from Eq. (132) which is shown as dash-dotted curves. It is to be remarked however, that the MD and test-particle simulations are inapplicable at high velocities because the screening length increases and becomes larger than the finite length L of the simulation box. To allow nevertheless some comparison at high v, one can imitate the finite simulation box in all the theoretical predictions by excluding stopping contributions which are originated only large wave length excitations. Compared to Fig. 3 where an infinitely extended target was assumed the dash-dotted curves in Fig. 4, corresponding to the binary collision model with velocity dependent screening length, are thus modified by subtracting the linear response stopping power related to k values smaller than $2\pi/L$, that is, by subtracting the correction term $(dE/ds)_{corr}\lambda_D/k_B T = Z^2\sqrt{3}\Gamma^{3/2}g(k_{min} = 2\pi/L, v/v_{th})$, Eq. (126). Due to the relation between the screening length and the plasma parameter Γ, see Section A.1, Eq. (A.3), this correction becomes significant only at high ion velocities $v \gg v_{th}$ for larger Γ, but already at $v \geq v_{th}$ for $\Gamma = 0.05$. For a given coupling strength the same change by $(dE/ds)_{corr}$ would apply as well for the further approaches discussed in Fig. 3. The deviations among them remain thus unaffected by this finite box size correction. The problem of the finite box size, however, together with a growth of the fluctuations with decreasing $|Z|\Gamma^{3/2}$ inhibits an application of the simulation techniques at much smaller coupling and more ideal targets as presented here.

When comparing now the simulation results with the simpler models one has to keep in mind that the nonlinearity of the coupling is treated by both MD and Vlasov simulations while only the MD simulations can deal with nonideal targets. In the Vlasov simulations as well as in the discussed theoretical approaches for semilinear coupling the target is an ideal electron plasma. A comparison of the results from MD with those from the Vlasov propagation thus reveals the influence of the nonideality of the target while we have to compare the simpler models with the

Vlasov simulations (circles) for judging on their range of validity. For the lowest coupling strength $Z\Gamma^{3/2} = 0.11$, Fig. 4, the binary collision model with velocity dependent screening (dash-dotted curve) agrees well with the Vlasov results (circles) within the errors. These are of the same order as the difference between the binary collision model and the combined expression, see Fig. 3. Thus both approaches are in very good agreement with the simulation results while the linear response result with cutoff, on the other hand, shows too large stopping values around the stopping maximum. For increasing $Z\Gamma^{3/2} = 0.36$ the binary collision treatment reproduces well the Vlasov results at high and low velocities but underestimates the stopping power for medium velocities where dE/ds reaches its maximum. There is, however, almost perfect agreement with the combined expression which provides a bit higher values at medium velocities as can be seen from the difference of the solid and the dash-dotted curve in Fig. 3. The linear response result with cutoff, on the other hand, becomes already rather unreliable except for large v. At still larger coupling $Z\Gamma^{3/2} = 2$ the binary collision stopping excellently fits the simulation results while the combined expression would predict around 30% to large values at the stopping power maximum. For the largest coupling strength $Z\Gamma^{3/2} = 11.2$ where the low velocities lie well within the nonlinear regime the binary collision treatment still reproduces satisfyingly the typical dimension of the stopping power at medium velocities but clearly underestimates it at low velocities. Here, the simulation results (MD and Vlasov) exhibit a much more pronounced linear increase in v which extends up to higher velocities, in the MD simulation (diamonds) practically up to the stopping maximum. At this high coupling the combined expression grossly overestimates the stopping power by a factor ≈ 2. From this we can conclude that the combined expression, Eq. (69), which can be considered as the theoretically best founded treatment works well up to a coupling parameter $Z\Gamma^{3/2} \lesssim 1$ in agreement with the definition of the semilinear coupling regime for which it was designed. For large coupling, more precisely in the range $Z\Gamma^{3/2} \approx 1$–5, the more phenomenological binary collision treatment with velocity dependent screening length yields a much better prediction for the stopping power. For even larger coupling all discussed approximations fail.

The effects of the nonideality of the target are revealed by comparing the results from MD with those from the Vlasov simulations, because collisions between the electrons are included in the full MD-simulation but are excluded in the mean-field description. There is good agreement for the smallest plasma parameter $\Gamma = 0.05$, see Fig. 4 for $Z\Gamma^{3/2} = 0.11$. For the next higher $\Gamma = 0.11$ some deviations begin to appear at low velocities and are clearly visible around the stopping power maximum. With increasing nonideality of the target $\Gamma = 0.34$ and $\Gamma = 1.08$ this trend proceeds and a more and more pronounced difference develops at low velocities up to the velocity where the stopping is maximal. This clearly indicates an influence of the nonideality of the target plasma, which tends to reduce the nonlinear stopping power at low and medium velocities. The high velocity stopping remains unaffected. This influence of the nonideality of the plasma has been investigated for a large number of simulations at various Z and Γ. They allow to conclude that nonideal effects start to appear at $\Gamma \gtrsim 0.1$. All these simulations show the appropriate linear increase of the stopping power with v at low v almost up to the maximum of dE/ds at $v \gtrsim v_{th}$. The position of the maximum shifts towards higher velocities with increasing coupling $|Z|\Gamma^{3/2}$ as it is the case also in the simpler models, Fig. 3. But a simple functional dependence of this shift on $Z\Gamma^{3/2}$ cannot be detected. In view of the linear increase of dE/ds at low v, the discussion of nonlinear stopping can be restricted to an investigation of the friction coefficient $R(Z, \Gamma)$, as defined in Eq. (121). We remark, that a similar linear increase up to $v \approx v_F$ was also found for nonlinear

stopping in the completely different target regime of fully degenerate electrons [190], using density functional methods (see Section 3.3.6). Finally it is to be noted that the low velocity stopping power $dE/ds \propto R(Z, \Gamma)v$ obtained for a one-component electron target provides already the stopping power in a (fully ionized) two component plasma for $v_{th}^{ions} < v \lesssim v_{th}-3v_{th}$ where v_{th}^{ions} is the thermal velocity of the target ions. Due to the high ion mass $v_{th}^{ions} \ll v_{th}$.

4.2.2. Charge dependence

We now concentrate on stopping at low velocities, parametrized in terms of the friction coefficient $R(Z, \Gamma)$, see Eq. (121), and investigate the dependence on the ion charge Z, particularly in the regime of nonlinear ion–target coupling. The left part of Fig. 5 shows the Z dependence of R computed with MD simulations for positively charged ions and various target correlations Γ, namely $\Gamma = 0.11$ (circles), $\Gamma = 0.34$ (triangles), $\Gamma = 1.08$ (diamonds) and $\Gamma = 3.41$ (crosses). The typical errorbars for the MD analysis can be looked up in the more detailed Fig. 6. At first glance, the MD results seem to line up with one common dependence on $Z\Gamma^{3/2}$. But a closer look reveals that results for different Γ have a different offset. Thus one has to conclude that $R(Z, \Gamma)$ depends on Γ and Z separately as expected from a full many-body dynamics. For comparison we have drawn a pure $Z^2\Gamma^3$-behavior as it corresponds to a naive extrapolation of dielectric theory to arbitrary Γ, see the dashed line in Fig. 5. It is obvious that the friction coefficient from MD increases slower
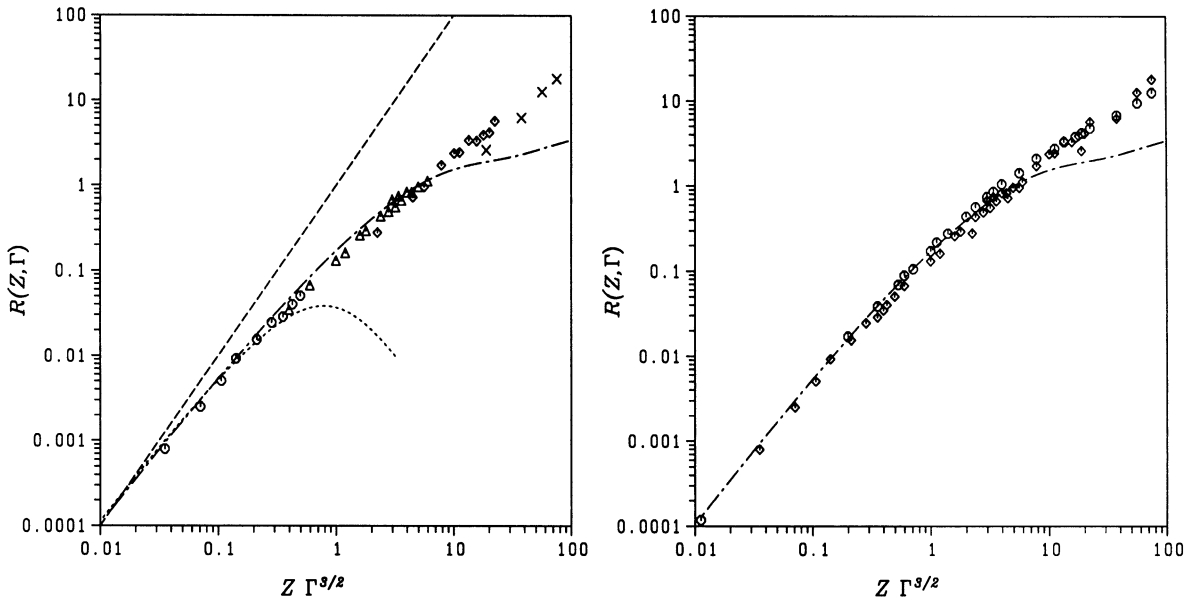

Fig. 5. Dimensionless friction coefficient $R(Z, \Gamma)$ (121) as function of $Z\Gamma^{3/2}$. The dotted curve represents the linear response description (129) and the dash-dotted curve the binary collision treatment (122) for the screened interaction (123) with $\lambda = \lambda_D$. To guide the eye and for comparison, a pure $Z^2\Gamma^3$ dependence (dashed line) is added. *Left plot*: MD-simulation results for various ion charge states Z and target plasmas with $\Gamma = 0.11$ (circles), $\Gamma = 0.34$ (triangles), $\Gamma = 1.08$ (diamonds) and $\Gamma = 3.41$ (crosses). *Right plot*: The circles are the results of Vlasov simulations which only depend on $Z\Gamma^{3/2}$. The diamonds are the MD results given in the left part now not further distinguished with respect to Γ.
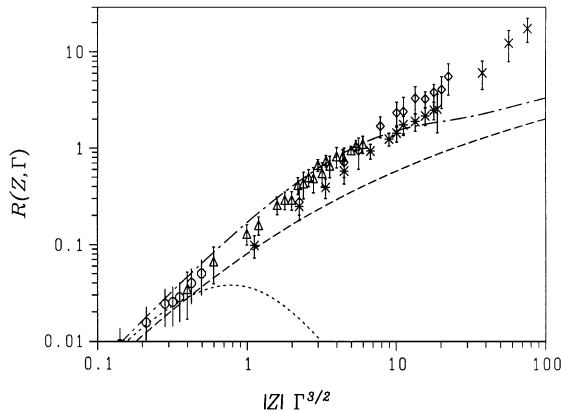
Fig. 6. Dimensionless friction coefficient $R(Z, \Gamma)$ (121) as function of $|Z| \Gamma^{3/2}$. MD-simulation results of Fig. 5 for different $Z > 0$ and $\Gamma = 0.11$ (circles), 0.34 (triangles), 1.08 (diamonds), 3.41 (crosses), now in more detail and with errorbars (standard deviations, see Appendix A.1) together with MD results for different $Z < 0$ and $\Gamma = 1.08$ (stars). The various curves show the friction coefficient R as obtained in the linear response description, Eq. (129) (dotted) and the binary collision treatment, Eqs. (122) and (123) with $\lambda = \lambda_D$, for positively (dash-dotted) and negatively charged ions (dashed).

than Z^2. The Z-dependence for targets with $\Gamma \geq 0.34$ fits well on a simple power law $R \propto Z^x$ with $x \lesssim 1.5$ for each fixed Γ. This is compared with the theoretical predictions for R of the linear response description Eq. (129) (dotted curve) and the binary collision approach, Eq. (122), for the screened interaction (123) at $\lambda = \lambda_D$ (dash-dotted curve), which both depend only on $Z\Gamma^{3/2}$. Here, the binary collision result represents the friction coefficient corresponding to both the previously discussed combined expression $(dE/ds)_{\text{com}}$ and the binary collision expression (119) with the velocity dependent screening length from Eq. (132), which become identical in the low velocity limit. The linear response result as well as the binary collision prediction deviates from the simple Z^2 law as expected for the stopping power in the semilinear regime. The linear response results follows the trend of the Z dependence for quite a while, but then it fails grossly for nonlinear coupling with $|Z|\Gamma^{3/2} \gtrsim 1$. The curve bends over and finally falls off like $(Z\Gamma^{3/2})^{-2}$ for large $|Z|\Gamma^{3/2}$. The charge dependence of the binary collision description agrees generally better with the MD simulation results, but for large $Z\Gamma^{3/2} > 10$ it also underestimates the friction coefficient R.

The right part of Fig. 5 shows a comparison between the MD (diamonds for all Γ) and Vlasov (circles) simulation results again for various Z and Γ. The friction coefficient $R(Z, \Gamma)$ of the Vlasov simulations depend only on the product $Z\Gamma^{3/2}$ as expected for a mean-field description. The friction coefficient and thus the stopping power exhibit a very similar charge dependence in the mean-field treatment as compared to the full MD which includes electron–electron correlations. Thus the nonlinear effects which lead to the typical trend $\propto Z^{1.5}$ are already present at the mean-field level. There remain, however, differences between the mean-field description and the MD simulations due to correlations, as seen from the separate Z and Γ-dependence of the MD results.

Fig. 6 enlarges a part of Fig. 5 (left) with MD results for $R(Z, \Gamma)$ now shown with errorbars. In addition, MD results for negatively charged ions at $\Gamma = 1.08$ are shown (stars). Results from the binary collision description, Eq. (122) with interaction (123) and $\lambda = \lambda_D$, are shown for $Z > 0$

(dash-dotted) and $Z < 0$ (dashed). We see larger stopping powers for positive ions than for negative ions in both, the MD and the binary collision results. This difference will vanish, of course, for weak coupling $|Z|\Gamma^{3/2} \ll 1$. The binary collision results for positive ions (dash-dotted curve) show a bump at $Z\Gamma^{3/2} \approx 2$–10 which is absent for the negative ones. This is due to electron scattering events with scattering angles larger than $180°$ (resonant states).

To judge on the agreement between the simulation results and the binary collision description we better compare with the Vlasov simulations. There the particles move, after a transient period, in a constant mean field as it is assumed in the binary collision approach. Both descriptions depend only on $Z\Gamma^{3/2}$ whereas the MD simulations additionally distinguish different degrees of internal correlation. This better agreement of the binary collision results (dash-dotted) with the Vlasov (circles) than MD results (diamonds) can be seen in the right plot of Fig. 5 or more clearly when comparing Fig. 6 with the left part of Fig. 7. The remaining differences of the Vlasov simulations and the binary collisions at large $Z\Gamma^{3/2}$ are due to the fact that the selfconsistent potential in the Vlasov calculations differs in these cases from the effective potential (Eq. (123) with $\lambda = \lambda_D$) assumed for the binary collisions. There nonlinear screening becomes more involved with increasing $Z\Gamma^{3/2}$. This is taken into account for obtaining the improved solid curve in Fig. 7 (left plot) by
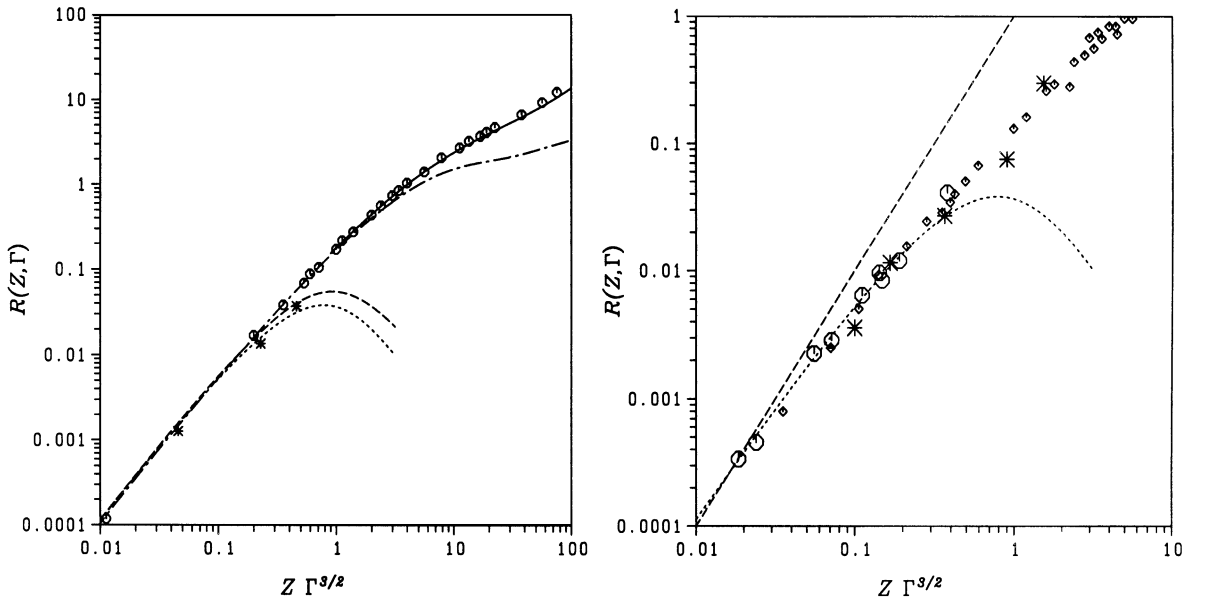

Fig. 7. Dimensionless friction coefficient $R(Z,\Gamma)$ (121) as function of $Z\Gamma^{3/2}$. The dotted curves represents the linear response description Eq. (129). *Left plot*: Vlasov (PIC/test-particle) simulation results (circles) as shown in the right part of Fig. 5 and the results (stars) of numerical solutions of the Vlasov–Poisson equations on a grid in phase-space from Ref. [23]. The dash-dotted and the solid curves represent the binary collision treatment (122) with interaction (123) for $\lambda = \lambda_D$ and $\lambda = \lambda(Z\Gamma^{3/2}) = \lambda_D(1 + 0.09(Z\Gamma^{3/2})^{0.6})$ (see Section 4.3), respectively. For the dashed curve, the next order term of the target response, as calculated in Ref. [135], was added to the linear response contribution. *Right plot*: The diamonds are the MD-simulation results for various Z and Γ of Fig. 5. The dashed line is a pure $Z^2\Gamma^3$ dependence. The large symbols are the experimental results from cooling force measurements by Wolf et al. [188] (circles) and Winkler et al. [185] (stars) adapted to the case of an isotropic plasma assuming an effective temperature of $T = 3.1T_{\parallel}$ and $T = 7.1T_{\parallel}$, respectively (see text).

employing instead of λ_{D} a screening length $\lambda(Z\Gamma^{3/2})$ extracted from the effective potential observed in the simulations. This will be discussed in more detail later on in Section 4.3.

4.2.3. Comparison with other approaches and experiments

The left part of Fig. 7 compares $R(Z,\Gamma)$ obtained from test particle Vlasov simulations (circles), the binary collision model for two different choices for λ (dash-dotted and solid), the linear response approach with cutoff (dotted), linear response plus perturbative corrections (dashed), and a numerical solution of the Vlasov–Poisson equations on a grid (stars). The solution on a grid employed cylindrical symmetry which yields a reduced treatment in a four dimensional phase space, see Ref. [23]. Even then the method is very expensive and only few points are available. These points exhibit a slightly reduced friction and are practically identical with the results of a test-particle solution of the Vlasov equation also in cylindrical symmetry reported in Ref. [38]. The smaller stopping power found in these investigations may be in part due to the reduced dimensions which excludes several excitation modes but the major cause is probably the different treatment of the ion–electron interaction at short distances. In typical grid based numerical schemes the finite grid size automatically introduces a short distance cutoff of the Coulomb potential, whereas a proper description also of the close ion–electron collision requires additional efforts and a special treatment as included in the test-particle simulations (circles) reported here, see Appendix A.2.

The result of a perturbative treatment to the next order beyond linear response is taken from Ref. [135]. It is based on a classical treatment and requires a cutoff k_m at large momentum transfer. With the standard choice of this cutoff given by Eq. (127) the friction coefficient including the next order term (dashed curve) thus bends over and falls off for $|Z|\Gamma^{3/2} \gtrsim 1$ like the linear response result (dotted). The example demonstrates the character of any perturbative description. The higher order corrections remain negligibly small for very weak perturbations $|Z|\Gamma^{3/2} \ll 1$ and improve the results for increasing strength of the perturbation. But it is only a small range of intermediate coupling where this next term suffices for a satisfying description. Very soon an increasing number of perturbative terms is needed which make the whole perturbative expansion obsolete for strong perturbations $|Z|\Gamma^{3/2} \gtrsim 1$.

Experiments on the stopping of highly charged heavy ions in dense and highly ionized target plasmas are in progress [82,83,42,43,59,163,33,34,94,95,171]. But the plasma densities are not yet sufficiently high to reach the regime of nonlinear projectile–target coupling. There exist, however, experimental results from measuring the cooling force for electron cooling in heavy ion storage rings. In the electron cooler the ions of the stored ion beam are merged with a cold electron beam once in each cycle. Thermal energy is transferred from the ions to the cold electron plasma. This produces colder ion beams of lower phase-space volume [142]. The cooling of the ions can be related to the energy loss of an ion when moving through the electron cloud and the measured cooling force represents the stopping power averaged over the velocity distribution of the ions. The cooling forces at low ion–electron relative velocities observed experimentally show a Z^x dependence with x between 1.5 and 1.7 [170,185,186,188], more recent experiments at the experimental storage ring (ESR) at GSI, Darmstadt, yield even smaller values $x \approx 1.3$ [187]. This agrees qualitatively with the presented MD and test-particle results for isotropic electron plasmas. In the electron cooler, however, the situation is more complex because one has two different electron temperatures in the transversal and the longitudinal direction and because there is a longitudinal magnetic field which guides the electron beam. The typical parameters in the electron cooler at the

test storage ring (TSR) in Heidelberg are $n \approx 3 \times 10^7 \, \text{cm}^{-3}$, $k_B T_\perp \approx 0.1 \, \text{eV}$, $k_B T_\parallel \approx 1{-}5 \times 10^{-4} \, \text{eV}$ and $Z = 1, \ldots, 16$ [188], where $T_\perp$ denotes the temperature transversal to the beam direction and $T_\parallel$ longitudinal with the beam. These parameters stay safely in the regime of ideal target and linear ion–target coupling for the transversal temperature whereas the longitudinal temperature yields $\Gamma_\parallel \lesssim 0.7$ and $Z\Gamma_\parallel^{3/2} \lesssim 9$. The ESR in Darmstadt has the parameters $n \approx 10^6 \, \text{cm}^{-3}$, $k_B T_\perp \approx 0.15 \, \text{eV}$, $k_B T_\parallel \approx 5 \times 10^{-5} \, \text{eV}$ and $Z = 6, \ldots, 92$ [170,185]. That is again an ideal target and the ion–target coupling is linear for the transverse temperature but $\Gamma_\parallel \lesssim 0.4$ and $Z\Gamma_\parallel^{3/2} \lesssim 23$ for the longitudinal degree of freedom. The longitudinal conditions in both devices corresponds to a target close to the nonideal regime and to nonlinear coupling. In addition there comes the longitudinal magnetic field. This hinders the transversal motion of the electrons and thus freezes the hot transverse electronic degrees of freedom. There should remain an effective temperature for the ion–electron interaction which stays close to the longitudinal temperature. We compare the measured friction coefficients with MD simulations of an isotropic plasma by interpreting the experiments in terms of an effective temperature. The result is shown in the right part of Fig. 7. An effective temperature of $T = 7.1 T_\parallel$ (stars) had been used to adjust the data from [185] and of $T = 3.1 T_\parallel$ (circles) for comparison with [188]. The experimental trends are well reproduced which provides an experimental confirmation for the typical Z-dependence as seen in the MD simulations. Furthermore, the effective temperatures remain close to the given $T_\parallel$ which supports the picture of nearly frozen transversal degrees of freedom.

4.3. Screening and electron trapping

We discussed in Section 4.2.2 the Z-scaling of the stopping power and found a trend $\propto Z^x$, $x \approx 1.5$. This trend is related to the development of screening of a highly charged, slow ion. We have investigated that in detail in specific simulations. The Coulomb interaction between an ion at rest ($v = 0$) and the electrons was switched on at time $t = 0$ and the ion subsequently attracts electrons. The electron density about the ion grows and reaches an almost stationary state on a time scale of plasma periods τ_p. The screening function $\Upsilon(r)$ is then extracted as the total electric potential about the ion divided by the bare ion potential. The linear response theory yields $\Upsilon(r) = \exp(-r/\lambda_D)$ (Debye–Hückel). The screening function deduced from MD and Vlasov simulations for nonlinear coupling is also rather close to an exponential function $\Upsilon = \exp(-r/\lambda)$ but with a much different screening length $\lambda = \lambda(Z, \Gamma) > \lambda_D$. This suggests that the corresponding effective ion–electron interaction is well approximated by the potential (123) when λ is replaced by $\lambda(Z, \Gamma)$. The results for the observed screening length are shown in Fig. 8. The rather large errorbars reflect here not only the different initial states but mainly the imperfectness of matching the real potential to the simple exponential form $\exp(-r/\lambda)/r$. One sees that the screening length increases with the coupling strength, particularly for $Z\Gamma^{3/2} > 10$. This trend of the static screening is in good agreement with the trend of the friction coefficient. Remind the Figs. 5 and 7 (left part) where the friction coefficients at strong coupling $Z\Gamma^{3/2} \gg 1$ lie well above the results from the binary collision model where an interaction potential (123) with the linear response screening $\Upsilon(r) = \exp(-r/\lambda_D)$ was used. To be more quantitatively, a rough estimate for $\lambda(Z\Gamma^{3/2})$ can be deduced from the data in Fig. 8 as $\lambda(Z\Gamma^{3/2}) = \lambda_D(1 + 0.09(Z\Gamma^{3/2})^{0.6})$. Taking this screening length as an input for the ion–electron interaction (123) in the binary collision approximation Eq. (122) results in the solid curve in the left plot of Fig. 7 which agrees fairly well with the Vlasov simulation results. The
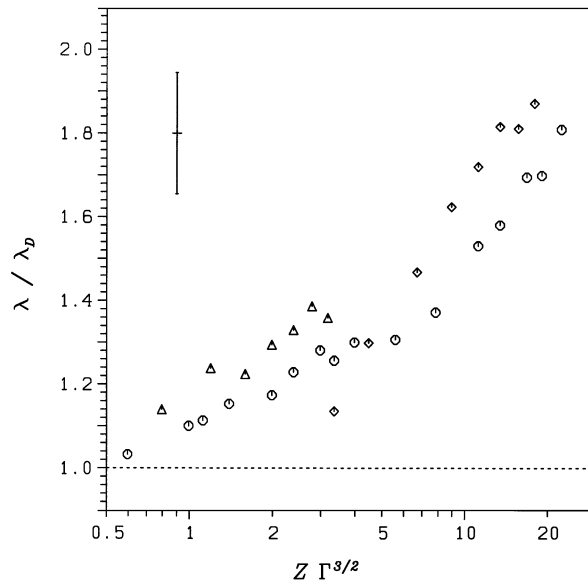
Fig. 8. Static screening length λ in units of the Debye length λ_D as function of $Z\Gamma^{3/2}$. MD-simulation results for different ion charge states Z and electron targets $\Gamma = 0.34$ (triangles) and $\Gamma = 1.08$ (diamonds) and Vlasov simulation results (circles) obtained from the observed approximatively exponential decay of the total electrical potential about the ion. The typical errors as indicated left top are mainly due to the imperfect agreement of the actual potential with the simple functional form $\propto \exp(-r/\lambda)/r$. The dotted line represents the constant screening length in the linear response description.

enhanced friction is clearly related to the enhanced screening length. Of course, the simple binary collision picture can only provide the qualitative trend of nonlinear stopping in an ideal target. The hard electron–electron collisions which are present in the MD simulations and which become increasingly important for increasing Γ give an additional contribution due to the target nonideality as documented by the separate dependence of $\lambda(Z, \Gamma)$, Fig. 8, and $R(Z, \Gamma)$, Fig. 6, on Z and Γ.

A further interesting observable related to screening is the electron density near the ion. We characterize it by the number of electrons $N(r < r_0)$ in a sphere of radius $r_0 = 0.3a \, (a = (4\pi n/3)^{-1/3})$ about the ion because this quantity can be sampled with reliable statistics in our MD simulations. Fig. 9 shows $N(r < r_0)$ for $Z = 10$ and $\Gamma = 1.08$ as function of the ion velocity v. The results represent the ensemble averages over the same simulation runs from which the stopping powers in Fig. 4 have been computed. MD-simulation results (diamonds) are compared with results from the Vlasov equation (circles) and the ideal gas value $N = n4\pi r_0^3/3 = (0.3)^3$ (dotted line). MD simulations produce a huge enhancement of $N(r < r_0)$ at low velocities compared to the ideal gas, about a factor of 80. The enhancement decreases for increasing velocity and vanishes completely at large ion velocities which agrees with the restoration of linear response at large velocities. But note how large the velocities have to be to recover that limit ($v/v_{th} > 5$). The Vlasov simulation results (circles) behave similar, however, with a considerably smaller enhancement at low velocities. Most of the electrons which contribute to this enhancement at low ion velocities are trapped in the ion
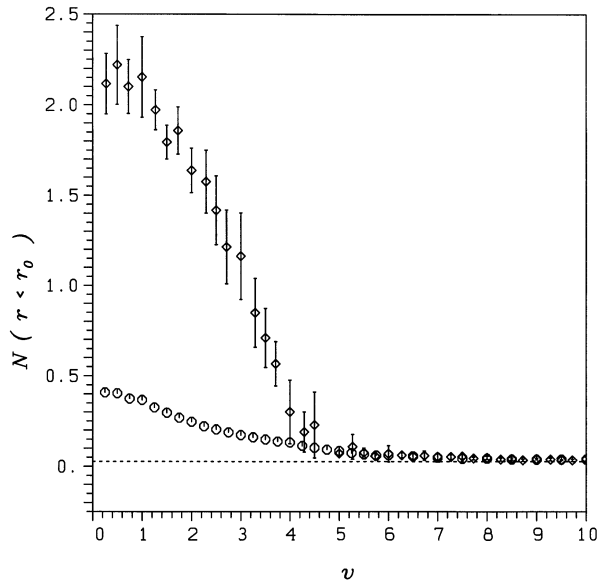
Fig. 9. Number of electrons N within a sphere of radius $r_0 = 0.3a$ ($a = (4\pi n/3)^{-1/3}$) about an ion of charge state $Z = 10$ as function of the ion velocity v in units of the thermal velocity $v_{th} = (k_B T/m)^{1/2}$ in a plasma with $\Gamma = 1.08$. The diamonds are results of MD-simulations, the circles show Vlasov simulation results. The dotted line indicates the ideal gas value $N = n4\pi r_0^3/3 = (0.3)^3$.

potential as can be concluded from the negative energies of these electrons. Here, this energy is determined as sum of the kinetic energy of relative motion and the potential energy in the field of the ion and the other electrons or in the mean-field. The trapping of electrons is a typical many-body effect, caused by an exchange of energy and momentum with the ion and the surrounding electrons in multi-particle collisions involving the ion and two or more electrons. Such processes are sensitive to the nonideality of the plasma, i.e. to the collisions and correlations between the electrons. While the electron–electron interaction and hence the nonideality effects are correctly treated in the MD-simulations, the trapping and the enhanced densities are suppressed in the Vlasov treatment. The behavior of the density near the ion is of course connected to screening and to the stopping power although in a rather intricate manner. While the electron densities close to the ion are quite different in the MD and Vlasov treatments, that is, in nonideal and ideal targets, respectively, the corresponding screening lengths behave very similar, see Fig. 8. In particular for negative ions where the charge density near the ion is reduced, the screening lengths is nevertheless enhanced over the Debye length at nonlinear coupling as we have observed in the simulations. This also contributes to the behavior of the friction coefficient in Fig. 6 for $Z < 0$ (stars) which lies for increasing coupling clearly above the binary collision prediction (dashed curve) for $\lambda = \lambda_D$.

The electron trapping is also of interest with respect to electron–ion recombination. The trapping of electrons by multi-particle collisions corresponds to recombinations into high Rydberg states of the ion. The enhanced electron densities and the population of loosely bound electron

states are one crucial mechanism to explain the enhancement of radiative recombination rates by factors of 4–5 as observed for a large number of ions in recent experiments with highly charged ions in heavy ion storage rings [13,57,157,177]. These experiments used the electron beam in the cooler as an electron target to study spontaneous or laser-induced radiative electron–ion recombination. It should be emphasized that these many-body effects can occur only for strong coupling. They are different from the usual three-body-recombination in an ideal target where a sufficiently strong interaction is only possible in the very unlikely event that an ion and two electrons come very close together. Therefore, the theoretical description of these processes always require a full MD-simulation for a proper description of the essential multi-particle collisions. One needs, of course, also to take into account the anisotropic electron temperatures and the presence of the magnetic field. Such extensive MD-simulations covering all these aspects were performed recently for an ion with charge $Z = 51$ at rest ($v = 0$) for typical target parameters in an electron cooler, here specifically those of the TSR at Heidelberg [169]. The resulting enhancement factor $n(r)/n$, here for the density which yields rather high errorbars, is shown in Fig. 10 for various strengths of the magnetic field. It represents the average over an interaction time of three plasma periods according to the typical time of flight through the cooling section of a storage ring. As a general trend the expected growing density enhancement with decreasing distance from the ion is clearly visible. But the magnetic field introduces further quite intricate influences and dependencies. At close distances an increasing magnetic field progressively reduces the density enhancement considerably while it seems to support the enhancement slightly farther away from the ion. We have to be aware, however, that we are here in an transient stage of the buildup of the electron cloud about the ion.
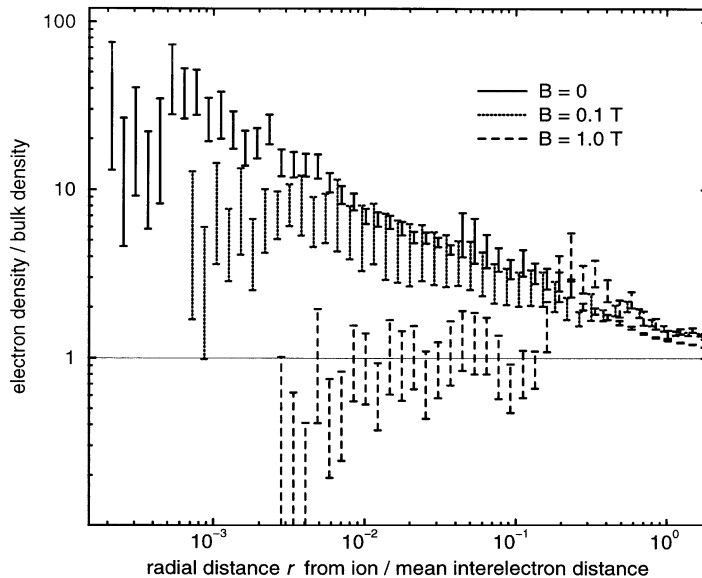

Fig. 10. Electron density about an ion with respect to the homogeneous density n as function of the radius r in units of $a = (4\pi n/3)^{-1/3}$ and averaged over $\tau = 3\tau_p \approx 35$ ns after switching on the ion–electron interaction. The ion of charge state $Z = 51$ is at rest in an anisotropic electron plasma as typical in an electron cooler with $n = 10^7$ cm^{-3} and $k_B T_\perp = 15$ meV, $k_B T_\parallel = 0.5$ meV and for magnetic field strengths $B = 0$ (solid bars) 0.1 T (dotted) and 1.0 T (dashed).

A closer look on the time evolution of the local density $n(r, t)$ then reveals the influence of the magnetic field on this buildup, see [169]. It becomes slower with increasing magnetic field which indicates a reduction of the mobility of the electrons connected to the freezing of the transversal degrees of freedom. Further MD studies on the local electron density around an ion are reported in [197,200,201].

5. Quantum effects

5.1. Stopping with effective potentials

MD simulations with classical point particles are orders of magnitude less expensive than fully fledged quantum mechanical methods. It is therefore tempting to map quantum features into a classical simulation by means of an effective potential. These are often derived from the quantum mechanical density matrix of the electrons in equilibrium and they thus incorporate all the needed smoothing from the quantum effects [76]. An effective potential between charges q_α and q_β, whose shape and parametrization have been adjusted to quantum chemical calculations has been proposed by Kelbg [97] and Deutsch et al. [39–41]. It is parametrized in simple local form as

$$V_{\text{eff}}(r) = -\frac{q_\alpha q_\beta}{4\pi\varepsilon_0 r}[1 - \exp(-r/\lambda_{\alpha\beta})] , \tag{133}$$

where all quantum effects are mediated through the short-range cutoff parameter $\lambda_{\alpha\beta}$. The WPMD simulations, on the other hand, aim at a direct simulation of the quantum system. But they also allow to determine an effective potential "a posteriori" by measuring the potential energy for every electron–proton pair as a function of the distance. This means essentially that one averages the electron–proton interaction (99)

$$V_{Ii} = \frac{e^2}{4\pi\varepsilon_0|R_I - r_i|} \text{erf}\left(\left|\frac{R_I - r_i}{\gamma_i}\right|\sqrt{\frac{3}{2}}\right) \tag{134}$$

for all pairs of ions and electrons and over observation time. The results are shown in Fig. 11. The "measured" effective potential from WPMD agree with the conventional effective potential in the gross features. Both models introduce a substantial reduction as compared to the Coulomb potential. At second glance, however, the WPMD result turns out to be softer than the potential (133). Of course the evaluation of V_{Ii} from a simulation contains statistical fluctuations about an average potential which are due to the influence of the surrounding medium in the evolution of the width of the wave packet. The fluctuations are indicated by errorbars in Fig. 11. Furthermore, calculations at higher densities indicate a density dependence of the effective potential, in contrast to the ansatz (133) and to the results in Ref. [76]. One could also expect that the effective potential depends on the velocity. This has been checked by making two alternative samplings, one taking into account only particles with more than twice of the thermal velocity and another one with a velocity window on less than half-thermal velocity. Both samplings give potentials which are very similar to the unbiased average drawn in Fig. 11. The WPMD data do therefore not require a velocity dependent effective interaction.
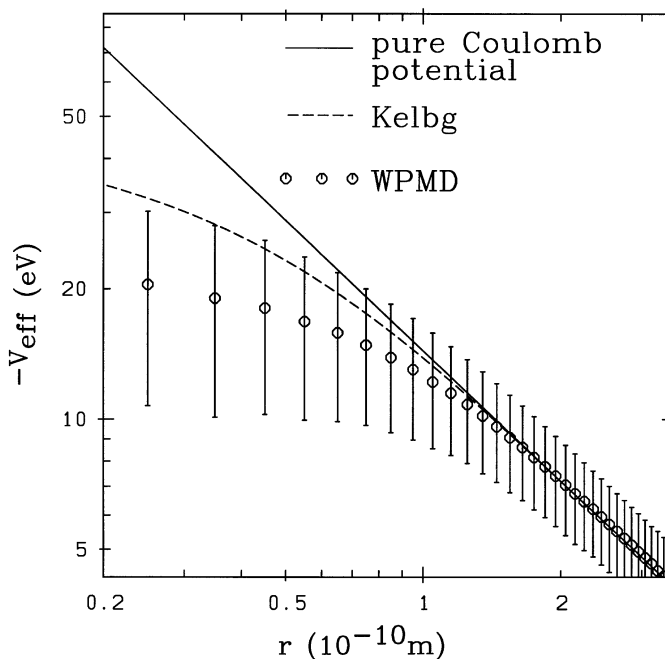
Fig. 11. (Effective) potentials as function of the distance. The solid line is the Coulomb potential, the dashed line is the effective potential (133) [97], and the points are averages obtained from Eq. (134) in WPMD-simulations. The errorbars reflect the fluctuations in the simulations.

The lack of velocity dependence also carries through to the effective potential for a moving ion as it is required for computing the stopping power. One expects that the wavelength $\lambda_{\alpha\beta}$ in Eq. (133) depends on the average relative velocity between ion and electron plasma. The quantum smoothing should decrease for $v \gg v_{th}$ and the full Coulomb potential should be recovered for further increasing velocity. The observation of such an effect in WPMD is hindered by the unpleasant fact that the statistical fluctuations grow with the ion velocity and the errorbars become much larger than those in Fig. 11. We have not yet been able to spot any significant velocity dependence in the effective ion–electron potential from WPMD simulations. But that is probably more than a problem of statistical sampling. The present gaussian approximation (88) is too crude to resolve the details of the effective interaction at large velocities. In fact, model studies of electrons moving between fixed scattering centers show that the exact wavefunction develops an anisotropic shape and some structures beyond gaussian wave packets.

We compare in Fig. 12 the friction coefficient (121) for classical MD simulations with the Coulomb potential as well as with effective potentials of type (133). The quantum effects incorporated into effective potentials reduce the stopping power. In the following we show that this quantum reduction of the stopping power can be based on treatments which involve quantum mechanics on a deeper level.
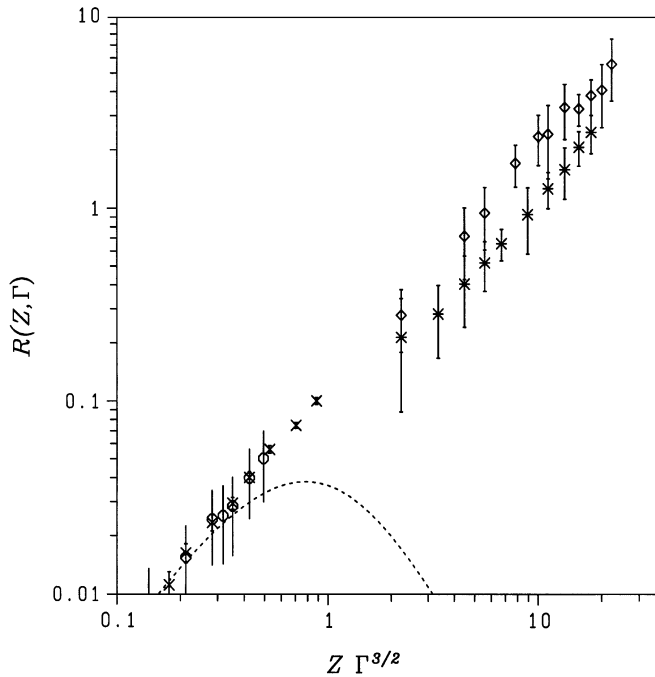
Fig. 12. Dimensionless friction coefficient $R(Z,\Gamma)$ (121) as function of $Z\Gamma^{3/2}$. Classical MD-simulations for various ion charge states Z with the Coulomb potential for $\Gamma = 0.11$ (circles) and $\Gamma = 1.08$ (diamonds) and with effective potentials of the functional form (133) for $\Gamma = 0.11$ (crosses) and $\Gamma = 1.08$ (stars) and a temperature of $k_B T = 10$ eV. The ranges of the potential (133) are $\lambda_{ep} = \hbar/(2\pi m k_B T)^{1/2}$ for the electron–projectile interaction and $\lambda_{ee} = 2^{1/2}\lambda_{ep}$ for the interaction between the electrons. The dotted curve is the linear response description (129).

5.2. Quantum stopping power

Qualitatively one expects that quantum effects reduce the stopping power. On one hand, quantum indeterminacy mollifies the Coulomb interaction near the origin, thereby reducing the probability of hard collisions with large momentum transfer. Furthermore, collisions are suppressed by Pauli-blocking in the degenerate regime. In order to exhibit the transition into the quantum regime we performed WPMD simulations of the stopping power for target parameters (n,T) shown as working points in Fig. 13 [101]. The plasma parameter was kept fixed near the dashed line at $\Gamma = 1.08$. With increasing temperature one moves then along this line from a nonideal, classical regime into the quantum regime. The ion has a charge number $Z = 5$ and mass $M = 80\,000m$. Fig. 14 shows the stopping power $-\,\mathrm{d}E/\mathrm{d}s$ as a function of the ion velocity v for the various working points shown in Fig. 13. On the scale employed the classical stopping power depends only on Γ, but not separately on n,T, as the quantum stopping power obviously does. The comparison of the classical simulation with the WPMD simulations at the working points of Fig. 13 shows indeed the trend envisaged above: The magnitude of the stopping power decreases when moving into the quantum regime. On the other hand the shape of $\mathrm{d}E/\mathrm{d}s$ as a function of the
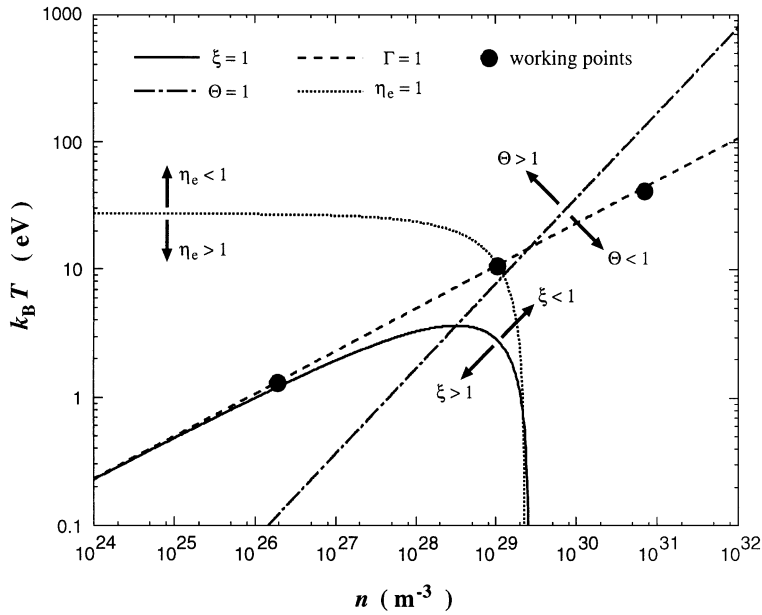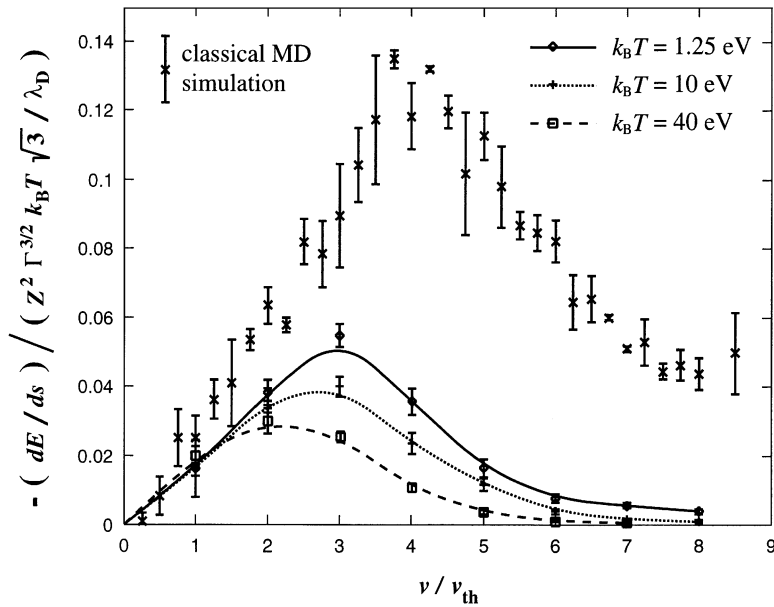
Fig. 13. Working points in the n–T-plane. See also Fig. 1.

Fig. 14. Normalized stopping power for $Z = 5$, $M = 80\,000m$ as a function of the ion velocity. The crosses are results from a classical simulation for $\Gamma = 1.08$. The results of the WPMD-simulations for $\Gamma = 1.08$ at the different temperatures corresponding to the working points given in Fig. 13 have been joined by curves to guide the eye.
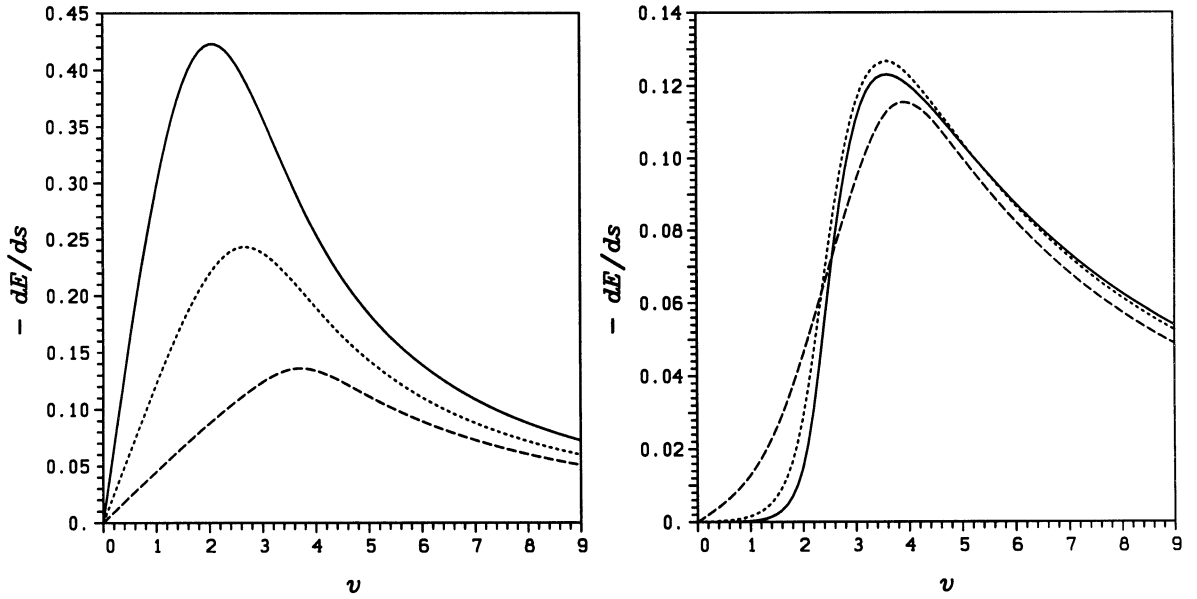
Fig. 15. Normalized stopping power $dE/ds/Z^2$ in units of $3^{1/2}\Gamma^{3/2}k_BT/\lambda_D$ as function of the ion velocity v in units of the thermal velocity $v_{th} = (k_BT/m)^{1/2}$ for $Z = 5$ and at the working points of Fig. 13 ($\Gamma = 1.08$) with $k_BT = 1.25$ eV (solid curves), $k_BT = 10$ eV (dotted) and $k_BT = 40$ eV (dashed). The left plot shows the linear response stopping power (39) with the RPA dielectric function (47), the right plot the semilinear stopping power (65) using the cutoff (68).

ion velocity remains unchanged, in particular we always observe a linear increase for small ion velocities $v \leq v_{th}$. For large velocities the simulation results should not be taken too quantitatively, as it becomes increasingly difficult to represent the infinite system by finite simulation boxes, see Appendix A.1.

We use this occasion to explore the range of validity of the RPA expressions (39), (47) which were obtained in the linear, ideal regime and extended into the regime of semilinear coupling by the cut-off (65)–(68). In the left plot of Fig. 15 we show the stopping power obtained from Eqs. (39) and (47). Due to the blocking factors in the dielectric function (47) the stopping power decreases as the working point moves into the quantum regime. While the shape of these curves is quite similar to the WPMD results in Fig. 14, the RPA results of Fig. 15 (left) turn out much too large. Indeed the RPA does not account for the wave nature of the electrons in their interaction with the projectile, which is therefore over-estimated if the coupling becomes strong. This can be corrected in the semilinear regime by introducing the cutoff (68), which reduces the stopping power as shown in the right part of Fig. 15. However, also this treatment fails for small velocities $v/v_{th} \leq 1$, where one enters the truly nonlinear regime $\langle \eta_p \rangle \geq 1$ (16).

5.3. Comparison of WPMD and LFC treatments

We discussed in Section 3.1.4 the LFC extension of the RPA. Higher correlations beyond the RPA are contained in the Local Field Correction $G(k, \omega)$ which effectively introduces a modified

residual interaction (48), (49). The LFC has been calculated by Ichimaru and coworkers for hydrogen in the regime of a liquid metal, e.g. $r_s = 1$ and $\Gamma = 2$. The protons were treated classically in the framework of the HNC. The electron–electron and the electron–proton correlations were studied in the framework of the modified convolution approximation (MCA) [174,91] for the LFC. In Fig. 16 the correlation functions of this HNC MCA scheme are compared with those obtained
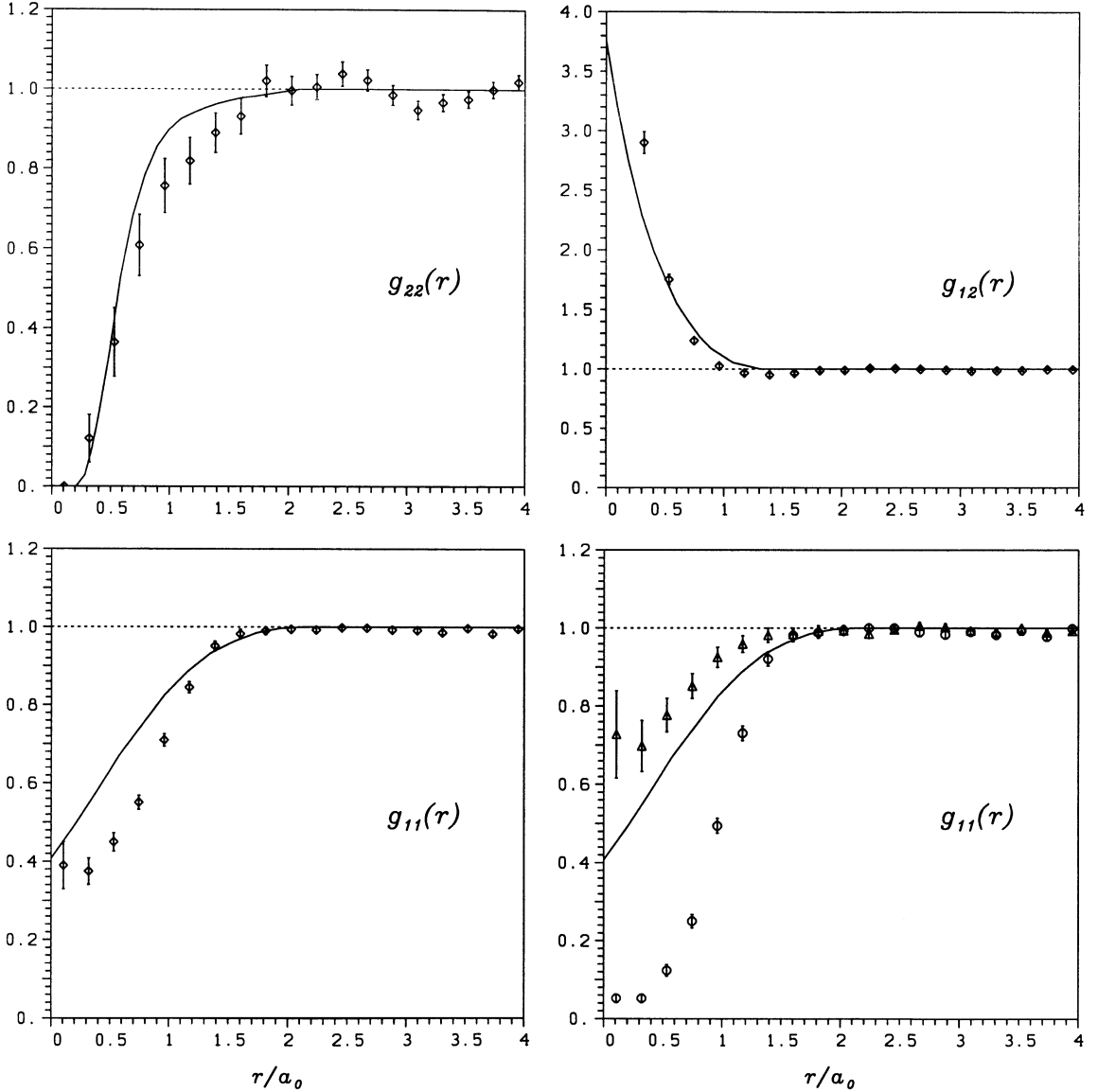

Fig. 16. Proton–proton $g_{22}(r)$, electron–proton $g_{12}(r)$ and electron–electron $g_{11}(r)$ pair correlation functions (radial distribution functions) for a hydrogen plasma with $\Gamma = 2$, $r_s = 1$, $k_B T = 13.6\,\text{eV}$, $n = 1.61\,\text{Å}^{-3}$, $k_F = 3.627\,\text{Å}^{-1}$. Points with errorbars: WPMD results for the spin averaged $g_{\mu\nu}$ (diamonds) and for parallel (circles) and antiparallel (triangles) electron spins, respectively. Solid curves: HNC MCA results from Ref. [91].

in the WPMD simulation. Quite generally the WPMD correlation function show for $r > a_0$ some long-range structure, which is not visible in the HNC MCA results. For $r \lesssim a_0$ the correlation holes in the WPMD are somewhat more pronounced. The correlation function for electrons with like spin approaches zero for $r \to 0$, i.e. the Pauli-principle is observed.

6. Conclusions

In this report on the stopping of ions in plasmas at strong coupling we have drawn attention to some recent important results and also emphasized some known, but hitherto rather neglected points.

1. We presented a careful and detailed classification scheme for various stopping regimes according to the target parameters density and temperature, or equivalently, ideality and degeneracy and according to the ion properties charge and velocity.
2. We identified three coupling regimes: Linear, semilinear and nonlinear. The semilinear regime is distinguished by the fact that the nonlinearity occurs only for a negligible fraction of space inside the typical shielding length. Rather universal methods like the RPA and the binary collision approximation are applicable in the linear and semilinear regimes. Extensions to nonlinear coupling require detailed investigations at large numerical expense. We found molecular dynamics and test-particle computer simulations very useful in this regime.
3. In agreement with experiments we find that the friction coefficient for slow ions in a plasma scales approximately like $Z^{1.5}$. This is of large importance for the electron cooling of highly charged ions in storage rings.
4. This change in the scaling is partly due to nonlinear shielding. The effective shielding length is larger than the Debye length and depends separately on the charge of the ion and the plasma parameter.
5. A highly charged slowly moving ion traps electrons, so that the electron density around the ion is increased. This may result in an enhanced recombination rate, as has been observed at several storage rings. For their effective operation it is essential that the cooling rate remains larger than the recombination rate.
6. Quantum effects like the wave nature of the electrons and Pauli-blocking tend to mollify the effective interaction and to reduce the stopping power.

Finally we want to point out some areas where further progress on the stopping power is highly desirable: Bound states and the variation of the charge state of the projectile should be calculated in a self-consistent manner. The WPMD should be generalized by admitting larger variational spaces than Gaussian wave packets in order to describe better the delocalization of the electrons, e.g. in metallic target states. For more realistic applications to electron cooling the influence of a temperature anisotropy in the plasma and of external magnetic guiding fields should be accounted for explicitly. Such work is in progress.

Appendix A. Description of the simulation techniques

A.1. MD-simulations

As outlined in Section 3.3.3 the MD-simulation technique provides the full many-body dynamics of a classical system by numerical integration of the Newtonian equations of motion. This allows in particular to study non-equilibrium properties of highly correlated systems without restrictions on the strength of the interaction. In this section, we sketch the simulation scheme as it was used to investigate the stopping power [191–197,199–201]. It is convenient to cast the equations of motion (79) into dimensionless form by introducing characteristic units for time, velocity, length and energy, given by the inverse of the plasma frequency, the thermal velocity, the Debye length and the thermal energy, i.e.

$$t_s = \omega_p^{-1}, \quad v_s = v_{th} = (k_B T/m)^{1/2}, \quad r_s = \lambda_D = v_{th}/\omega_p, \quad E_s = k_B T \ . \tag{A.1}$$

This leads to the set of coupled equations

$$\frac{d\tilde{\bm{r}}_i}{d\tilde{t}} = \tilde{\bm{u}}_i, \quad \frac{d\tilde{\bm{u}}_i}{d\tilde{t}} = -\frac{\partial}{\partial \tilde{\bm{r}}_i}\left[\sqrt{3}\Gamma^{3/2}\sum_{j\neq i}\frac{1}{|\tilde{\bm{r}}_i - \tilde{\bm{r}}_j|} - \frac{\sqrt{3}Z\Gamma^{3/2}}{|\tilde{\bm{r}}_i - \tilde{\bm{R}}|}\right],$$

$$\frac{d\tilde{\bm{R}}}{d\tilde{t}} = \tilde{\bm{v}}, \quad \frac{d\tilde{\bm{v}}}{d\tilde{t}} = \sqrt{3}Z\Gamma^{3/2}\frac{m}{M}\frac{\partial}{\partial \tilde{\bm{R}}}\sum_i \frac{1}{|\tilde{\bm{r}}_i - \tilde{\bm{R}}|}\ , \tag{A.2}$$

$$\tilde{\bm{r}} = \bm{r}/r_s, \quad \tilde{\bm{u}} = \bm{u}/v_s, \quad \tilde{\bm{R}} = \bm{R}/r_s, \quad \tilde{\bm{v}} = \bm{v}/v_s\ ,$$

$$\tilde{t} = t/t_s, \quad \sqrt{3}\Gamma^{3/2} = e^2\omega_p/(4\pi\varepsilon_0 k_B T v_{th})\ .$$

In this form, one can read off immediately the coupling parameters. The plasma parameter Γ characterizes the importance of the electron–electron interactions, and $|Z|\Gamma^{3/2}$ the strength of the ion–electron coupling. But one has to remind the strong Coulomb singularity at the ion position which produces large forces however small $|Z|\Gamma^{3/2}$ may be. The proper measure for linearity is $\varphi(0)$ or $\langle\eta_p\rangle$, see Eqs. (19)–(21) and the discussion in Section 2.3. The classical equations of motion (A.2) come never into a completely linear regime as there is always a small vicinity around the ion where fields are large and the condition for linearity, $\varphi(r) \ll 1$, is violated. In that case, weak perturbations correspond already to semilinear coupling and we recover in the ion–electron coupling strength $|Z|\Gamma^{3/2}$ the parameter which distinguishes for low ion velocities the semilinear regime ($|Z|\Gamma^{3/2} \ll 1$) from the nonlinear regime ($|Z|\Gamma^{3/2} \geq 1$), see Eqs. (24) and (25).

A particular MD-simulation based on an integration of Eq. (A.2) depends on Γ, Z, the mass ratio m/M and the initial positions and velocities of the particles. Global observables, as e.g. the stopping power, are obtained with ensemble averaging. These depend only on Γ, Z and the initial ion velocity v. The exact value of the ion mass M remains unimportant as long as $M \gg m$. The target conditions, temperature T and density n, enter only through the plasma parameter in the combination $n^{1/3}/T \propto \Gamma$ such that simulation results for a given Γ (and Z, v) yield the stopping power for a variety of target parameters n and $T \propto n^{1/3}$. Finally, we want to point out that the stopping power in MD simulations depends on both, target condition Γ as well as ion–electron coupling $Z\Gamma^{3/2}$, whereas the Vlasov–Poisson equations (75)–(77) depend only on $Z\Gamma^{3/2}$ (and v). The parameter Γ which accounts for the correlations in the target becomes meaningless in a mean-field description.

It is obvious that one can only afford to propagate a finite number of electrons in a MD simulation. The expense grows quadratically with the particle number because the long-range Coulomb force needs to be evaluated between each pair. On a workstation, one can typically afford a system of 500 particles. The actual plasmas, however, contain a macroscopic number of particles. Such a practically infinite system is approximated by treating a finite number of electrons in a cubic simulation box of length L and continuing this box periodically in each direction. A particle is thus replaced by a cubic lattice of particles and the Coulomb interaction by the Ewald sum of Coulomb interactions [72,128]. The neutralizing background of positive charges is simplified in the jellium approach where the positive background is distributed homogeneously. The actual definition and calculation of the Ewald force are given in Ref. [72], Appendices A and B. One has to be cautious to avoid artifacts from the artificial periodic structure. Results become unreliable as soon as long-range correlations are propagated outside a simulation box into the next one. This is avoided if the screening length λ remains below the box length L. The volume of the box, L^3, is related to the particle number N through $L^3 = N(4\pi a^3/3)$, where a denotes the Wigner–Seitz radius of the electrons. In terms of the classical plasma parameter Γ and the screening length $\lambda = \lambda_D(1 + (v/v_{th})^2)^{1/2}$ (which can be used as an estimate also for strong coupling, see Section 4.3) we obtain

$$1 \overset{!}{<} \frac{L}{\lambda} = \left(\frac{4\pi}{3}N\right)^{1/3}\left[\frac{3\Gamma}{1 + (v/v_{th})^2}\right]^{1/2} \approx 22.2\left[\frac{\Gamma}{1 + (v/v_{th})^2}\right]^{1/2}, \tag{A.3}$$

where we used $N = 500$ in the last step. For an application of MD-simulations to heavy ion stopping, the favorable regime lies at low ion velocities with nonlinear coupling and at nonideal targets $\Gamma \geq 0.1$ where one easily meets the conditions $L/\lambda > 1$. This is confirmed by simulations using $N = 250$ and $N = 5000$ electrons, where the observed stopping power at low velocities remains unchanged compared to the standard number $N = 500$. For high ion velocities, on the other hand, one has to be aware of artifacts from the periodic simulation lattice, as e.g. interference effects in the wake fields excited by the ion and its images. Such unwanted side-effects limit the use of the MD technique. They can be turned into a truly physical effect when considering the ion–ion correlations in the stopping of a lattice of ions, as has been done in [192,195,198].

MD simulations with the full Coulomb force run into a technical difficulty. Occasionally, particles come very close to each other, in particular for the attractive ion–electron interaction. There arise large forces and high velocities which require to reduce the time step. This slows down

the numerical propagation and one can easily get stuck in an intractable situation. To overcome this deadlock, we extended the conventional MD-simulation scheme by a separate treatment of close collisions, now taking advantage of the fact that the timescales in the close collision region are much smaller than those for the system as a whole. Hence, we check in each time step the occurrence of clusters of close particles which are defined by setting an appropriate chosen critical distance d_c, where a particle belongs to a cluster if its distance to at least one other particle in the cluster is less than d_c. While all particles outside a cluster are propagated with the standard time step Δt, the most frequent binary clusters are propagated with the analytically known trajectories of the Rutherford problem. The few remaining larger clusters are propagated numerically but with a much reduced time step as compared to Δt. The interaction between the cluster and the rest of the particles is computed at the slower time-scale of the whole system by mediating to the cluster particles once a momentum shift according to the external forces (i.e. the sum of the forces from all other particles) and taking into account, of course, the reverse effect on the other particles. This suffices to guarantee momentum and energy conservation of the whole simulation. The outlined technique of a separate treatment of clusters of close particles considerably reduces computing time and ensures high stability of the simulations. The numerical integration of the equations of motion for all particles outside a cluster with the time step Δt as well as for those within higher clusters and with a much smaller time step is performed by a standard Velocity–Verlet algorithm [4,178].

Actual simulations to compute the stopping power proceed in two phases. First, the pure electron system is relaxed to an equilibrium stage without the ion. Then the ion with velocity v is added suddenly at an arbitrary location, and in the second phase the full system of ion and electrons is propagated. The initial equilibration starts from a random sampling of positions and velocities and relaxes towards the equilibrium distribution of desired temperature by dynamical propagation with velocity rescaling. The second phase aims to simulate the full propagation with the ion. In contrast to a truly infinite system, the energy loss of the ion is distributed over a "very finite" number of electrons and thus induces some heating of the electrons. We need a scheme for repeated cooling, in order to obtain the stopping power for a well defined target temperature T. To that end, we select a part of the electrons which is far away from the ion, i.e. outside a given sphere with a radius $r \gtrsim \lambda_D$ about the ion, and restore the initial temperature T by drawing new velocities from the corresponding Maxwell distribution. This is done in regular time intervals of 1–3 plasma periods $\tau_p = 2\pi/\omega_p$. A complete simulation run takes typically $10\text{–}15\tau_p$, which requires $\sim 10\,000\text{–}15\,000$ time steps Δt and around 1–3 h on a work station. The accuracy and stability of the runs are monitored using the total energy. The propagation thus stabilized is accompanied by the analysis of the stopping power. The energy loss ΔE and the travelled path Δs of the ion are "measured" in each time step resulting in an instantaneous stopping power $(\Delta E/\Delta s)(t)$. The stopping power is finally obtained as the time average $\langle \Delta E/\Delta s \rangle$ over the instantaneous $\Delta E/\Delta s$. Since the projectile mass is large compared to the electron mass (usually $M = 50\,000\text{–}10\,0000\,m$), the projectile velocity changes only slightly ($< 1\%$) and the ion travels almost perfectly along a straight line and we have $\langle \Delta E/\Delta s \rangle = \langle \Delta E \rangle / \langle \Delta s \rangle$, which represents the stopping power dE/ds for the given velocity v. These time averaged values include the transient period after adding the ion where the stopping power has not yet reached a stationary value. But this period is small, usually $< \tau_p$ [160,161], and affects the results only weakly. From several runs with the same Γ, Z, v, but different samplings of the initial state, an ensemble average over the time averaged $\langle \Delta E/\Delta s \rangle$ is performed and yields finally the stopping power. The error can be deduced from the fluctuations in

the ensemble of events. The errorbars shown in Figs. 4, 6, 9, 12 and 14 represent the standard deviations and *not* the (smaller) mean error of the mean.

A.2. PIC/Test-particle simulations of ion stopping

In addition to the previously described MD-simulations we performed particle-in-cell (PIC) simulations with test particles, a method commonly used for numerical solutions of nuclear dynamics [18,148]. The PIC simulations use particle propagation similar as the MD simulations. But the aim is much different. PIC is designed to solve the Vlasov–Poisson equation (see Section 3.3.1) for the smooth phase-space distribution $f(\mathbf{r}, \mathbf{u}, t)$, thus carrying only the mean-field aspects and discarding any correlations. It turns out, however, that the most efficient way to solve the Vlasov equation recurs to the concept of particle propagation in that the distribution is represented as a superposition

$$f(\mathbf{r}, \mathbf{u}, t) = \frac{N}{N_{\mathrm{T}}} \sum_i w(\mathbf{r} - \mathbf{r}_i(t)) w_u(\mathbf{u} - \mathbf{u}_i(t)) , \tag{A.4}$$

where w and w_u are smooth and fairly well concentrated, normalized wave-packets in phase space. The representatives i are pseudo-particles, N_{T} is the number of pseudo-particles and N the number of physical particles. We use here the PIC simulations to compare the mean-field propagation with the fully correlated MD simulations. To that end, we suppress the interparticle correlations by splitting each physical target electron into a large number of test particles, typically $N_{\mathrm{T}}/N = 350$. The test particles have smaller mass $m_{\mathrm{T}} = mN/N_{\mathrm{T}}$ and charge $q_{\mathrm{T}} = eN/N_{\mathrm{T}}$, but the physical charge to mass ratio $q_{\mathrm{T}}/m_{\mathrm{T}} = e/m$. The test particles follow the Newtonian equations of motion in the ionic field and in the mean-field ϕ produced from their own charges. Using the same natural units (A.1) as in Eq. (A.2)

$$\frac{\mathrm{d}\tilde{\mathbf{r}}_i}{\mathrm{d}\tilde{t}} = \tilde{\mathbf{u}}_i, \quad \frac{\mathrm{d}\tilde{\mathbf{u}}_i}{\mathrm{d}\tilde{t}} = -\frac{\partial}{\partial \tilde{\mathbf{r}}_i} \left[\tilde{\phi}(\tilde{\mathbf{r}}_i) - \frac{\sqrt{3}Z\Gamma^{3/2}}{|\tilde{\mathbf{r}}_i - \tilde{\mathbf{R}}|} \right],$$

$$\frac{\mathrm{d}\tilde{\mathbf{R}}}{\mathrm{d}\tilde{t}} = \tilde{\mathbf{v}}, \quad \frac{\mathrm{d}\tilde{\mathbf{v}}}{\mathrm{d}\tilde{t}} = \sqrt{3}Z\Gamma^{3/2} \frac{mN}{MN_{\mathrm{T}}} \frac{\partial}{\partial \tilde{\mathbf{R}}} \sum_i \frac{1}{|\tilde{\mathbf{r}}_i - \tilde{\mathbf{R}}|} , \tag{A.5}$$

$$\tilde{\varrho}(\tilde{\mathbf{r}}, t) = -\frac{N}{N_{\mathrm{T}}} \sum_i \tilde{w}(\tilde{\mathbf{r}} - \tilde{\mathbf{r}}_i) ,$$

$$\tilde{\Delta}\tilde{\phi}(\tilde{\mathbf{r}}, t) = -\tilde{\varrho}(\tilde{\mathbf{r}}, t) ,$$

$$\tilde{\varrho} = \frac{\varrho}{en}, \quad \tilde{w} = \frac{w}{n}, \quad \tilde{\phi} = \frac{e\phi}{E_s} = \frac{e\phi}{k_{\mathrm{B}}T}, \quad \tilde{\Delta} = r_s^2 \Delta .$$

One sees immediately from these scaled PIC equations that propagation now depends only on the combined coupling parameter $Z\Gamma^{3/2}$. The explicit dependence on Γ, which was present in the MD simulations and which characterized target correlations, has disappeared as it should be for a proper mean-field dynamics.

A few remarks on the technical aspects of the PIC scheme are in order. Note that compared to the MD-simulations for N electrons (79) the equations (A.5) now run over $N \cdot N_{\mathrm{T}}$ test particles and

the direct electron interaction is replaced by the mean-field potential $\phi(\mathbf{r})$. In addition to the numerical integration of the particle propagation, the charge density ϱ is sampled on a spatial grid from the sum of the test-particle weight functions w and the selfconsistent field ϕ is determined by solving the Poisson equation $\Delta\phi(\mathbf{r},t) = -\varrho(\mathbf{r},t)/\varepsilon_0$ on the grid. The forces on the particles are retrieved from the grid using the same weight functions again, for details see [18,80,148]. The expense of accumulation of the density ϱ and of retrieval of the forces grows only linearly with the number of test particles. Thus one can afford a large number of those. Our PIC simulations, e.g., have been done with $N_T = 175\,000$ test particles. The density and mean field have usually been handled on a $32 \times 32 \times 32$ grid in coordinate space. Both numbers have been varied to check the stability of the results. Particle propagation and separate handling of close electron–ion collisions remains as in the MD simulations, see the previous subsection. The Poisson equation is solved in Fourier space using fast Fourier transformation to switch forth and back. The periodic boundary conditions, and the related Ewald summation, are automatically taken care of by using the Fourier transformation with complex exponentials.

We close this section with a remark on the versatility of the PIC method. We used it here for comparison with MD simulations in order to work out effects of the nonideality of the target. To that end, electron–electron correlations had been suppressed by using a large number N_T/N of test particles per electron. One can equally well use PIC simulations in the regimes where correlations are unimportant in the target. Thus one can go for the opposite strategy to pack several electrons into one numerical macro-particle, i.e. $N_T/N \ll 1$. This allows to use large simulation boxes, larger than the (large) screening length of those loosely correlated systems. Thus the PIC simulations can penetrate into the regime $\Gamma \ll 1$ which is inaccessible to MD simulations for reasons of the numerical effort.

A.3. WPMD-simulations

With the help of the variational principle the quantum problem was mapped into a classical one with additional degrees of freedom, see Section 3.3.4. This is solved according to the general methods outlined in Appendix A.1. The Ewald sum (100) was calculated and stored on a lattice of 75^3 points. The actual values required during the simulation were obtained by linear interpolation ([129], ch. 3) according to

$$\mathscr{V}_{\mathrm{Ewald}}(\mathbf{r}) = \mathbf{a}(\mathbf{r}) \cdot \mathbf{r} + \mathbf{r} \cdot \overset{\leftrightarrow}{B} \cdot \mathbf{r} + c(\mathbf{r})xyz \tag{A.6}$$

with $\mathbf{r} = (x,y,z)$. As the Ewald sum is smoothly varying over the width of the wave packet, the same expression is used for the electrons as for the ions. The resulting set of differential equations is solved with a second order Runge–Kutta algorithm. As the computation of the forces between the pseudo-classical particles in Eqs. (89)–(101) requires most of the computational effort, it is essential to set up the code in a hierarchical manner [101]. The ith particle is propagated with a time step

$$\Delta t_i = \tau\left(\min_{i<j} 2^{-n_{ij}}\right),$$

where τ is an arbitrary scale factor and $n_{ij} \in \mathbb{N}$ is chosen in such a manner that

$$n_{ij} = \min \left\{ n \in \mathbb{N} \left| \tau 2^{-n} < \beta \min_{i<j,k} \sqrt{\left| \frac{\boldsymbol{F}}{\ddot{F}_k(i,j)} \right|} \right. \right\} ,$$

where $F_k(i,j)$ is the kth ($k = (x, y, z, \gamma)$) component of the force between the ith and the jth particle, and $\boldsymbol{F}$ is a constant average force. The desired accuracy is controlled by the parameter $\beta (\approx 10^{-2})$.

Appendix B. Definitions and list of symbols

B.1. Stopping power for infinite projectile mass

The limit of infinite projectile mass ($M \to \infty$) allows an alternative derivation of expression (6) for the stopping power. The ion moves with constant velocity and thus the Hamiltonian (2) reduces to the simpler one $\hat{H}'(t) = \hat{H}_0 - \theta(t - t_0) \sum_i e \phi_{\mathrm{p}}(\hat{\boldsymbol{r}}_i - \boldsymbol{v}t)$, where now ϕ_{p} acts as an external moving potential at position $\boldsymbol{v}t$. Since we have no change in momentum or energy of the projectile, the stopping power must be derived from the energy transfer to the target. Guided by expression (3) the stopping power can be defined for $t > t_0$ through

$$\frac{\mathrm{d}E}{\mathrm{d}s} = -\frac{1}{v}\frac{\mathrm{d}}{\mathrm{d}t}\langle E \rangle = -\frac{1}{v}\frac{\mathrm{d}}{\mathrm{d}t}\mathrm{Tr}\hat{\rho}(t)\hat{H}'(t) = -\frac{1}{v}\mathrm{Tr}\hat{\rho}(t)\frac{\partial}{\partial t}\hat{H}'(t)$$

$$= \frac{1}{v}\mathrm{Tr}\hat{\rho}(t)\frac{\partial}{\partial t}\sum_i e\phi_{\mathrm{p}}(\hat{\boldsymbol{r}}_i - \boldsymbol{v}t) = -\mathrm{Tr}\,\hat{\rho}(t)\sum_i e\frac{\boldsymbol{v}}{v}\cdot \nabla_{r_i}\phi_{\mathrm{p}}(\hat{\boldsymbol{r}}_i - \boldsymbol{v}t)$$

$$= -\int \mathrm{d}^3r_1 \dots \mathrm{d}^3r_N \langle \boldsymbol{r}_1, \dots, \boldsymbol{r}_N|\hat{\rho}(t)|\boldsymbol{r}_1, \dots, \boldsymbol{r}_N\rangle \sum_i e\frac{\boldsymbol{v}}{v}\cdot \nabla_{r_i}\phi_{\mathrm{p}}(\boldsymbol{r}_i - \boldsymbol{v}t) \,. \tag{B.1}$$

Rewriting the last term by introducing the charge density

$$\varrho(\boldsymbol{r}, t) = -e\sum_i \int \mathrm{d}^3r_i \, \delta^3(\boldsymbol{r} - \boldsymbol{r}_i) \prod_{j \neq i} \int \mathrm{d}^3r_j \langle \boldsymbol{r}_1, \dots, \boldsymbol{r}_N|\hat{\rho}(t)|\boldsymbol{r}_1, \dots, \boldsymbol{r}_N\rangle$$

and the electrical field $\mathscr{E}$ we immediately recover the result (6). We observe in addition that the steady excitation leads to a final steady state with constant stopping which depends only on the velocity of the inert ion, see Eq. (7).

B.2. Alternative derivations of the parameter of linearity

The expression for the local strength of the ion–target coupling Eqs. (19) and (20), and the subsequent definition of linear coupling by definition (21) are based on the semiclassical expression (18) for the potential energy where quantum effects are included in an approximative manner only. Here we sketch two fully quantal approaches for deriving a criterion for linear coupling to substantiate the previous considerations in Section 2.3.2.

One alternative way to characterize the coupling strength starts from a look at ion–electron Coulomb scattering. There the stationary Schrödinger equation reads (for $Z > 0$)

$$\left(\Delta_{\tilde{r}} + 1 + \frac{2\eta_{\mathrm{p}}}{\tilde{r}} \right) \psi_{\mathrm{c}}(\tilde{r}) = 0$$

with $\tilde{r} = r/\lambda_{\mathrm{r}}$ and the pure Coulomb wave $\psi_{\mathrm{c}}(\tilde{r}, \eta_{\mathrm{p}})$ [122,155]. Here, a measure of the coupling strength is established by comparing the probability of finding the electron at the ion position with the free particle case $\eta_{\mathrm{p}} = 0$. From the known behavior of the Coulomb wave one easily derives the relative change

$$\frac{|\psi_{\mathrm{c}}(\tilde{r} = 0, \eta_{\mathrm{p}})|^2}{|\psi_{\mathrm{c}}(\tilde{r} = 0, \eta_{\mathrm{p}} = 0)|^2} - 1 = \frac{2\pi\eta_{\mathrm{p}}}{1 - \exp(-2\pi\eta_{\mathrm{p}})} - 1 \overset{\eta_{\mathrm{p}} \ll 1}{\rightarrow} \pi\eta_{\mathrm{p}} \,,$$

which turns out to be small for $\eta_{\mathrm{p}} \ll 1$.

A further check for the strength of the perturbation is provided by inspecting the change of the electron density when an ion is added to a free electron target of density n. As a particular critical test we regard the induced density $\delta n(r) = n(r) - n$ at the ion location for the most severe case of an ion at rest ($v = 0$). In framework of the linear response treatment in Section 3.1, the induced density can be computed explicitly from the linear response relation (38) and by using the RPA dielectric function $\varepsilon_{\mathbf{R}}$ (47). A numerical survey yields

$$\frac{|\delta n(r = 0)|}{n} = \left| \frac{Z}{n(2\pi)^3} \int \mathrm{d}^3k \left[\frac{1}{\varepsilon_{\mathbf{R}}(k, \omega = 0)} - 1 \right] \right| = \langle \eta_{\mathrm{p}} \rangle h(\xi, \Theta) \approx \langle \eta_{\mathrm{p}} \rangle \,,$$

with $\langle \eta_{\mathrm{p}} \rangle$ as defined in Eq. (16), and a function $h(\xi, \Theta)$ which is of the order of unity for any degree of degeneracy Θ and any $\xi < 1$. The small relative change of the density resulting for $\langle \eta_{\mathrm{p}} \rangle \ll 1$ indicates a weak perturbation by the ion and linear coupling.

B.3. Definitions used for the Fourier-transformation

For the Fourier transformation of a function f in space and time we used throughout this review the definitions

$$f(\mathbf{r}, t) \rightarrow f(\mathbf{k}, \omega) = \int \mathrm{d}^3r \int_{-\infty}^{\infty} \mathrm{d}t\, f(\mathbf{r}, t) \exp(-\mathrm{i}(\mathbf{k} \cdot \mathbf{r} - \omega t)) \,,$$

$$f(\mathbf{k}, \omega) \rightarrow f(\mathbf{r}, t) = \int \frac{\mathrm{d}^3k}{(2\pi)^3} \int_{-\infty}^{\infty} \frac{\mathrm{d}\omega}{2\pi} f(\mathbf{k}, \omega) \exp(\mathrm{i}(\mathbf{k} \cdot \mathbf{r} - \omega t)) \,,$$

with the transform of a constant

$$f(\mathbf{r}, t) = 1 \rightarrow f(\mathbf{k}, \omega) = (2\pi)^3 \delta^3(\mathbf{k}) 2\pi \delta(\omega) \,.$$

B.4. Definitions of some important quantities

Wigner–Seitz radius

$$a = \left(\frac{4\pi n}{3}\right)^{-1/3}$$

Bohr radius

$$a_0 = \frac{\varepsilon_0 h^2}{\pi e^2 m} = 5.29 \times 10^{-11}\,\mathrm{m}$$

r_s parameter

$$r_s = \frac{a}{a_0} \approx \left[\frac{n_e}{1.6 \times 10^{24}\,\mathrm{cm}^{-3}}\right]^{-1/3}$$

Parameter of degeneracy

$$\Theta = \frac{k_\mathrm{B}T}{E_\mathrm{F}} = 2\frac{v_\mathrm{th}^2}{v_\mathrm{F}^2} = \frac{k_\mathrm{B}T}{13.6\mathrm{eV}}(\alpha r_s)^2, \quad \alpha = \left(\frac{4}{9\pi}\right)^{1/3} = 0.521$$

Parameter of ideality

$$\xi = \frac{2\alpha^2 r_s}{1 + \Theta}$$

Plasma parameter

$$\Gamma = \frac{e^2}{4\pi\varepsilon_0 k_\mathrm{B}T}\left(\frac{4\pi n}{3}\right)^{1/3} = \frac{e^2}{4\pi\varepsilon_0 k_\mathrm{B}Ta} = \frac{2\alpha^2 r_s}{\Theta}$$

Plasma frequency

$$\omega_\mathrm{p} = \left(\frac{e^2 n}{m\varepsilon_0}\right)^{1/2}$$

Plasma period

$$\tau_\mathrm{p} = \frac{2\pi}{\omega_\mathrm{p}}$$

Debye length

$$\lambda_D = \left(\frac{\varepsilon_0 k_\mathrm{B}T}{ne^2}\right)^{1/2} = \frac{v_\mathrm{th}}{\omega_\mathrm{p}} = \frac{a}{\sqrt{3\Gamma}}$$

Thermal velocity

$$v_\mathrm{th} = \left(\frac{k_\mathrm{B}T}{m}\right)^{1/2}$$

Fermi velocity

$$v_{\mathrm{F}} = \frac{\hbar(3\pi^2 n)^{1/3}}{m}$$

Fermi energy

$$E_{\mathrm{F}} = \frac{1}{2}mv_{\mathrm{F}}^2 = \frac{\hbar^2(3\pi^2 n)^{2/3}}{2m}$$

Averaged velocities (approximations)

$$\langle v_{\mathrm{r}} \rangle = (\langle v_{\mathrm{e}} \rangle^2 + v^2)^{1/2}, \quad \langle v_{\mathrm{r}} \rangle' = \frac{\langle v_{\mathrm{r}} \rangle}{\langle v_{\mathrm{e}} \rangle} = \left(1 + \frac{v^2}{\langle v_{\mathrm{e}} \rangle^2}\right)^{1/2},$$

$$\langle v_{\mathrm{e}} \rangle = (v_{\mathrm{F}}^2 + v_{\mathrm{th}}^2)^{1/2} = v_{\mathrm{F}}\left(1 + \frac{\Theta}{2}\right)^{1/2}$$

Classical collision diameter

$$b_0 = \frac{|Z|e^2}{4\pi\varepsilon_0 \mu v_{\mathrm{r}}^2} \overset{\mu v_{\mathrm{r}}^2 \to m\langle v_{\mathrm{r}} \rangle^2}{\rightarrow} \langle b_0 \rangle = \frac{|Z|e^2}{4\pi\varepsilon_0 m\langle v_{\mathrm{r}} \rangle^2} = \frac{|Z|\alpha^2 r_{\mathrm{s}}^2}{\langle v_{\mathrm{r}} \rangle'^2(1 + (\Theta/2))}a_0$$

The collision diameter b_0 is equal to the impact parameter for a classical collision in the (bare) Coulomb potential with $90°$ deflection angle at relative energy $\mu v_{\mathrm{r}}^2/2$.

Ion–electron Coulomb parameter

$$\eta_{\mathrm{p}} = \frac{|Z|e^2}{4\pi\varepsilon_0 \hbar v_{\mathrm{r}}} \overset{v_{\mathrm{r}} \to \langle v_{\mathrm{r}} \rangle}{\rightarrow} \langle \eta_{\mathrm{p}} \rangle = \frac{|Z|e^2}{4\pi\varepsilon_0 \hbar \langle v_{\mathrm{r}} \rangle^2} = \frac{|Z|\alpha r_{\mathrm{s}}}{\langle v_{\mathrm{r}} \rangle' \sqrt{1 + (\Theta/2)}}$$

Electron–electron Coulomb parameter

$$\eta_{\mathrm{e}} = \frac{e^2}{4\pi\varepsilon_0 \hbar v_{\mathrm{ee}}} \overset{v_{\mathrm{ee}} \to \langle v_{\mathrm{ee}} \rangle}{\rightarrow} \langle \eta_{\mathrm{e}} \rangle = \frac{e^2}{4\pi\varepsilon_0 \hbar \langle v_{\mathrm{ee}} \rangle} = \frac{\alpha r_{\mathrm{s}}}{\langle v_{\mathrm{ee}} \rangle' \sqrt{1 + (\Theta/2)}}$$

B.5. Notation

a	Wigner–Seitz radius $a = (4\pi n/3)^{-1/3}$
a_0	Bohr radius $0.529 \times 10^{-10}\,\mathrm{m}$
$b_0, \langle b_0 \rangle$	classical collision diameter
$C, \tilde{C}$	dimensionless friction coefficients
E	energy
$\mathscr{E}$	electric field
e	elementary charge, distinct from exponential function
$\mathrm{d}E/\mathrm{d}s$	stopping power
$\boldsymbol{F}$	force on the ion

f	phase space distribution function
f_0	phase-space distribution in ground state, usually Fermi or Maxwell
$f_B(x)$	Bose function
G	local field correction
g	spatial pair distribution function
$\hat{H}, \mathscr{H}$	Hamilton operator, function
I	high frequency limit of LFC (used in dynamic interpolation)
$\text{Im}[\dots]$	imaginary part
$\boldsymbol{k}, k$	wave number
k_B	Boltzmann constant
k_m	cutoff parameter
m	electron mass
M	projectile mass
N	particle number
N_D	number of electrons in a Debye sphere
$N_{\mu\nu}$	norm-matrix
n	bulk ground state electron density
$n(\boldsymbol{r})$	distribution of particle density
δn	small deviation from equilibrium density
$\boldsymbol{p}, p, \boldsymbol{P}, P$	momenta
$\boldsymbol{r}, \boldsymbol{R}$	coordinates in space
$R(Z, \Gamma)$	dimensionless friction coefficient for classical systems
r_s	a/a_0
S	structure factor (function), dynamic as well as static
S^{HNC}	static structure factor from HNC
T	electron temperature
t	time
U	one-body potential, mean field
V	two-body interaction, usually Coulomb
$\mathscr{V}_{Ewald}$	Ewald sum
$\boldsymbol{v}, v = |\boldsymbol{v}|$	ion velocity
$\hat{\boldsymbol{v}} = \boldsymbol{v}/v$	unit vector of ion velocity
v_r, v_{th}, v_F	relative, thermal, Fermi velocity
$v_e, \boldsymbol{u}, u$	electron velocities
Z	effective ion charge state or nuclear charge state
α	$(4/9\pi)^{1/3} = 0.521\dots$
Γ	(classical) plasma parameter
$\gamma, \ln\gamma$	$\ln\gamma = 0.577\dots$, Euler's constant
γ, γ_i	width parameter in the WPMD scheme (double usage of γ!)
$\delta(x), \delta^3(\boldsymbol{x})$	Dirac delta function
ε	dielectric function
ε_R	RPA dielectric function
ε_0	dielectric constant in vacuum

ε_α	single-electron energy
$\zeta, \tilde\zeta$	kinetic energy, free particle dispersion
$\eta_e, \langle\eta_e\rangle$	Coulomb parameter for electron–electron collisions
$\eta_p, \langle\eta_p\rangle$	Coulomb parameter for projectile-electron collisions
Θ	degree of degeneracy
$\theta(x)$	step function
κ	cutoff parameter
Λ	thermal wavelength
$\hat\lambda_r, \langle\hat\lambda_r\rangle$	de Broglie wavelength $\hbar/\mu v_r, \hbar/\mu\langle v_r\rangle$
λ, λ_D	screening length, Debye length
μ	reduced mass
v	electron–electron collision frequency
ξ	parameter of ideality
ϱ	charge density
$\hat\rho$	density operator
$\sigma, d\sigma/d\Omega$	differential cross section
σ_{tr}	transport cross section
τ	relaxation time
Υ	screening function
ϕ	electric potential
ϕ_p	bare ion potential
ϕ_{ei}	effective electron ion potential
φ	parameter of linearity of ion–target coupling
$\varphi_\alpha, \varphi_i, \varphi_q$	single-electron wavefunction
χ	denisty–density response function
χ_R	RPA density–density response function
χ_0	free particle density–density response function
$\lvert\Psi\rangle, \Psi$	wave function
ω	frequency
ω_p	plasma frequency
$[\ldots,\ldots]$	commutator
$\langle\ldots\rangle$	quantum and/or ensemble averaging

References

[1] I. Abril, R. Garcia-Molina, N.R. Arista, Nucl. Instr. and Meth. B 90 (1994) 72.

[2] S.P. Ahlen, Rev. Mod. Phys. 52 (1980) 121.

[3] A.I. Akhiezer, I.A. Akhiezer, R.V. Polovin, A.G. Sitenko, K.N. Stepanov, Plasma Electrodynamics, vol. 2, Pergamon Press, Oxford, 1975, Ch. 13.

[4] M.P. Allen, D.J. Tildesley, Computer Simulation of Liquids, Clarendon Press, Oxford, 1987.

[5] C.O. Almbladh, U. von Barth, Z.D. Popvic, M.J. Stott, Phys. Rev. B 14 (1976) 2250.

[6] N.R. Arista, W. Brandt, Phys. Rev. A 23 (1981) 1898.

[7] N.R. Arista, W. Brandt, Phys. Rev. A 29 (1984) 1471.

[8] N.W. Ashcroft, N.D. Mermin, Solid State Physics, Saunders, Philadelphia 1976.
[9] J.C. Ashley, R.H. Ritchie, W. Brandt, Phys. Rev. B 5 (1972) 2393.
[10] J.C. Ashley, Nucl. Instr. and Meth. 170 (1980) 197.
[11] J.C. Ashley, P.M. Echenique, Phys. Rev. B 31 (1985) 4655.
[12] J.C. Ashley, P.M. Echenique, Phys. Rev. B 35 (1987) 8701.
[13] S. Baird et al., Phys. Lett. B 361 (1995) 184.
[14] R. Balescu, Equilibrium and Non-Equilibrium Statistical Mechanics, Wiley, New York, 1975.
[15] U. von Barth, L. Hedin, J. Phys. C 5 (1972) 1629.
[16] J.E. Barnes, P. Hut, Nature 324 (1986) 446.
[17] W.H. Barkas, J.N. Dyer, H.H. Heckman, Phys. Rev. Lett. 11 (1963) 26.
[18] G. Bertsch, S. Das Gupta, Phys. Rep. 160 (1988) 190.
[19] H. Bethe, Ann. Physik 5 (1930) 325.
[20] F. Bloch, Ann. Physik 16 (1933) 285; 30 (1933) 72.
[21] N. Bohr, Phil. Mag. 25 (1913) 10; 30 (1915) 581.
[22] O. Boine-Frankenheim, J. D'Avanzo, Phys. Plasmas 3 (1996) 792.
[23] O. Boine-Frankenheim, Phys. Plasmas 3 (1996) 1585.
[24] E. Bonderup, K. Dan, Vidensk. Selsk. Mat. Fjs. Medd. 35 (1967) 17.
[25] L. Bönig, K. Schönhammer, Phys. Rev. B 39 (1989) 7413.
[26] Y. Boudouma, A.C. Chami, H. Beaumevieille, M. Boudjema, J. Phys. I France 2 (1992) 1803.
[27] M. Brack, Rev. Mod. Phys. 65 (1993) 677.
[28] G.I. Budker, Atomnaya Energiya 22 (1967) 346.
[29] F. Calvayrac, P.-G. Reinhard, E. Suraud, Ann. Phys. (N.Y.) 255 (1997) 125.
[30] R. Car, M. Parrinello, Phys. Rev. Lett. 55 (1985) 2471.
[31] D.M. Ceperley, B.J. Alder, Phys. Rev. Lett. 45 (1980) 566.
[32] D.M. Ceperley, Rev. Mod. Phys. 67 (1995) 279.
[33] M. Chabot et al., Il Nuovo Cimento 106 A (1993) 1789.
[34] C. Couillaud, R. Deicas, Ph. Nardin, M.A. Beuve, J.M. Guihaumé, M. Renaud, M. Cukier, C. Deutsch, G. Maynard, Phys. Rev. E 49 (1994) 1545.
[35] O.H. Crawford, J.J. Dorado, F. Flores, Nucl. Instr. and Meth. B 96 (1995) 610.
[36] O.H. Crawford, Phys. Rev. A 39 (1989) 4432.
[37] J. D'Avanzo, M. Lontano, P.F. Bortignon, Il Nuovo Cimento 106 A (1993) 1797.
[38] J. D'Avanzo, I. Hofmann, M. Lontano, Nucl. Instr. and Meth. A 415 (1998).
[39] C. Deutsch, Phys. Lett. A 60 (1977) 317.
[40] C. Deutsch, M.M. Gombert, H. Minoo, Phys. Lett. A 66 (1978) 381.
[41] C. Deutsch, Y. Furutani, M.M. Gombert, Phys. Rep. 69 (1981) 85.
[42] K.-G. Dietrich et al., Z. Phys. D 16 (1990) 229.
[43] K.-G. Dietrich et al., Phys. Rev. Lett. 69 (1992) 3623.
[44] A. Domps, A.S. Krepper, V. Savalli, P.-G. Reinhard, E. Suraud, Ann. Phys. (Leipzig) 6 (1997) 468.
[45] A. Domps, P.-G. Reinhard, E. Suraud, Ann. Phys. (N.Y.) 260 (1997) 171.
[46] R.M. Dreizler, E.K.U. Gross, Density Functional Theory, Springer, Berlin, 1990.
[47] J.W. Dufty, M. Berkovsky, Nucl. Instr. and Meth. B 96 (1995) 626.
[48] J.W. Dufty, M. Berkovsky, in: W.D. Kraeft, M. Schlanges (Eds.), Physics of Strongly Coupled Plasmas, World Scientific, Singapore, 1996, p. 165.
[49] P.M. Echenique, R.M. Nieminen, J.C. Ashley, R.H. Ritchie, Phys. Rev. A 33 (1986) 897.
[50] W. Ekardt, Phys. Rev. Lett. 52 (1984) 1925.
[51] H. Esbensen, P. Sigmund, Ann. Phys. 201 (1990) 152.
[52] H. Feldmeier, Nucl. Phys. A 515 (1990) 147.
[53] L. de Ferrariis, N.R. Arista, Phys. Rev. A 29 (1984) 2145.
[54] A.L. Fetter, J.D. Walecka, Quantum Theory of Many-Particle Systems, McGraw-Hill, New York, 1971.
[55] B.D. Fried, S.D. Conte, The Plasma Dispersion Function, Academic Press, New York, 1961.
[56] H. Furukawa, K. Nishihara, Phys. Rev. A 42 (1990) 3532.

[57] H. Gao et al., Phys. Rev. Lett. 75 (1995) 4381; Hyperfine Interactions 99 (1996) 301.
[58] X. Garbet, C. Deutsch, G. Maynard, J. Appl. Phys. 61 (1987) 907.
[59] D. Gardes, A. Servajean, B. Kubica, C. Fleurier, D. Hong, C. Deutsch, G. Maynard, Phys. Rev. A 46 (1992) 5101.
[60] E.P. George, T. Hamada, Phys. Lett. A 67 (1978) 369.
[61] D.O. Gericke, M. Schlanges, W.D. Kraeft, Phys. Lett. A 222 (1996) 241; Laser and Particle Beams 15 (1997) 523.
[62] H. Goldstein, Classical Mechanics, Addison-Wesley, Reading, MA, 1980.
[63] A. Gold, L. Calmels, Phys. Rev. B 48 (1993) 11622.
[64] C. Gouedard, C. Deutsch, J. Math. Phys. 19 (1978) 32.
[65] H.A. Gould, H.E. DeWitt, Phys. Rev. 155 (1967) 68.
[66] E.K.U. Gross, W. Kohn, Adv. Quant. Chem. 21 (1990) 255.
[67] E.K.U. Gross, C.A. Ullrich, U.J. Gossmann, in: E.K.U. Gross, R.M. Dreizler (Eds.), Density Functional Theory, NATO ASI Series, Plenum, New York, 1994.
[68] E.K.U. Gross, J.F. Dobson, M. Petersilka, in: R.F. Nalewjski (Ed.), Topics in Current Chemistry, Springer, Berlin, 1996.
[69] O. Gunnarson, B.I. Lundqvist, Phys. Rev. B 13 (1976) 4274.
[70] H.-S. Hahn, E.A. Mason, F.J. Smith, Phys. Fluids 14 (1971) 278.
[71] T. Hamada, Aust. J. Phys. 31 (1978) 291.
[72] J.P. Hansen, Phys. Rev. A 8 (1973) 3096.
[73] J.P. Hansen, I.R. McDonald, E.L. Pollock, Phys. Rev. A 11 (1975) 1025.
[74] J.P. Hansen, I.R. McDonald, Phys. Rev. Lett. 41 (1978) 1379.
[75] J.P. Hansen, I.R. McDonald, P. Vieillefosse, Phys. Rev. A 20 (1979) 2590.
[76] J.P. Hansen, I.R. McDonald, Phys. Rev. A 23 (1981) 2041.
[77] J.P. Hansen, I.R. McDonald, Theory of Simple Liquids, Academic Press, London, 1986.
[78] E.J. Heller, J. Chem. Phys. 62 (1975) 1544.
[79] K.W. Hill, E. Merzbacher, Phys. Rev. A 9 (1974) 156.
[80] R.W. Hockney, J.W. Eastwood, Computer Simulations Using Particles, McGraw-Hill, New York, 1981.
[81] I. Hofmann, in: J. Bosser (Ed.), Beam Cooling and Related Topics, CERN 94-03, Genf 1994, p. 330.
[82] D.H.H. Hoffmann et al., Z. Phys. A 330 (1988) 339.
[83] D.H.H. Hoffmann et al., Phys. Rev. A 42 (1990) 2313.
[84] P. Hohenberg, W. Kohn, Phys. Rev. 136 (1964) B864.
[85] D. Hohl, V. Natoli, D.M. Ceperley, R.M. Martin, Phys. Rev. Lett. 71 (1993) 541.
[86] N. Honda, J. Phys. Soc. Japan 19 (1964) 1201.
[87] S. Ichimaru, Basic Principles of Plasma Physics, Benjamin, Reading, MA, 1973.
[88] S. Ichimaru, S. Mitake, S. Tanaka, X.-Z. Yan, Phys. Rev. A 32 (1985) 1768.
[89] S. Ichimaru, S. Tanaka, Phys. Rev. A 32 (1985) 1790.
[90] S. Ichimaru, H. Iyetomi, S. Tanaka, Phys. Rep. 149 (1987) 91.
[91] S. Ichimaru, Statistical Plasma Physics, vol. 2, Addison-Wesley, Reading, MA, 1994, Chs. 3 and 4.
[92] H. Iyetomi, K. Utsumi, S. Ichimaru, Phys. Rev. B 24 (1981) 3226.
[93] A.D. Jackson, E. Krotschek, D.E. Meltzer, R.A. Smith, Nucl. Phys. A 386 (1982) 125.
[94] J. Jacoby, D.H.H. Hofmann, W. Laux, R.W. Müller, H. Wahl, K. Weyrich, E. Boggasch, B. Heimrich, C. Stöckl, H. Wetzler, S. Miyamoto, Phys. Rev. Lett. 74 (1995) 1550.
[95] J. Jacoby, C. Bickes, H.-P. Flierl, D.H.H. Hofmann, M. Dornik, K. Weyrich, C. Stöckl, H. Wetzler, Nucl. Instr. and Meth. B 115 (1996) 7.
[96] R.O. Jones, O. Gunnarsson, Rev. Mod. Phys. 61 (1989) 689.
[97] G. Kelbg, Ann. Physik 12 (1963) 219.
[98] D. Klakow, C. Toepffer, P.-G. Reinhard, Phys. Lett. A 192 (1994) 55.
[99] D. Klakow, C. Toepffer, P.-G. Reinhard, J. Chem. Phys. 101 (1994) 10766.
[100] D. Klakow, Molekulardynamik von Wellenpaketen in Coulomb-Systemen, Ph.D. thesis, Erlangen, 1994.
[101] M. Knaup, WPMD Simulationen von Ionen in Wasserstoffplasmen, Diploma thesis, Erlangen, 1996.
[102] W. Kohn, L.J. Sham, Phys. Rev. 40 (1965) A1133.
[103] W.D. Kraeft, B. Strege, Physica A 149 (1988) 313.

[104] P. Kramer, M. Saraceno, Geometry of the Time-Dependent Variational Principle in Quantum Mechanics, Lecture Notes in Physics, vol. 140, Springer, Berlin, 1967, and references therein.
[105] L.D. Landau, E.M. Lifshitz, Statistical Physics, Part 2, Pergamon Press, Oxford, 1980, Section 86.
[106] G. Lauritsch, P.G. Reinhard, Int. J. Mod. Phys. C 5 (1994) 65.
[107] R.L. Liboff, Phys. Fluids 2 (1959) 40.
[108] R.L. Liboff, Kinetic Theory, Prentice-Hall, Englewood Cliffs, NJ, 1990.
[109] J. Lindhard, K. Dan, Vidensk. Selsk. Mat. Fjs. Medd. 28 (1954) 8.
[110] Chi-Kang Li, R.D. Petrasso, Phys. Rev. Lett. 70 (1993) 3059, 3063.
[111] W.R. Magro, D.M. Ceperley, C. Pierloni, B. Bernu, Phys. Rev. Lett. 76 (1996) 1240.
[112] B. Majer, Diploma Thesis, Universität Erlangen, 1992.
[113] E.A. Mason, R.J. Munn, F.J. Smith, Phys. Fluids 10 (1967) 1827.
[114] R.M. May, Aust. J. Phys. 22 (1969) 687.
[115] G. Maynard, C. Deutsch, J. Physique 46 (1985) 1113.
[116] G. Maynard et al., Il Nuovo Cimento A 106 (1993) 1825.
[117] G. Maynard, K. Katsonis, S. Mabong, Nucl. Instr. and Meth. B 107 (1996) 51.
[118] G. Maynard, K. Katsonis, G. Zwicknagel, S. Mabong, M. Chabot, D. Gardes, Yu.K. Kurilenkov, Nucl. Instr. and Meth. A 415 (1998) 687.
[119] G. Maynard, G. Zwicknagel, M. Chabot, D. Gardes, to be published.
[120] G. Maynard, G. Zwicknagel, to be published.
[121] N.D. Mermin, Phys. Rev. B 1 (1970) 2362.
[122] A. Messiah, Quantum Mechanics, vol. I, Wiley, New York, 1970, Ch. XI, Appendix B.
[123] S. Mitake, S. Tanaka, X.-Z. Yan, S. Ichimaru, Phys. Rev. A 32 (1985) 1775.
[124] K. Morawetz, G. Röpke, Phys. Rev. E 54 (1996) 4134.
[125] S. Moroni, D. Ceperley, G. Senatore, Phys. Rev. Lett. 75 (1995) 689.
[126] I. Nagy, A. Arnau, P.M. Echenique, E. Zaremba, Phys. Rev. B 40 (1989) 11983.
[127] E. Nardi, Z. Zinamon, Phys. Rev. Lett. 49 (1982) 1251.
[128] B.R.A. Nijboer, F.W. De Wette, Physica XXIII (1957) 309.
[129] W.H. Press, B.P. Flannery, S.A. Teukolsky, W.T. Vetterling, Numerical Recipies, Cambridge University Press, Cambridge, 1989.
[130] A. Ono, H. Horiuchi, T. Maruyama, A. Ohnishi, Prog. Theor. Phys. 87 (1992) 1185.
[131] C.A. Ordonez, M.I. Molina, Phys. Rev. Lett. 72 (1994) 2407.
[132] M. Schlanges, D.O. Gericke, W.D. Kraeft, Th. Bornath, Nucl. Instr. Meth. A 415 (1998) 517.
[133] F.J. Perez-Perez, I. Abril, R. Garcia-Molina, N.R. Arista, Phys. Rev. A 54 (1996) 4145.
[134] F.J. Perez-Perez, I. Abril, N.R. Arista, R. Garcia-Molina, Nucl. Instr. and Meth. B 115 (1996) 18.
[135] T. Peter, J. Meyer-ter-Vehn, Phys. Rev. A 43 (1991) 1998.
[136] T. Peter, J. Meyer-ter-Vehn, Phys. Rev. A 43 (1991) 2015.
[137] S. Pfalzner P. Gibbon, in: Physics of Nonideal Plasmas, W. Ebeling (Ed.), Teubner, Stuttgart, 1992, p. 43.
[138] M. Petersilka, U.J. Gossmann, E.K.U. Gross, Phys. Rev. Lett. 76 (1996) 1212.
[139] D. Pines, Elementary Excitations in Solids, Benjamin, New York, 1964.
[140] D. Pines, P. Nozière, The Theory of Quantum Liquids Vol. I, Benjamin, New York, 1966.
[141] J.M. Pitarke, R.H. Ritchie, P.M. Echenique, Phys. Rev. B 52 (1995) 13883.
[142] H. Poth, Phys. Rep. 196 (1990) 135.
[143] J.J. Barnard, T.J. Fessenden, E.P. Lee (Eds.), Proc. Int. Symp. on Heavy Ion Inertial Fusion, Princeton, September 1995, Fusion Engineering and Design 32–33 (1996).
[144] J. Bosser (Ed.), Proc. Workshop on Beam cooling and Related topics, Montreux, October 1993, CERN 94-03, 1994.
[145] D.M. Maletić, A.G. Ruggiero (Eds.), Proc. 31st Workshop of the INFN Eloisatron project, Erice, November 1995, Crystalline Beams and Related Issues, World Scientific, Singapore, 1996.
[146] R. Redmer, Phys. Rep. 282 (1997) 35.
[147] P.-G. Reinhard, N. Rowley, D.M. Brink, Z. Phys. 266 (1974) 149.
[148] P.-G. Reinhard, E. Suraud, Ann. Phys. (NY) 239 (1995) 193, 216.

[149] P.-G. Reinhard, E. Suraud, Z. Phys. A 355 (1996) 339.
[150] G. Rein, Math. Meth. Appl. Sci. 15 (1992) 365.
[151] E. Runge, E.K.U. Gross, Phys. Rev. Lett. 52 (1984) 997.
[152] J.K. Salmon, M.S. Warren, J. Comput. Phys. 111 (1994) 136.
[153] Yu.S. Sayasov, Z. Phys. A 313 (1983) 9.
[154] Yu.S. Sayasov, Laser and Particle Beams 10 (1992) 505.
[155] L.I. Schiff, Quantum Mechanics, Wiley, McGraw-Hill, New York, 1968, Section 21.
[156] K. Schönhammer, Phys. Rev. B 37 (1988) 7735.
[157] U. Schramm et al., Hyperfine Interactions 99 (1996) 309.
[158] H.K. Schweng, H.M. Boehm, A. Schinner, W. Macke, Phys. Rev. B 44 (1991) 13291.
[159] H.K. Schweng, H.M. Boehm, Phys. Rev. B 48 (1993) 2037.
[160] C. Seele, Diploma Thesis, Universität Erlangen, 1995.
[161] C. Seele, G. Zwicknagel, C. Toepffer, Phys. Rev. E 57 (1998) 3368.
[162] G. Senatore, S. Moroni, D. Ceperley, J. Non-Cryst. Solids 205–207 (1996) 851.
[163] A. Servajean, J. Appl. Phys. 71 (1992) 2587.
[164] P. Sigmund, Phys. Rev. A 26 (1982) 2497.
[165] K.S. Singwi, M.P. Tosi, R.H. Land, A. Sjölander, Phys. Rev. 176 (1968) 589.
[166] A.H. Sørensen, E. Bonderup, Nucl. Instr. and Meth. 215 (1983) 27.
[167] Q. Spreiter, Diploma thesis, Universität Erlangen, 1995.
[168] Q. Spreiter, M. Seurer, C. Toepffer, Nucl. Instr. and Meth. A 364 (1995) 239.
[169] Q. Spreiter, C. Toepffer, Hyperfine Interactions (1998), in press.
[170] M. Steck et al., in: D.M. Maletić, A.G. Ruggiero (Eds.), Crystalline Beams and Related Issues, World Scientific, Singapore, 1996, p. 459.
[171] M. Stetter, GSI Darmstadt, Private communications, 1997.
[172] B. Strege, W.D. Kraeft, Laser and Particle Beams 10 (1992) 227.
[173] S. Tanaka, S. Mitake, X.-Z. Yan, S. Ichimaru, Phys. Rev. A 32 (1985) 1779.
[174] S. Tanaka, X.-Z. Yan, S. Ichimaru, Phys. Rev. A 41 (1990) 5616.
[175] K. Utsumi, S. Ichimaru, Phys. Rev. B 22 (1980) 1522, 5203; 23 (1981) 3291.
[176] K. Utsumi, S. Ichimaru, Phys. Rev. A 26 (1982) 603.
[177] O. Uwira et al., Hyperfine Interactions 99 (1996) 295.
[178] L. Verlet, Phys. Rev. 159 (1967) 98.
[179] G. Viesti, P. Boccaccio, Il Nuovo Cimento 1D (1982) 95.
[180] S.H. Vosko, L. Wilk, M. Nusair, Can. J. Phys. 58 (1980) 1200.
[181] You-Nian Wang, Teng-Cai Ma, Phys. Lett. A 200 (1995) 319.
[182] Wang Neng-ping, Ho Yu-kun, Phys. Rev A 52 (1995) 3953.
[183] S. Weisgerber, P.-G. Reinhard, Phys. Lett. A 158 (1991) 407.
[184] S. Weisgerber, P.-G. Reinhard, Z. Phys. D 23 (1992) 275.
[185] Th. Winkler et al., Hyperfine Interactions 99 (1996) 277.
[186] Th. Winkler, K. Beckert, F. Bosch, H. Eickhoff, B. Franzke, F. Nolden, H. Reich, B. Schlitt, M. Steck, Nucl. Instr. and Meth. A 391 (1997) 12.
[187] Th. Winkler, Private communications, 1998.
[188] A. Wolf et al., in: J. Bosser (Ed.), Beam Cooling and Related Topics, CERN 94-03, Genf, 1994, p. 416.
[189] X.-Z. Yan, S. Tanaka, S. Mitake, S. Ichimaru, Phys. Rev. A 32 (1985) 1785.
[190] E. Zaremba, A. Arnau, P.M. Echenique, Nucl. Instr. and Meth. B 96 (1995) 619.
[191] G. Zwicknagel, D. Klakow, P.-G. Reinhard, C. Toepffer, Contrib. Plasma Phys. 33 (1993) 395.
[192] G. Zwicknagel, C. Toepffer, P.-G. Reinhard, Il Nuovo Cimento A 106 (1993) 1857.
[193] G. Zwicknagel, C. Toepffer, P.-G. Reinhard, in: J. Bosser (Ed.), Beam Cooling and Related Topics, CERN 94-03, Genf 1994, p. 245.
[194] G. Zwicknagel, Energieverlust schwerer Ionen in stark gekoppelten Plasmen, Ph.D. thesis, Universität Erlangen, 1994.
[195] G. Zwicknagel, C. Toepffer, P.-G. Reinhard, Laser and Particle Beams 13 (1995) 311.

[196] G. Zwicknagel, C. Toepffer, P.-G. Reinhard, in: W.D. Kraeft, M. Schlanges (Eds.), Physics of Strongly Coupled Plasmas, World Scientific, Singapore, 1996, p. 45.
[197] G. Zwicknagel, C. Toepffer, P.-G. Reinhard, Hyperfine Interactions 99 (1996) 285.
[198] G. Zwicknagel, C. Deutsch, Laser and Particle Beams 14 (1996) 749.
[199] G. Zwicknagel, C. Toepffer, P.-G. Reinhard, Fusion Eng. Des. 32–33 (1996) 523.
[200] G. Zwicknagel, Q. Spreiter, M. Miller, C. Toepffer, P.-G. Reinhard, in: D.M. Maletić, A.G. Ruggiero (Eds.), Crystalline Beams and Related Issues, World Scientific, Singapore, 1996, p. 185.
[201] G. Zwicknagel, Q. Spreiter, C. Toepffer, Hyperfine Interactions 108 (1997) 131.
[202] G. Zwicknagel, Nucl. Instr. and Meth. A 415 (1998) 680.